



저작자표시-비영리-변경금지 2.0 대한민국

이용자는 아래의 조건을 따르는 경우에 한하여 자유롭게

- 이 저작물을 복제, 배포, 전송, 전시, 공연 및 방송할 수 있습니다.

다음과 같은 조건을 따라야 합니다:



저작자표시. 귀하는 원저작자를 표시하여야 합니다.



비영리. 귀하는 이 저작물을 영리 목적으로 이용할 수 없습니다.



변경금지. 귀하는 이 저작물을 개작, 변형 또는 가공할 수 없습니다.

- 귀하는, 이 저작물의 재이용이나 배포의 경우, 이 저작물에 적용된 이용허락조건을 명확하게 나타내어야 합니다.
- 저작권자로부터 별도의 허가를 받으면 이러한 조건들은 적용되지 않습니다.

저작권법에 따른 이용자의 권리는 위의 내용에 의하여 영향을 받지 않습니다.

이것은 [이용허락규약\(Legal Code\)](#)을 이해하기 쉽게 요약한 것입니다.

[Disclaimer](#)

Doctor of Philosophy

**Deposition of 2D Materials by Vacuum Kinetic Spray
Method and Its Application in Supercapacitors**

The Graduate School of
the University of Ulsan

School of Mechanical
Engineering

Mohaned Mohammed Mahmoud Mohammed

Deposition of 2D Materials by Vacuum Kinetic Spray
Method and Its Application in Supercapacitors

Supervisor: Professor Doo-Man Chun

A Dissertation

Submitted to the Graduate School of the University of Ulsan in Partial
Fulfillment of the Requirements for the Degree of

Doctor of Philosophy

By

Mohaned Mohammed Mahmoud Mohammed

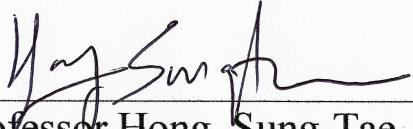
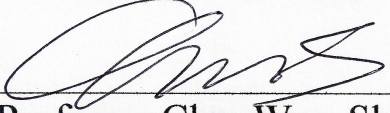
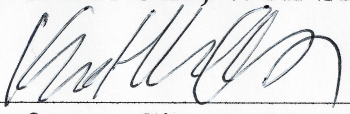
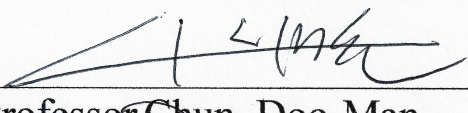
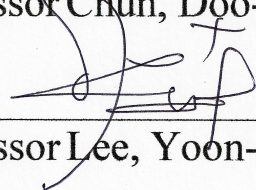
School of Mechanical Engineering

University of Ulsan, South Korea

February 2020

Deposition of 2D Materials by Vacuum Kinetic Spray
Method and Its Application in Supercapacitors

This certifies that the thesis of Mohaned Mohammed Mahmoud Mohammed
is approved.






Committee Chairman:	 Professor Hong, Sung-Tae
Committee Member:	 Professor Chu, Won-Shik
Committee Member:	 Professor Chung, Koo-Hyun
Committee Member:	 Professor Chun, Doo-Man
Committee Member:	 Professor Lee, Yoon-Ho

School of Mechanical Engineering

University of Ulsan, South Korea

February 2020

Mohaned Mohammed Mahmoud Mohammed의 공학석사 학위
논문을 인준함

심사위원장	홍성태	
심사위원	추원식	
심사위원	정구현	
심사위원	천두만	
심사위원	이윤호	

울산대학교 대학원

2020년 02월

Acknowledgments

I would like to express my deep and sincere gratitude to many people who made this PhD thesis possible. Special thanks are due to my supervisor Professor Doo-Man Chun for his insight resolving many of the problems encountered throughout research and thesis writing, for his inspiring and encouraging way to guide me to a deeper understanding of research, and his invaluable comments during my graduate study.

I am highly indebted to my committee members Professors Sung-Tae Hong, Koo-Hyun Chung, Yoon-Ho Lee, and Won-Shik Chu. Many thanks are due to Hybrid Manufacturing Technology (HMT) lab members for helping and supporting me all the time.

Finally, I would like to thank my wife, she is always there support me and stands by me through good and bad times. She and my son have lost a lot due to my research abroad.

Abstract

The developments in mobile/portable electronics and alternative energy vehicles prompted engineers and researchers to develop electrochemical energy storage devices called supercapacitors, as the third-generation type capacitors. Most of the research and development on supercapacitors focus on electrode materials, electrolytes, and hybridization. Some attempts have been directed towards increasing the energy density by employing electroactive materials, such as metal oxides and conducting polymers. However, the high cost and toxicity of applicable metal oxides and poor long-term stability of the conducting polymers paved the way for alternative electrode materials. The electroactive materials with carbon particles in composites have been used substantially to improve the stability of supercapacitors. Furthermore, the use of carbon particles and metal oxides could significantly increase the energy density of supercapacitor electrodes compared to metal oxides. Recent developments in carbon materials, such as carbon nanotubes (CNTs), activated carbon, reduced graphene oxide, and graphene, have found applications in supercapacitors because of their enhanced double-layer capacitance due to the large surface area, electrochemical stability, and excellent mechanical and thermal properties.

Several approaches have been used to develop binder-free supercapacitor hybrid electrode materials, such as electrochemical deposition, chemical bath deposition, chemical vapor deposition, and the sol-gel method. These approaches have been shown some drawbacks, such as complicated processes, long processes time, expensive equipment, high vacuum, volatile precursors and toxic chemicals. On the contrary, the nanoparticle deposition system (NPDS) offers low vacuum, room temperature, eco-friendly, and binder-free deposition method.

The main objective of this thesis is to study the deposition of some electroactive materials using the NPDS technique. Promising electroactive materials, such as few-layer graphene nano-flakes, molybdenum disulfide, nickel

hydroxide, and graphene-based composites have been selected to be deposited by the NPDS. The deposition was carried out with different deposition parameters, and different contents of the electroactive materials. By studying the structural and electrochemical performance of these materials, we have established a complete set of deep understandings on the concepts, structures at varying lengthy scales and electrochemical performance.

The research carried out in this thesis are briefly summarized as follows:

- (1) The effect of the deposition parameters on the formation of few-layer graphene nano-flakes and their related electrochemical performance are examined by changing the scan speed of the deposition. The faster scan speed of deposition shows higher degree of fragmentation and better electrochemical performance. The electrochemical performance of the few-layer graphene nano-flakes symmetric supercapacitor was further improved by increasing the different electrolytes concentration.
- (2) The influence of MoS₂ content on the electrochemical performance of MoS₂-graphite hybrid electrode is studied. The MoS₂-graphite hybrid electrode deposited with 5, 10, 15, 20, 25 and 30% wt. of MoS₂ by the NPDS on stainless-steel substrates. The capacitance of the MoS₂-graphite hybrid electrodes based symmetric supercapacitor demonstrates maximum areal capacitance at 15% of MoS₂ content used in the deposition (5.1 mF cm⁻² @ 2 mV s⁻¹).
- (3) Ni(OH)₂ deposited by the NPDS on nickel sheets and nickel foam. The structural and electrochemical performance of the Ni(OH)₂ deposited with different parameters on nickel sheets are compared. The deposited Ni(OH)₂ on nickel sheets with 5 mm SoD and 0.3 MPa carrier gas pressure demonstrates better electrochemical performance. The Ni(OH)₂ deposition on nickel foam with 5 mm SoD and 0.3 MPa showed superior specific capacitance (2092 F g⁻¹ @ 1 A g⁻¹) and good cyclic stability.

(4) The effect of Ni(OH)_2 content in Ni(OH)_2 -graphene hybrid electrodes on the electrochemical performance is examined. Ni(OH)_2 and graphite powders is mixed with 20, 40, 60, and 80% wt. of Ni(OH)_2 and deposited on nickel foam substrate. The structural and electrochemical performance of the Ni(OH)_2 -graphene hybrids is investigated. The Ni(OH)_2 -graphene hybrids demonstrates a maximum specific capacitance at 10% the content of the Ni(OH)_2 in the hybrid electrode. An asymmetric supercapacitor is fabricated based on 10% Ni(OH)_2 -graphene hybrid electrodes as a positive electrode and rGO as a negative electrode. The Ni(OH)_2 -Gr//rGO ASC displays an energy density of 64 W h kg^{-1} and a high power density of 8230 W kg^{-1} .

Contents

Acknowledgments	i
Abstract	ii
Contents	v
List of Figures	viii
List of Tables	xiii
List of Abbreviations	xv
Chapter 1 Introduction	1
1.1 Background	2
1.2 Types of Supercapacitors	4
1.2.1 Electric double-layer capacitance	5
1.2.2 Pseudocapacitance	7
1.2.3. Hybrid.....	7
1.3 Electrode Materials	9
1.3.1 Activated carbon.....	9
1.3.2 Carbon nanotubes (CNTs).....	9
1.3.3 Graphene.....	10
1.3.4 Metal Oxides.....	11
1.3.5 Conducting Polymers	12
1.4 Electrolytes.....	13
1.5 Separators	14
1.6 Fabrication Methods of Electrode Materials	14
1.6.1 Electrochemical deposition.....	15
1.6.2 Chemical bath deposition (CBD)	16
1.6.3 Chemical vapor deposition (CVD).....	17
1.6.4 Sol-gel.....	19
1.7 Nano-Particle Deposition System (NPDS)	20
1.8 Research Motivations and Objectives	26
1.9 Thesis Organization.....	27
Chapter 2 Experimental Section	29
2.1 Materials.....	30
2.2 Materials Preparation	30
2.3 Characterization Techniques	31
2.3.1 Field Emission-Scanning Electron Microscopy (FE-SEM)	31
2.3.2 High-Resolution Transmission Electron Microscopy (HR-TEM)	31

2.3.3 X-Ray Diffraction (XRD).....	31
2.3.4 Raman Spectroscopy	32
2.3.5 X-ray photoelectron spectroscopy (XPS).....	32
2.4 Electrochemical Performance	33
Chapter 3 Symmetric Supercapacitor Fabricated Based on Few-Layer Graphene Nano-Flakes	36
3.1 Background	37
3.2 Materials and Methods	41
3.2.1 Graphene electrode preparation.....	41
3.3 Results and Discussion.....	42
3.3.1 Morphology properties	42
3.3.2 X-ray diffraction analysis	47
3.3.3 Raman Spectroscopy	49
3.3.4 Electrochemical properties	52
3.4 Summary	63
Chapter 4 Symmetric Supercapacitor Based on MoS₂-Graphite Composite.....	64
4.1 Background	65
4.2 Experiment	67
4.2.1 MoS ₂ -graphite powder mixing	67
4.2.2 MoS ₂ -graphite composite deposition.....	67
4.3 Results and Discussion.....	68
4.3.1 Surface Morphology	68
4.3.2 XRD.....	71
4.3.3 Raman Spectroscopy	73
4.3.4 Electrochemical performance	75
4.4 Summary	80
Chapter 5 Deposition of Ni(OH)₂ on nickel substrate using vacuum kinetic spray and its application to high-performance supercapacitor.....	82
5.1 Background	83
5.2 Experimental	84
5.2.1 Ni(OH) ₂ Deposition on Ni sheets	84
5.3 Results and Discussion.....	85
5.3.1 Surface Morphology	85
5.3.2 X-ray Diffraction	88
5.3.3 Raman Spectroscopy	90

5.3.4 Electrochemical performance	91
5.3.5 Deposition of Ni(OH) ₂ on nickel foam.....	92
5.4 Summary	97
Chapter 6 High energy density asymmetric supercapacitors based on Ni(OH)₂-graphene hybrid electrode	99
6.1 Background	100
6.2 Experiment	102
6.2.1 Deposition of Ni(OH) ₂ -Gr composite powder.....	102
6.2.2 Preparation of reduced graphene oxide (rGO)	103
6.3 Results and Discussion.....	103
6.3.1 Positive electrode material.....	103
6.3.2 Negative electrode material	115
6.3.3 Asymmetric supercapacitor	117
6.4 Summary	120
Chapter 7 Conclusion	121
7.1 Conclusion.....	122
7.2 Recommendations	126
References	128
Appendices.....	162
Appendix A: Credits & Copyright Permissions.....	162
List of Publications	164

List of Figures

Figure 1 Ragone plot for various energy storage devices[8].	3
Figure 2 Taxonomy of supercapacitors.	4
Figure 3 Schematic representation of electrical double layer structures according to (a) the Helmholtz model, (b) the Gouy-Chapman model, and (c) the Gouy-Chapman-Stern model[11].	6
Figure 4 Scheme of electrochemical deposition technique.	16
Figure 5 Schematic diagram of CVD.	19
Figure 6 (a) schematic diagram of the NPDS, (b) top view, and (c) perspective view of the deposition processes.	24
Figure 7 (a) dipping deposited electrode into the gel electrolyte; (b) assembly of the fabricated supercapacitor.	34
Figure 8 Mass per unit area verses the thickness of the deposited films with scan speeds 0.4, 0.8 and 1.2 mm/min.	43
Figure 9 FESEM of (a) graphite powder, deposited film at scan speeds (b, c) 0.4 mm/min, (d, e) 0.8 mm/min and (f, g) 1.2 mm/min, respectively.	45
Figure 10 (a) HR-TEM image of the deposited film with scan speed 1.2 mm/min, (b) FFT of image (a), (c) Histogram plot of the area surrounded by the yellow rectangular in (a), and (d) magnified HR-TEM of the area surrounded by the yellow rectangular in (a) (In the top right, inset FFT of image (d))	47
Figure 11 XRD of the graphite powder, SUS304 substrate, and deposited films at different scan speeds.	48

Figure 12 Raman spectroscopy of (a) the graphite powder and deposited films at different scan speeds on larger size particles with less fragmentation, (b) graphite powder and deposited films at different scan speeds on the more fragmented particles.51

Figure 13 (a-c) CV curves of 0.03 mol of H₃PO₄ gel electrolyte with different scan speeds, (d) calculated specific areal capacitance from CV curves.54

Figure 14 CV curves of (a) 0.06, (b) 0.09 mol of H₃PO₄ gel electrolyte with a 1.2 mm/min scan speed electrode, and (c) the calculated areal capacitance for 0.06 and 0.09 mol of H₃PO₄ gel electrolyte with a 1.2 mm/min scan speed electrode.56

Figure 15 (a-c) Galvanostatic charge/ discharge curves of 0.03 mol of H₃PO₄ gel electrolyte with different scan speeds, (d) Calculated specific areal capacitance from charge/ discharge curves.57

Figure 16 galvanostatic charge/ discharge curves of (a) 0.06, (b) 0.09 mol of H₃PO₄ gel electrolyte with a 1.2 mm/min scan speed electrode, and (c) the calculated areal capacitance for 0.06 and 0.09 mol of H₃PO₄ gel electrolyte with a 1.2 mm/min scan speed electrode.58

Figure 17 Nyquist plots of (a) 0.03 mol of H₃PO₄ gel electrolyte with different scan speeds, (b) 0.03, 0.06 and 0.09 mol of H₃PO₄ gel electrolyte with a 1.2 mm/min scan speed electrode.61

Figure 18 Charge /discharge stability over 5000 cycles for a 1.2 mm/min scan speed and 0.09 mol of H₃PO₄- PVA at a current of 0.06 mA.....62

Figure 19 FE-SEM images of (a) bulk MoS₂, (b) bulk graphite, (c) mechanically mixed 15% MoS₂-graphite powder, and (d–f) 15% MoS₂-graphite deposited composite on stainless steel.69

Figure 20 (a) the cross-sectional SEM image, (b) enlarged cross-sectional SEM image of 15% MoS₂-graphite deposited composite on stainless steel, (c) FE-SEM and EDS of mechanically mixed 15% MoS₂-graphite composite powder, and (d) SEM and EDS of 15% MoS₂-graphite deposited composite on stainless steel.. 70

Figure 21 XRD results of bulk MoS₂, bulk graphite, mechanically mixed 15% MoS₂-graphite powder, and 15% MoS₂-graphite deposited composite on stainless steel. 73

Figure 22 Raman spectra of bulk MoS₂, bulk graphite, mechanically mixed 15% MoS₂-graphite powder, and deposited 15% MoS₂-graphite composite on stainless steel. 74

Figure 23 (a) CV curves at a scan rate of 20 mV/s, (b) galvanostatic charge/discharge at a current of 0.04 mA, and (c) specific areal capacitance calculated from CV curves and galvanostatic charge/discharge of graphite and MoS₂-graphite composite supercapacitors with different composition ratios ranging from 5 to 30%. 77

Figure 24 (a) CV curves at different scan rates of 2–100 mV/s, (b) galvanostatic charge/discharge at a current range of 0.1–0.01 mA, (c) specific areal capacitance calculated from CV curves and galvanostatic charge/discharge, and (d) cycling performance of 15% MoS₂-graphite composite supercapacitor, (e) the charge/discharge of first 5 cycles and last 4 cycles, (f) Nyquist plots of 15% MoS₂-graphite composite supercapacitor. 79

Figure 25 FE-SEM images of (a) Ni(OH)₂ powder and, (b) Ni sheet substrate. 86

Figure 26 FE-SEM images of the deposited Ni(OH)₂ thin films on Ni sheets with different deposition conditions, (a, b) 2.5 mm – 0.1 MPa, (c, d) 2.5 mm – 0.3 MPa, (e, f) 5 mm – 0.1 MPa and, (g, h) 5 mm – 0.3 MPa (the right images are low-magnified, and the left images are high-magnified)..... 87

Figure 27 (a) XRD spectra, (b) enlarged view of (001) XRD peak, (c) Raman spectra of Ni(OH) ₂ powder, nickel sheet, and deposited Ni(OH) ₂ films with powder pressure of 0.1 MPa and 0.3 MPa in both SoDs 2.5 and 5 mm, and (d) CV curves of deposited films on nickel sheet with powder pressure of 0.1 MPa and 0.3 MPa in both SoDs 2.5 and 5 mm	89
Figure 28 FE-SEM images of (a-c) nickel foam, (d-f) deposited Ni(OH) ₂ on nickel foam substrate.	93
Figure 29 (a) XRD of nickel foam and deposited Ni(OH) ₂ on nickel foam substrate, (b) Raman spectrum of the deposited Ni(OH) ₂ on nickel foam substrate.	94
Figure 30 (a) XPS survey, (b) high-resolution XPS scan of Ni 2p, and (c) high-resolution XPS scan of O 1s for the deposited Ni(OH) ₂ on nickel foam substrate.	95
Figure 31 (a) CV curves at different scan rates, (b) galvanostatic charge-discharge curves at different current density, (c) calculated specific capacitance from CV and GCD curves, and (d) cyclic stability of the deposited Ni(OH) ₂ films on nickel foam substrate.	97
Figure 32 FESEM images of (a) raw graphite powder, (b) raw Ni(OH) ₂ powder, (c) mixed Ni(OH) ₂ -graphite powder, (d) nickel foam, (e) 10% Ni(OH) ₂ -Gr deposited composite, and (f) EDS mapping of the 10% Ni(OH) ₂ -Gr deposited composite.	105
Figure 33 (a) XRD spectra, (b) Raman spectra of the graphite and Ni(OH) ₂ powders and the 10% Ni(OH) ₂ -Gr deposited composite, (c) XPS survey scan, (d) high-resolution C 1s scan, (e) high-resolution Ni 2p scan, and (f) high-resolution O 1s scan.	109

Figure 34 (a) comparison of specific capacitances of Ni(OH)₂-Gr hybrid electrodes with different Ni(OH)₂ content (0~100% by wt.) at various current densities of 1~20 A g⁻¹, (b) CV curves, (c) GCD curves, (d) the variation of specific capacitances of 10% Ni(OH)₂-Gr hybrid electrode as a function of scan rate and current density, and (e) cyclic stability of Gr, Ni(OH)₂, and the 10% Ni(OH)₂-Gr hybrid electrode at a scan rate of 100 mV s⁻¹.113

Figure 35 (a) XRD spectra, (b) Raman spectra of graphite, GO, and rGO, (c) CV curves at different scan rates, (d) GCD curves at different current densities, (e) specific capacitance versus current density, and (f) cycling stability for 3000 cycles at a current density of 10 A g⁻¹ for the rGO electrode.116

Figure 36 (a) Schematic diagram of the Ni(OH)₂-Gr//rGO ASC,(b) CV curves of the Ni(OH)₂-Gr//rGO ASC at various scan rates, (c) GCD curves of the Ni(OH)₂-Gr//rGO ASC at various current densities, (d) specific capacitance of the Ni(OH)₂-Gr//rGO ASC at different current densities, (e) Ragone plot of the Ni(OH)₂-Gr//rGO ASC, and (f) cyclic stability of the Ni(OH)₂-Gr//rGO ASC at 6 mA cm⁻² current density.....119

List of Tables

Table 1 Deposited materials using NPDS.....	21
Table 2 Different synthesis methods of electrode materials in terms of advantages and disadvantages	25
Table 3 Process parameters for graphite deposition on the stainless-steel substrate.....	42
Table 4 Thickness and mass values of the deposited films with different scan speeds.	43
Table 5 D, G, and 2D peaks and I_D/I_G for the graphite powder and deposited films.	52
Table 6 Process parameters for MoS ₂ -graphite composite deposition on a stainless-steel substrate	68
Table 7 Composition ratio of 15% MoS ₂ -graphite composite before and after the deposition	71
Table 8 Process parameters for Ni(OH) ₂ deposition on a nickel sheet.	85
Table 9 Crystallite size of the powder and deposited films with different deposition conditions for (001) XRD peak and FWHM of 3581 cm ⁻¹ Raman peak.	90
Table 10 Characteristic potential data of the deposited films with different deposition conditions obtained from CV curves at 10 mV s ⁻¹	92
Table 11 Deposition parameters for the Ni(OH) ₂ -graphene hybrid electrodes deposited on nickel foam with different Ni(OH) ₂ content (0~100% by wt.). (The piston speed was reduced according to Ni(OH) ₂ content to achieve similar loading masses).	103

Table 12 The calculated specific capacitance of the Ni(OH)₂-graphene hybrid electrodes deposited on nickel foam with different Ni(OH)₂ content (0~100% by wt.) from the GCD curves at different current densities from 1 A g⁻¹ to 20 A g⁻¹.
.....112

Table 13 Specific capacitance of the Ni(OH)₂-Gr hybrid electrode obtained in this study, compared with some of the Ni(OH)₂ and carbon-based hybrid electrodes reported in previous literature.....114

Table 14 Summary of the electrochemical performance of the studied 3-electrode configuration and the fabricated symmetric and asymmetric hybrid supercapacitors.....125

List of Abbreviations

EDL	Electric double-layer
EDLC	Electric double-layer capacitor
IHP	Inner Helmholtz plane
OHP	Outer Helmholtz plane
C_t	Total capacitance
C_H	Compact/Helmholtz double-layer capacitance
C_{diff}	Diffusion layer capacitance
AC	Activated carbon
CNTs	Carbon nanotubes
ESR	Equivalent series resistance
CV	Cyclic voltammetry
WE	Working electrode
CE	Counter electrode
RE	Reference electrode
CBD	Chemical bath deposition
CVD	Chemical vapor deposition
NPDS	Nano-particle deposition system
DSSC	Dye-sensitized solar cell
ECD	Electrochromic Device
SoD	Stand-off distances
CFD	Computational fluid dynamics
FE-SEM	Field Emission-Scanning Electron Microscopy
HR-TEM	High-Resolution Transmission Electron Microscopy
FIB	Focused ion beam
XRD	X-ray diffraction
XPS	X-ray Photoelectron Spectroscopy
PVA	Polyvinyl alcohol
rGO	Reduce graphene oxide
GO	Graphene oxide
NF	Nickel foam
PTFE	Poly(tetrafluoroethylene)
GCD	Galvanostatic charge-discharge
EIS	Electrochemical impedance spectroscopy
FFT	Fast Fourier transformer
C_a	Areal capacitance
R_{ct}	Charge transfer resistance
R_s	Equivalent series resistance

Z'	Real impedance
Z''	Imaginary impedance
TMDs	Transition-metal dichalcogenides
EDS	Energy-dispersive X-ray spectroscopy
C_m	Specific capacitances
E_a	Anodic potential
E_c	Cathodic potential
E_o	Oxygen-evolution potential
E_{ac}	Potential difference between E_a and E_c
E_{oa}	Potential difference between E_o and E_a

Chapter 1

Introduction

1.1 Background

Due to climate change and the fast development of the global economy, energy has become a primary focus in the scientific and industrial communities. With concerns about environmental pollution, increasing mining costs and the depletion of fossil fuel, there is an urgent need for an efficient, clean and renewable energy source, and energy storage technique[1].

Although great efforts have been made on the development of high-performance Li-ion batteries and fuel cells[2-4], the poor power capability and high maintenance cost have kept them away from many applications. Recently, supercapacitors have drawn great attention because of their high charge-discharge rate, long life cycle, outstanding power density and no short circuit concern that are of concern with current batteries or fuel cells. Supercapacitors, also known as ultracapacitors or electrochemical capacitors, store energy with an electric double layer (EDL) capacitance achieved by ion adsorption or pseudocapacitance dominated by a surface redox reaction. Pseudocapacitors with conducting polymers or metal oxides as an electrode material, although demonstrating high capacitive performance, but cannot maintain this performance after prolonged cycling. On the other hand, EDL capacitors can be charged and discharged as many as one million cycles without performance degradation[5]. Furthermore, ion transportation is faster than a redox reaction, resulting in a high charge-discharge rate and power density in EDL capacitors. Currently, the energy density of EDL capacitors is generally 3-5 Wh/kg, which is one order of magnitude below commercialized lithium-ion batteries (100-275 Wh/kg)[6, 7]. Thus, increasing the energy capacity with minimum sacrifice of power density is now a major topic in supercapacitor research. Currently, the three major commercialized energy storage devices are capacitors, batteries and fuel cells.

The Ragone chart shown in Figure 1 is a standard method to visualize the energy storage performance of various devices[8]. The dash lines indicate the

time required to charge or discharge the device. From the chart, we can see that compared with batteries or fuel cells, conventional capacitors have very high-power density, but relatively low energy density. It means that a conventional capacitor can be charged or discharged very quickly and generate high power, but it cannot store much energy in unit mass or volume. On the other hand, batteries and fuel cells can store more energy but have a poor dynamic performance. Supercapacitors store more power than a battery and more energy than a capacitor. It means that supercapacitors can be charged or discharged very fast and maintain reasonable energy stored per unit mass. For this reason, it brings significant benefits in peak-power delivery applications, like regenerative braking, electric vehicle acceleration, and uninterruptible power supply.

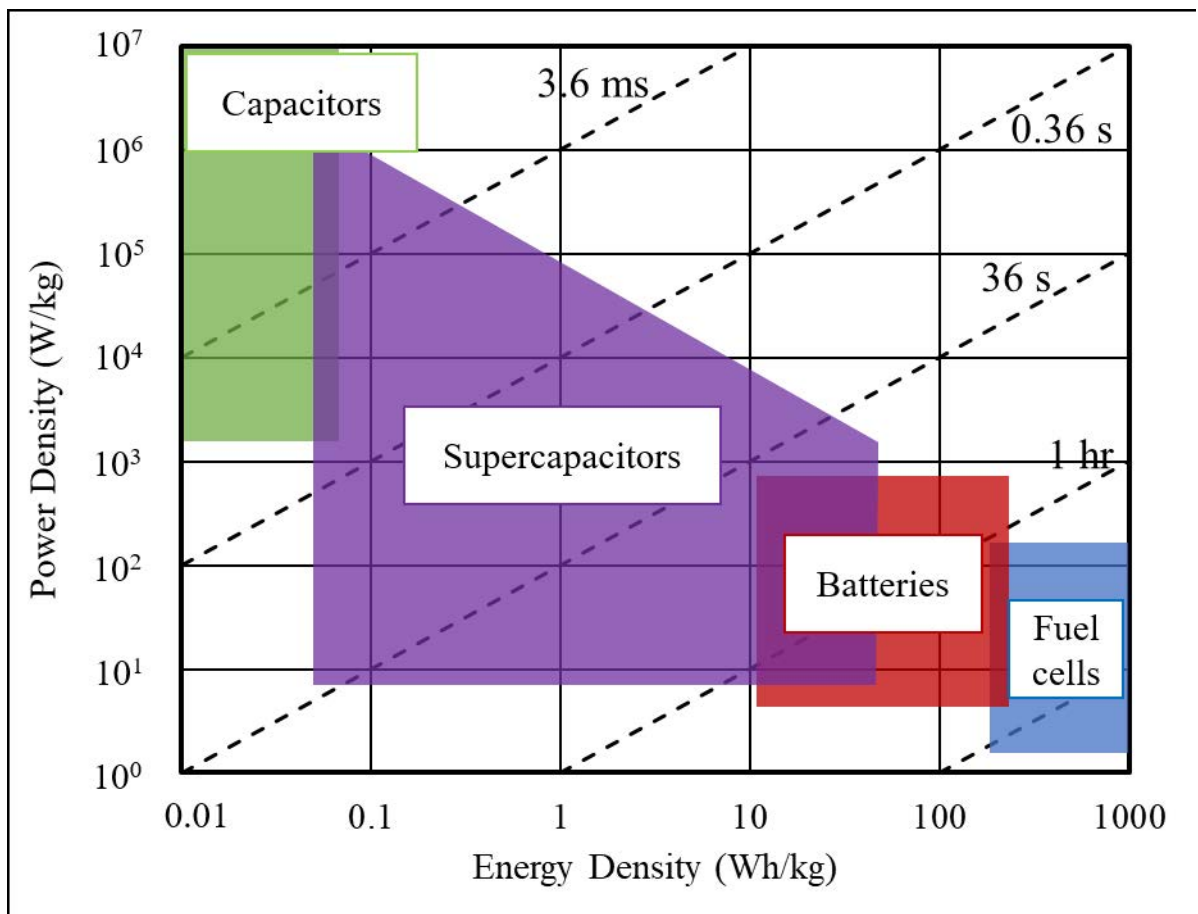


Figure 1 Ragone plot for various energy storage devices[8].

Besides bridging the power gap between capacitors and batteries, supercapacitors also hold many other desirable properties that make them a promising candidate for the next-generation energy storage device. The charge storing mechanism is a physical process without any chemical or phase change so that it is highly reversible and can be repeated for a large number of charge-discharge cycles, up to 1 million times[9, 10]. Also, they can be operated over a wide temperature range.

1.2 Types of Supercapacitors

There are three representative types of supercapacitors: (1) the electric double-layer capacitor (EDLC), (2) the pseudocapacitors, and (3) hybrid supercapacitors as shown in Figure 2.

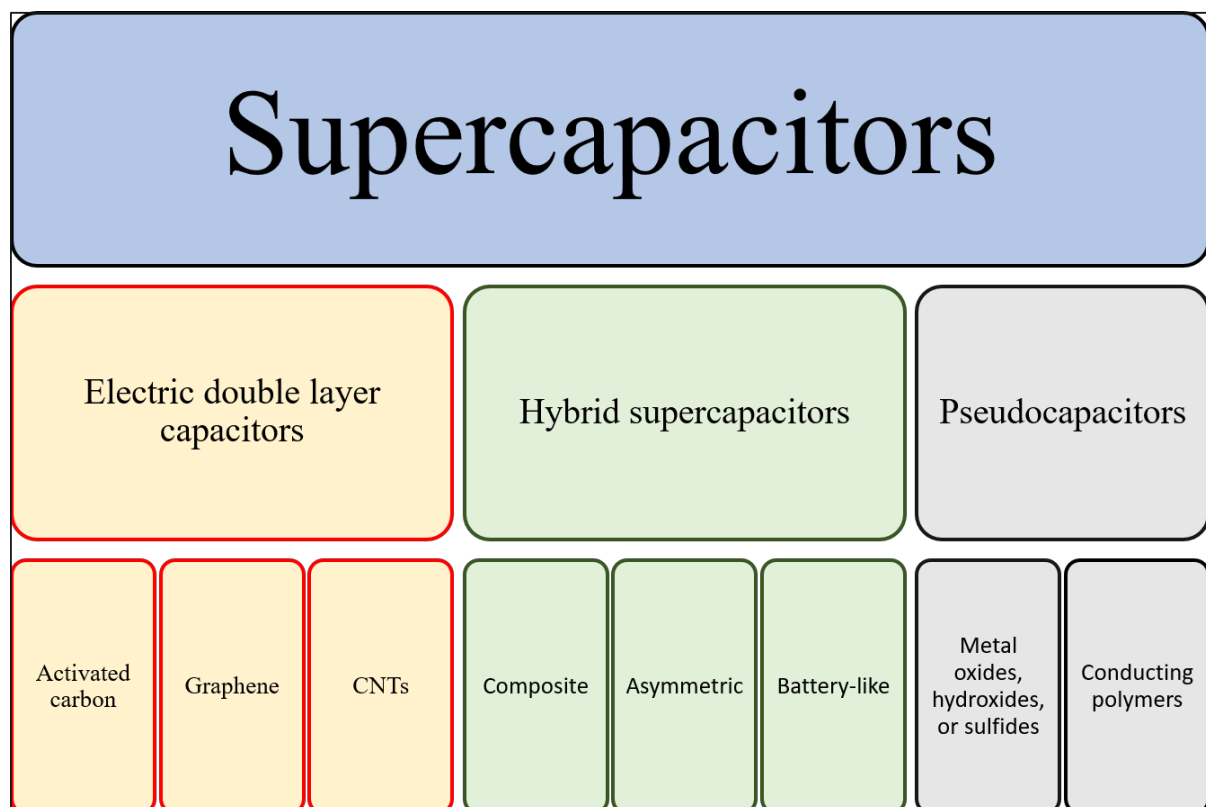


Figure 2 Taxonomy of supercapacitors.

1.2.1 Electric double-layer capacitance

EDL capacitors utilize the electric double layer to store charge. Various models were developed to illustrate the EDL charge distribution, as shown in Figure 3 [11]. Since typical electrolyte solvents used in supercapacitors are polar protic solvents (e.g. water and alcohols), so the cations are highly solvated, but the anions are not. The earliest model was reported by von Helmholtz in the 19th century in his research regarding the distribution of opposite charges at the interface of colloidal particles[12]. The Helmholtz model treats the EDL as a simple capacitor that two layers of opposite charges form at the interface of electrode and electrolyte separated from a distance. So, at the positively charged side, a layer of anions is adsorbed at the surface forming a linear electric potential profile. Unfortunately, this model does not consider the adsorption of water molecules and counter ions. Therefore, in the early 1900s, it was further modified simultaneously by Gouy and Chapman[13, 14] who have proposed that the distribution of electrolyte ions in the electrolyte medium is due to the thermal motion, named as a diffusion layer. The Gouy-Chapman model overestimates the EDL capacitance. It assumes that ions act like point charges and there is no physical limitation for ions' approach to the surface, which is not true. The capacitance of two separated arrays of charges is inversely proportional to the separation distance, so an extremely high capacitance would occur when point charge ions are close to the surface which does not meet with the actual case.

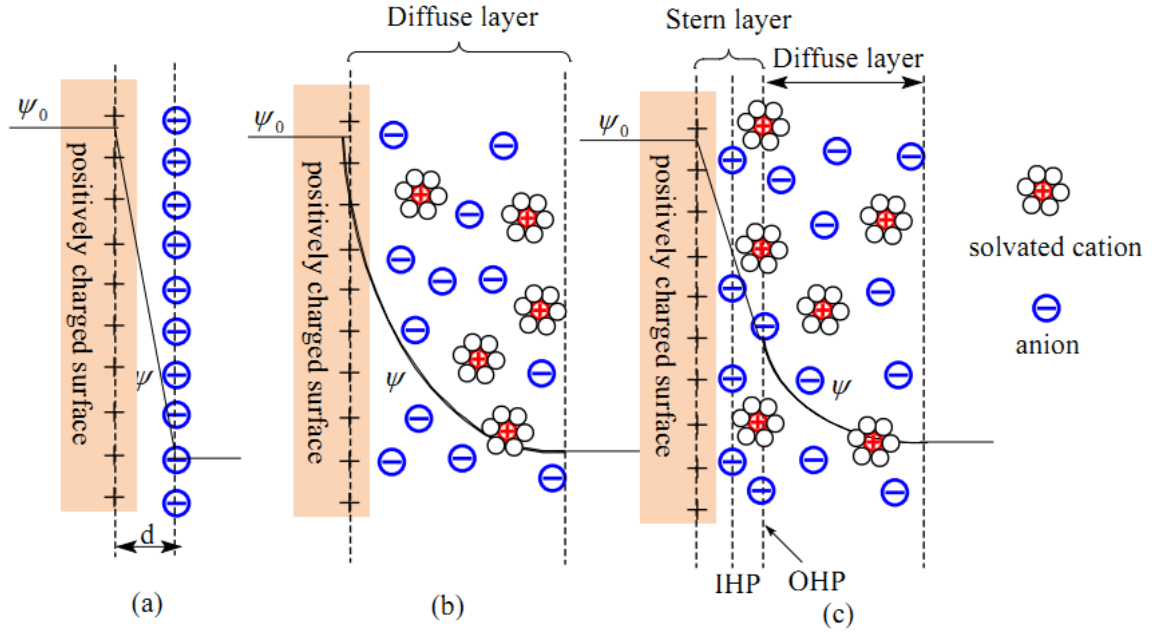


Figure 3 Schematic representation of electrical double layer structures according to (a) the Helmholtz model, (b) the Gouy-Chapman model, and (c) the Gouy-Chapman-Stern model[11].

So, in 1924, Stern[15] developed an alternate theory by combining the Helmholtz and Gouy–Chapman models, which explained the existence of two layers of ion distribution. The first layer is called a compact layer or the Stern layer or Helmholtz layer. It is formed by adsorbed ions and non-specifically adsorbed counter ions on the electrode, and these two types of adsorbed ions are distinguished as the inner Helmholtz plane (IHP) and outer Helmholtz plane (OHP). The second layer is called the diffusion layer, which is the same as what the Gouy–Chapman model described. So, total capacitance (C_t) is built up by both the layers, i.e., compact layer (Helmholtz layer) and the diffusion layer. The stored capacitance is termed as compact/Helmholtz double-layer capacitance (C_H) and diffusion layer capacitance (C_{diff}). So, the total capacitance can be expressed as follows[2, 4, 16]:

$$\frac{1}{C_t} = \frac{1}{C_H} + \frac{1}{C_{diff}}$$

1.2.2 Pseudocapacitance

Pseudocapacitors store energy through a faradaic reaction at the interface between electrode and electrolyte. These faradaic reactions include electrosorption, redox reactions and intercalation processes[17, 18]. To further improve the specific capacitance of the electrode, pseudocapacitive electrode materials like conducting polymers or metal oxides were utilized to make pseudocapacitors or added to the carbon-based materials to generate hybrid supercapacitors.

1.2.3. Hybrid

As we have seen EDLCs offer good cyclic stability, good power performance while in the case of pseudocapacitance it offers greater specific capacitance. In the case of the hybrid system, it offers a combination of both, that is by combining the energy source of a battery-like electrode, with a power source of a capacitor-like electrode in the same cell[19]. With a correct electrode combination, it is possible to increase the cell voltage, which in turn leads to an improvement in energy and power densities. Several combinations have been tested in the past with both positive and negative electrodes in aqueous and inorganic electrolytes. Generally, the faradic electrode results in an increase of energy density at the cost of cyclic stability, which is the main drawback of hybrid devices compared to EDLCs, it is imperative to avoid turning a good supercapacitor into an ordinary battery[20]. Currently, researchers have focused on the three different types of hybrid supercapacitors, which can be distinguished by their electrode configurations: Composite, Asymmetric, and Battery-type.

1.2.3.1 Composite

Composite electrodes combine carbon-based materials with either metal oxides or conducting polymer in a single electrode, this means a single electrode

will have both physical and chemical charge storage mechanisms. Carbon-based materials offer capacitive double-layer of charge and high specific surface area which increases the contact between pseudocapacitive materials and electrolytes. Through Faradaic reaction, pseudocapacitive material increases capacitance in composite electrode[21, 22]. Currently, there are two different types of composites: Binary and Ternary composites. Binary composites involve the use of two different electrode materials, while in the case of ternary it uses three different electrode materials to form a single electrode.

1.2.3.2 Asymmetric

Asymmetric hybrids combine faradic and non-faradic processes by coupling and EDLC with a pseudocapacitor electrode. The configuration of the asymmetric hybrid supercapacitor is arranged in such that the carbon material is used as a negative electrode while the metal oxide or conducting polymer as a positive electrode. The asymmetric hybrid supercapacitor achieves higher energy and power density than the EDLCs, and it has better cyclic stability than the pseudocapacitors[23-25].

1.2.3.3 Battery Type

Similar to an asymmetric hybrid supercapacitor, battery type hybrid combines two different electrodes, but in this case, they are fabricated by combining a supercapacitor electrode with a battery electrode. The battery type hybrid utilizes both properties of supercapacitors and batteries such as high energy density and long cyclic stability and short recharging time[26-30].

1.3 Electrode Materials

1.3.1 Activated carbon

Activated carbon (AC) is widely used as an electrode material in ELDCs due to its large surface area, good electrical conductivity, and low cost[31]. Several researches reported that there is a direct relation between the surface area of the AC and the capacitance, but the contribution of the surface area contribute to the capacitance is limited. This limitation is caused by too large electrolyte ions cannot diffuse into smaller pores and preventing these pores from the contribution to the capacitance[32-34]. Additionally, excessive activation results in large pore volume, which in turn leads to drawbacks like low conductivity and material density, which will lead to a low energy density and loss of power capability. Efforts have been made to see the effect of different electrolytes on the capacitance performance of AC. It was observed that the capacitance of AC is higher in aqueous electrolytes (ranging from 100 F/g to 300 F/g) as compared to organic electrolytes (<150 F/g)[35].

1.3.2 Carbon nanotubes (CNTs)

CNTs have a great as EDLCs electrode material due to its unique pore structure, good mechanical and thermal stability and superior electrical properties[36, 37]. Unlike other carbon-based electrodes, the mesopores in carbon nanotube electrodes are interconnected, allowing a continuous charge distribution that uses almost all of the available surface area. Thus, the surface area is utilized more efficiently to achieve capacitances comparable to those in activated-carbon-based supercapacitors, even though carbon nanotube electrodes have a modest surface area compared to activated carbon electrodes[37, 38].

Because the electrolyte ions can more easily diffuse into the mesoporous network,

carbon nanotube electrodes also have a lower ESR than activated carbon[39-41]. In addition, several fabrication techniques have been developed to reduce the ESR even further. Especially, carbon nanotubes can be grown directly onto the current collectors, subjected to heat-treatment, or cast into colloidal suspension thin films[40, 41]. The efficiency of the entangled mat structure allows energy densities comparable to other carbon-based materials and the reduced ESR allows higher power densities.

1.3.3 Graphene

Graphene is a 2D plane of sp^2 bonded carbon atoms, organized in a honeycomb lattice. There are two reasons why graphene is a particularly suitable material for storage devices. The first reason is that graphene has good electrical conductivity. The electrical conductivity is a result of graphene's unique electronic properties, which include a massless Dirac fermion, an ambipolar electric field effect, and an extremely high carrier mobility[42]. These properties arise from the unique electronic band structure of graphene, which is considered a zero-gap conductor[43]. Moreover, due to the high quality of its 2D crystal structure, graphene exhibits fast transport properties, which also results in a low defect density, allowing graphene to behave like a metal with a high constant mobility[44]. The second reason for graphene's suitability for electronic storage is its high surface area. The theoretical calculation of the specific surface area of graphene yields a value of 2630 m^2/g . This is a high specific surface area even compared with the graphite ($\sim 10 m^2/g$)[5] or CNTs (1315 m^2/g)[45]. These advantages make the graphene and their composites suitable for supercapacitor application. So far, a variety of methods have been developed to synthesis graphene. Among them, the impressive approaches include mechanical exfoliation of graphite[46], chemical vapor deposition of monolayer graphene[47], epitaxial growth on SiC substrate[48], unzipping of CNT[49] and so on. Generally, those methods can be classified into two routes: the top-down

and bottom-up approaches. Bottom-up methods can produce high-quality monolayer graphene, while top-down such as chemical exfoliation methods are described to give the highest throughput of graphene with trade-off like layer restacking and conductivity degradation. Some studies showed that the specific capacitance of graphene supercapacitor is 135 F/g in aqueous potassium hydroxide and 99 F/g in an organic electrolyte which still falls far below the theoretical value of 550 F/g calculated for single-layer graphene[50]. Overall, graphene undergoes the restacking or reattachment problems during electrochemical process, which is a main limitation for commercialization. The restacking or reattachment of graphene sheet is due to the π - π interaction and strong van der Waals force of attraction that exists between the graphene layers. Recently, researchers are finding different ways to inhibit the restacking of graphene layers like (i) hybrid composites and (ii) doping of graphene with heteroatom.

1.3.4 Metal Oxides

Many transition metal oxides thin film including ruthenium oxide, iridium oxide, manganese oxide, cobalt oxide, nickel oxide, tin oxide, iron oxide, perovskites, ferrites etc. have been investigated as electrode material for pseudocapacitors. Because of the cost consideration, inexpensive metal oxides with good capacitive values attracted considerable attention. Unlike the asymmetric cyclic voltammetry curves of conducting polymers with current peaks at the respective redox potentials, the CV curves of metal oxides like RuO₂ and IrO₂ electrodes have a near rectangular shape, as is expected for ideal capacitors. Hydrated forms of RuO₂ have been studied intensively for supercapacitors because of the high theoretical specific capacitance limit of 1358 F/g and electrical conductivity 300 S/cm[51]. Experimental specific capacitance up to 750 F/g and 800-1200 F/g were reported for electrodeposited RuO₂ and hydrated RuO₂ /carbon composites[51, 52]. The major disadvantage of metal

oxides is the low operating voltage. Materials like RuO₂ and IrO₂ can only be applied with aqueous electrolytes which set the voltage around 1V. Previously, RuO₂ electrode in H₂SO₄ electrolyte showed a maximum potential range of 1.4V[53].

1.3.5 Conducting Polymers

Conducting polymers, such as polyaniline (PANI), polypyrrole (PPy), poly-(3,4-ethylenedioxythiophene) (PEDOT) and derivatives of polythiophene, have a relatively higher capacitance and conductivity than carbon-based materials. Conducting polymers can store energy with not only EDL but also rapid faradic charge transfer. In general, conducting polymers are more conductive than the inorganic battery materials leading to a larger power capability. Moreover, the low ESR and manufacturing cost attracted a lot of interest into related research. However, conducting polymers are experiencing much lower cycle life than carbon electrodes because the redox sites in conducting polymer backbone are not sufficiently stable. The structure of polymer has a critical impact on the electrochemical performance by affecting the ion mobility and accessibility of pores. Thus, the design of polymer structure is important to get high charge storage efficiency and stability. Poly(Tri(4-(Thiophen-2-yl)Phenyl)Amine) (pTTPA) deposited into highly porous films or template nanotube structures yielded a remarkably high capacitance of 950 F/g in 100 mM tetrabutylammonium tetrafluoroborate in acetonitrile[54]. Graphene/CNT/PANI composites prepared via in situ polymerization exhibited the specific capacitance of 1035 F/g in 6M of KOH much higher than pure PANI capacitance[55]. Also improved cycle stability was observed in those composites, because graphene and CNT play a great role of backbone to generate a homogenous polymer distribution. It is known that conducting polymers are mechanically weak, so the composites can preserve the polymer from mechanical breaking in the long cycling[19].

1.4 Electrolytes

The key to reach high capacitance is using electrodes with high surface area and electrical conductivity. However, further researches reveal that even with high surface area materials, the device performance depends on the electrolyte as well. The performance of supercapacitors can be adjusted apparently by applying suitable electrolytes. There are three types of electrolytes used in the supercapacitor research: aqueous electrolyte, organic electrolyte and ionic liquid. Aqueous electrolytes such as KOH, NaOH and H₂SO₄ have smaller ion size that can utilize more surface area. The conductivities of acid and alkaline solutions are advantageously high owing to the proton transport resulting in a low ESR and high-power capability. However, the decomposition voltage of aqueous electrolyte is theoretically 1.23V or practically 1.3-1.4 V in kinetic terms[56]. Another concern of aqueous electrolyte is the corrosion nature of the acid or alkaline solution that may damage the electrode or other components of the device, leaving problems like reliability and self-discharge. Then, non-aqueous electrolytes were employed to break through the potential limit. Organic electrolytes, such as tetraethylammonium tetrafluoroborate and triethylmethylammonium tetrafluoroborate in acetonitrile, have been studied in supercapacitor with a relatively high potential window around 2-2.5 V. But the large organic solvent molecules set higher requirement of pore size of electrodes. And the drawbacks like electrolyte depletion upon charge and low safety also limit the use of organic electrolytes[57]. Ionic liquids, on the other hand, have a maximum operating voltage about 4-4.5V as well as a moderate ion size. AC supercapacitor cells filled with N-butyl-N-methylpyrrolidinium bis(trifluoromethanesulfonyl)imide (PYR14TFSI) ionic liquid demonstrated a high cycling stability for 40000 cycles and a high stable specific capacitance of 60 F/g[58]. Hence, the choice of electrolyte depends on reliability and performance requirements of each application of supercapacitors. To choose

between aqueous electrolyte, organic electrolyte and ionic liquid, we need to consider the tradeoffs between operating voltage range, specific capacitance and ESR or power density.

Conventional supercapacitors with liquid electrolytes consist of a separator as isolation between electrodes. But there is also a trend of using solid electrolytes like poly(vinyl alcohol) (PVA)-H₃PO₄ polymer gelled electrolyte. The use of those solid electrolytes results in a simplified fabrication process with no need for separator and no possible leakage of dangerous electrolyte.

1.5 Separators

A separator works as isolation for the two electrodes to prevent the combination of ions of opposite charge. For this purpose, the separators should be ideal insulator like with high resistance. The thickness of separator would determine the capacitance value the device can achieve. Ideally, it should be very thin in range of tens of microns. To maintain a low ESR, the separator should be very porous, and the pore size should be adjusted properly, so that the ions could be capable to diffuse across separator freely. Furthermore, they should be mechanically strong and chemically inert to protect the stability and conductivity of the electrolyte. The common separators used in research devices are nonwoven polypropylene (PP) membrane with a porosity of 40-60%.

1.6 Fabrication Methods of Electrode Materials

There are several synthesis methods of supercapacitors electrode materials. These methods include electrochemical deposition, chemical bath deposition, chemical vapor deposition and the sol-gel method.

1.6.1 Electrochemical deposition

Electrochemical deposition or electrodeposition is simple and economic coating method for metals and metal oxides on conductive substrate. Electrodeposition enables production of a uniform film on the conductive substrates with complex shape, while one can precisely control the film thickness by tuning the electrical charge delivered during the electrolysis. In electrodeposition method, a three-electrode configuration is used to deposit supercapacitor material as in Figure 4. The substrate is connected to the working electrode (WE), a platinum foil or carbon rod is used as a counter electrode (CE), and Ag/AgCl can be used a reference electrode (RE). The electrodeposition method has been used to deposit manganese oxide (MnO_2) of specific capacitance 364 F/g at 10 mV/s[59]. Also, RuO_2 has been deposited by the electrodeposition method and demonstrated a specific capacitance of 788 F/g[60]. Electrodeposition has also been employed to deposit conducting polymers such as PANI, which showed a specific capacitance of 437 F/g in 0.5 M H_2SO_4 at a scan rate of 10 mV/s[61].

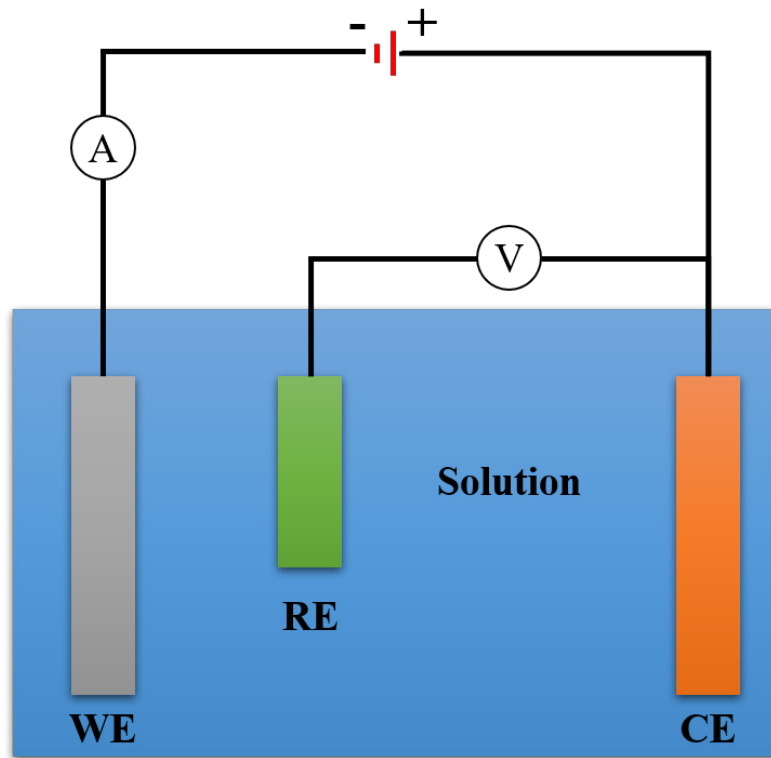


Figure 4 Scheme of electrochemical deposition technique.

Electrodeposition has many advantages, such as precise control of the thickness and uniformity, low cost, and mass production. However, it is time-consuming process, and process parameters must be optimized for each workpiece to obtain uniform thickness. Environmental concerns also arise from the process such as the acidic, alkaline, and cyanide discharge[62].

1.6.2 Chemical bath deposition (CBD)

Chemical bath deposition (CBD) is a low temperature technique that allows for relatively inexpensive deposition of material on large-scale substrates[63]. The CBD method involves the direct deposition of a material from a solution medium without the application of current or voltage. CBD occurs on a substrate immersed in a solution by means of a reaction from the solution containing different precursors dissolved either in ionic or molecular form. These

react chemically on the substrate, resulting in film formation by nucleation. Recently, a specific capacitance of 753 F/g at a scan rate of 5 mV/s in 0.5 M H₂SO₄ solution for PANI thin films which have been deposited by microwave assisted CBD[64]. The CBD method has also been used to synthesize ruthenium oxide (RuO₂) for supercapacitor electrodes. Thin films of RuO₂ synthesized by room temperature liquid phase CBD have been reported to exhibit a specific capacitance of greater than 400 F/g at a scan rate of 5 mV/s in 0.5 M H₂SO₄[60].

The advantages of the CBD are that the relatively low cost, large substrate area, and low temperature processing of CBD, another advantage is its relative simplicity, especially when compared to electrodeposition. However, the flexibility of the CBD method has been limited due to insufficient fundamental understanding and control of the underlying chemistry[65]. Another disadvantage of CBD is the low material yield for film formation[66].

1.6.3 Chemical vapor deposition (CVD)

The chemical vapor deposition (CVD) is a widely used processing technology to produce thin films. CVD process is achieved by exposing the heated substrate to appropriate gaseous reactants in the deposition chamber, as in Figure 5. The precursors undergo reaction or decomposition on the surface of the substrate and form the desired solid thin film or powder. Any volatile precursors produced during the process are removed by gas flow through the chamber. CVD has several advantages as a method for depositing thin films. One of the primary advantages is that CVD films are generally quite conformal, i.e., that the film thickness on the sidewalls of features is comparable to the thickness on the top. This means that films can be applied to elaborately shaped pieces, including the insides and undersides of features, and that high-aspect ratio holes and other features can be completely filled. Another advantage of CVD is that, in addition

to the wide variety of materials that can be deposited, they can be deposited with very high purity. This results from the relative ease with which impurities are removed from gaseous precursors using distillation techniques. Other advantages include relatively high deposition rates, and the fact that CVD often doesn't require as high a vacuum. CVD also has several disadvantages. One of the disadvantages, the precursors need to be volatile at near-room temperatures. CVD precursors can also be highly toxic ($\text{Ni}(\text{CO})_4$), explosive (B_2H_6), or corrosive (SiCl_4). The byproducts of CVD reactions can also be hazardous (CO , H_2 , or HF). The other major disadvantage is the fact that the films are usually deposited at high temperatures. This puts some restrictions on the kind of substrates that can be coated. More importantly, it leads to stresses in films deposited on materials with different thermal expansion coefficients, which can cause mechanical instabilities in the deposited films. The CVD method has been used to synthesize multiwalled carbon nanotubes and has been employed in flexible supercapacitor electrodes[67]. The CVD method also allows the synthesis of graphene-type materials. Three-dimensional networks of graphene have been prepared by CVD using ethanol as a carbon source[68]. These networks have been used as templates to make graphene/metal oxide composite supercapacitor electrodes showing specific capacitance of 816 F/g at a scan rate of 5 mV/s. Graphitic nanofibers have also been deposited by the CVD process for supercapacitor applications[69].

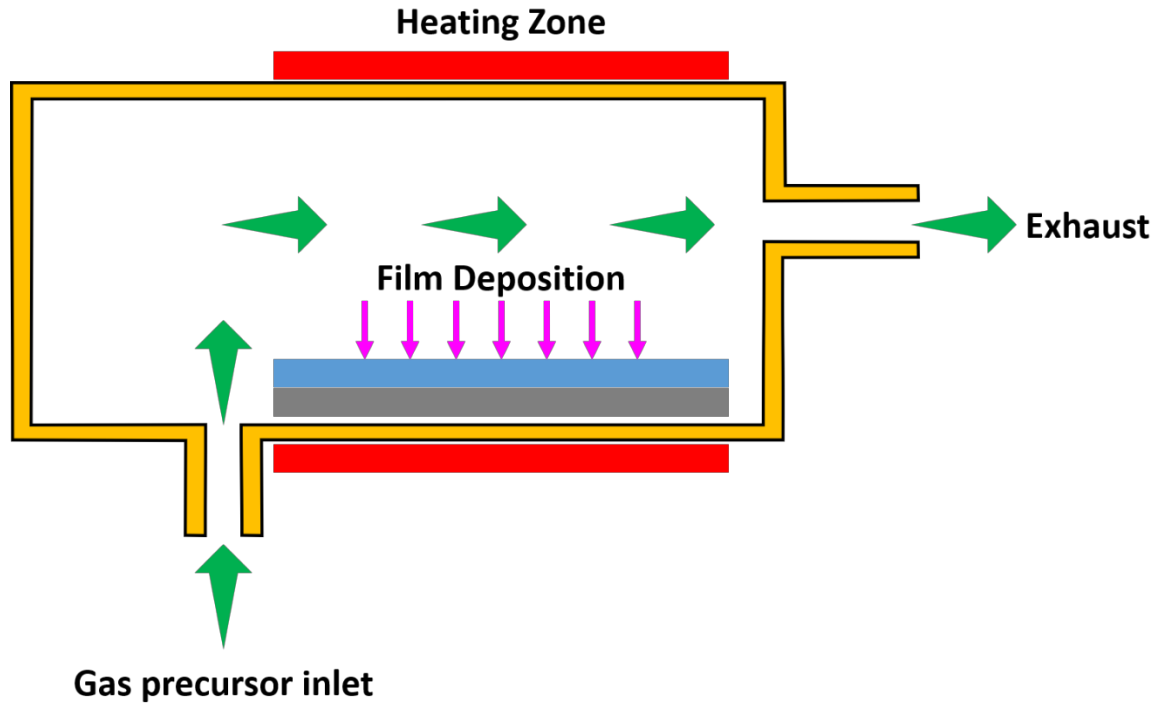


Figure 5 Schematic diagram of CVD.

1.6.4 Sol-gel

Sol-gel is a method used to form solid thin films, which involves preparation of a solution followed by its gelation and removal of the solvent[1]. The main advantages of the sol-gel process over conventional processes is that (i) better chemical homogeneity in multicomponent systems; (ii) relatively low sintering temperatures due to high surface area of the product; (iii) ability to maintain relatively high chemical purity as the processes of grinding, pressing etc. are not involved; and (iv) versatility to produce a variety of products in the form of monoliths, fibers, particles, coatings[70]. Disadvantages of sol-gel processes include the cost of the raw materials (especially alkoxide precursors), shrinkage of films during drying and sintering, and the fact that they are time consuming. One well-known application of a sol-gel process is thin-film coating, which benefits from most of the advantages of sol-gel processes while avoiding the disadvantages[71-73]. The sol-gel technique has been employed to synthesize

electrode materials for supercapacitors. For example, carbon aerogels are obtained from the carbonization of organic aerogels[74]. Other materials, such as high-surface area carbon-ruthenium xerogels, have also been derived from sol-gel methods and used to make electrodes with a specific capacitance of 256 F/g in carbon–metal oxide supercapacitors[75]. Among other materials, tin dioxide (SnO_2) nanocrystallites doped with antimony were synthesized by a sol-gel process and employed in SnO_2 based supercapacitors[76]. Amorphous hydrous ruthenium oxide/active carbon was prepared by a sol-gel based procedure and a specific capacitance of up to 715 F/g was obtained[77]. Amorphous manganese dioxide (MnO_2) made by the sol-gel method by reducing sodium permanganate (NaMnO_4) with solid fumaric acid has been employed as an electrode material[78].

1.7 Nano-Particle Deposition System (NPDS)

The nano-particle deposition system (NPDS) was developed in 2008 by Chun et al.[79-81]. NPDS was used to deposit nano/micro-sized ceramic and metal particles with sizes from 100 nm to 100 μm under room temperature and low-vacuum conditions. The deposition on several substrate types was reported by the NPDS such as metal, ceramic, polymer and paper substrates. Table 1 summarize the previous deposited materials and substrates. Also, no need for post-processes for the thin film deposited by the NPDS, so that the NPDS is considered low-cost and simple thin film deposition method. The NPDS has been used for some application including dye-sensitized solar cell (DSSC) and Electrochromic Device (ECD)[82, 83].

Table 1 Deposited materials using NPDS.

Deposited material		Substrate material	Ref.
Metal	Ni	Si Wafer	[84]
	Sn	PCB, PET, PP	[85]
		Glass, Sapphire	[85, 86]
		Paper	[85]
Ceramic	TiO ₂	Cu, Al, Stainless steel	[79]
		ITO-Coated glass	[82]
		PET, PE, ITO-Coated PET	[80, 87]
	Al ₂ O ₃	Cu, Al	[88]
		Si Wafer, Sapphire	[89]
	WO ₃	FTO and ITO glasses	[83]
NiO	Si, Ni-coated Si, and FTO-coated glass	[90]	
2D materials	Graphene	Cu, Stainless steel	[91, 92]
		Glass, Sapphire	
	Graphite	PET	

Figure 6 shows the schematic diagram of the NPDS. The NPDS comprised of an air compressor, powder feeder, nozzle, vacuum chamber, vacuum pump, and controller. The air compressor supplies compressed air as carrier gas to move micro-sized powders from the powder feeder to the nozzle. The power feeder controls the powders feeding rate by piston movement and brush. The powder was accelerated through a rectangular opening converging-diverging nozzle. The

main factors controlling the deposition are the nozzle design, and the pressure difference between the carrier gas pressure and chamber pressure, also, the third parameter is the stand-off distances (SoD) between the nozzle outlet and substrate.

The impact velocity of particles is a key factor for deposition and is directly affected by the flow. The flow can be controlled by various process parameters, such as carrier gas pressure, pressure in the deposition chamber, SoD, nozzle geometry, powder type, and powder size, among the most relevant ones.

The effect of SoD has been studied by CFD of the impact velocity of Al_2O_3 particles. The range of SoD was set from 1 to 7 mm and 2 mm step. The CFD results showed that the impact velocity of the particles increased with increasing SoD. This result was compared the mechanical properties observed for the Al_2O_3 deposited by NPDS. Small differences in impact velocities caused large changes in mechanical properties[89].

Another important factor affecting the deposition by NPDS are the powder particle size and the substrate hardness. Hyungsub et al.[90] reported that micro-sized and sub-micro NiO particles failed to deposit on the FTO glass by NPDS but the deposition was successfully carried out on Si and Ni-coated Si wafers, this may attributed to the hardness result shows, where the Si (10.850 GPa) and Ni-coated Si wafers (8.386 GPa) had higher hardness values than that of bulk NiO (7.724 GPa). However, FTO glass (6.633 GPa) had a lower hardness than NiO. This hardness difference may account for the failed deposition of micro-sized and sub-micro NiO particles on the FTO glass. During the impact between NiO micro-sized and sub-micro NiO particles and the FTO glass, part of the kinetic energy is dissipated in the deformation process, resulting in deposition, and part is converted elastically to the kinetic energy of rebound. If this rebound energy exceeds the adhesion energy, the particles rebound, resulting in no deposition. Such particle rebound is most likely to occur when the particles are larger and harder than the substrate. For the case of hard substrate–soft particle combination,

the initial kinetic energy of the particle was mostly dissipated into plastic deformation, flattening the particle with a very slight deformed substrate. Which explains the success of NiO deposition on Si and Ni-coated Si wafers[90]. The effect of the particle size on the NPDS deposition was reported for NiO, smaller size of NiO particles (100 nm or less) show the high flow velocity, but because of the small moment of impact, the maximum impact velocity extremely decreased. So that, nano-sized NiO particles were deposited by breaking up of agglomerates and formed the loosely compact coating layer. Moreover, micro-sized NiO particles which have the highest impact velocity, can well deposited by deformation and fracturing of particles, forming the densely compact coating layer[90].

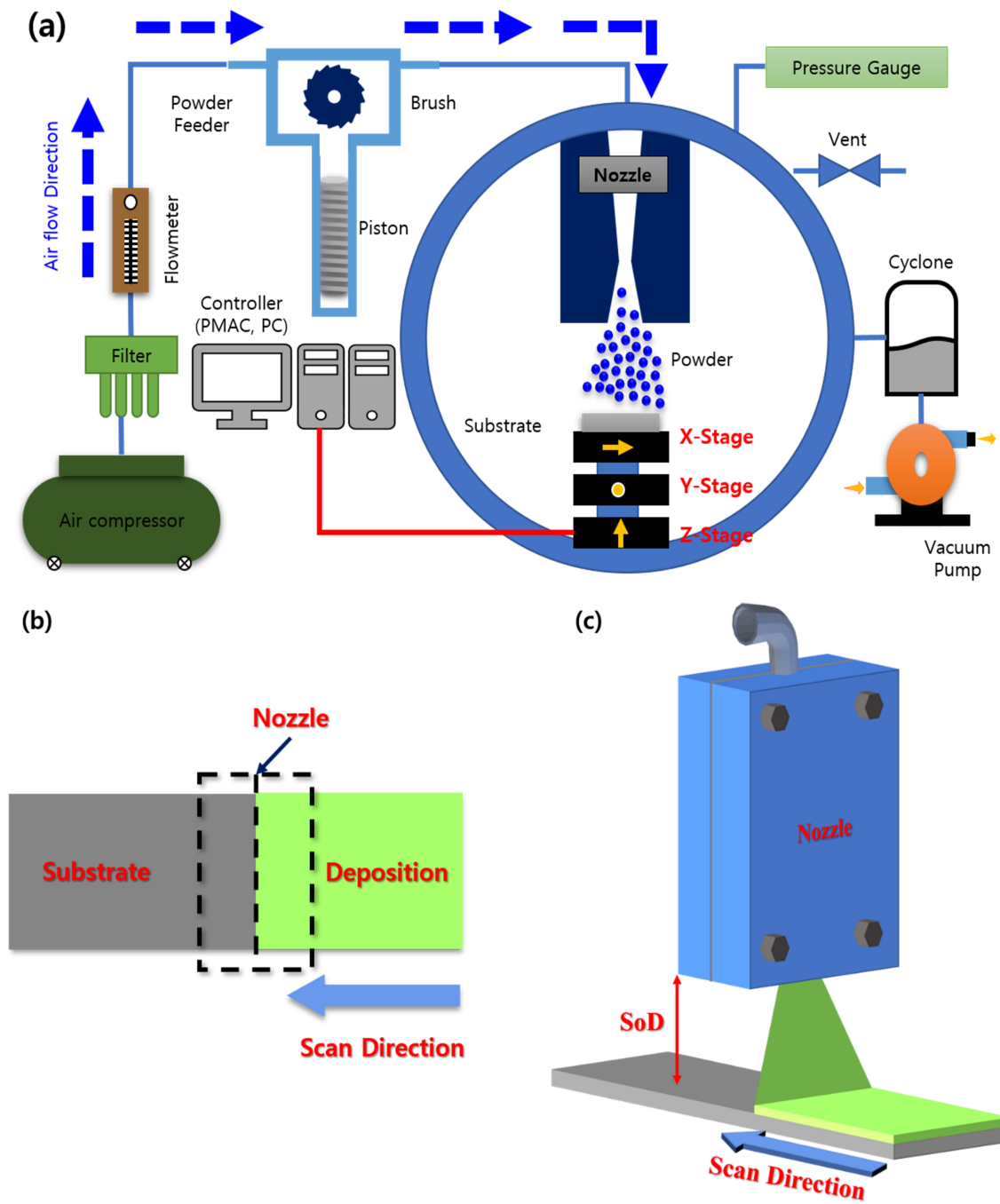


Figure 6 (a) schematic diagram of the NPDS, (b) top view, and (c) perspective view of the deposition processes.

Table 2 Different synthesis methods of electrode materials in terms of advantages and disadvantages

Synthesis methods	Advantages	Disadvantages
Electrochemical deposition	Large area deposition, low-cost, precise control on film thickness and uniformity	Post-processes (drying or annealing), long processes time and toxic chemicals
Chemical bath deposition	Simplicity, low temperature, low-cost, large area	Low yield, limited flexibility
Chemical vapor deposition	Good film uniformity, high purity, high deposition rate	Expensive equipment, high vacuum, volatile precursors
Sol-gel	Low-cost, controllable film texture, homogeneity	Weak bonding, complicated process
Nano-particle deposition system	Room temperature, low vacuum, simple process, large area deposition	Large feedstock

The comparison between NPDS and other synthesis methods in Table 2 indicate that NPDS is a direct deposition technique at room temperature and low vacuum conditions.

1.8 Research Motivations and Objectives

The improvement of supercapacitors is associated with many essential problems, such as low energy density, low operating potential, and high equivalent series resistance. The energy density of commercial supercapacitors that are based on carbon electrodes is generally less than 10 Wh/kg, which is much lower than that of batteries, 100 Wh/kg. Although pseudo-capacitive electrodes offer high energy density supercapacitors, but they suffer from poor rate capability and poor cycling stability. In contrast, pseudo-capacitive materials are expensive compared to carbon materials. Therefore, there is a huge demand to improve the electrochemical performance of pseudo-capacitive materials. Organic electrolytes and ionic liquids with broad operating potential windows offer relatively higher energy density. However, organic electrolytes have poor electrical conductivity and are not environmentally friendly, while ionic liquids are not cost-effective. Therefore, both types of electrolytes have been undesirable for practical applications. Considering the environmental concerns and cost, aqueous electrolytes are more desirable when configured with smart supercapacitors using proper electrode materials. Based on the above considerations, the intention of this dissertation research is to develop hybrid electrode materials that have enhanced electrochemical performance in terms of specific capacitance, energy and power densities and cycling stability.

The main objective of this research is to develop graphene-based hybrid electrodes such as molybdenum disulfide/graphite and nickel hydroxide/graphene hybrids for electrochemical supercapacitors with the following considerations.

- To study the deposition behavior of some 2D material such as few-layer graphene nano-flakes, molybdenum disulfide (MoS_2), nickel hydroxide

(Ni(OH)₂) and their composites with graphene using the nano-particle deposition system (NPDS).

- To maximize the specific capacitance of the deposited graphene-based composite electrodes by changing the graphene content in the composites.
- To improve the energy density of the asymmetric supercapacitor using Ni(OH)₂-graphene as a positive electrode.

1.9 Thesis Organization

The structure of this thesis can be summarized as follows.

Chapter 1 focuses on the literature review on supercapacitors including energy storage principles, electrode materials, electrolytes and separators. Then chapter 1 reviews the synthesis techniques of the supercapacitor electrode materials and their advantages and disadvantages. The latter part of Chapter 1 describes the motivations, and the objectives of carrying out this thesis work followed by the organization of the thesis.

Chapter 2 discuss the chemical and physical characterization techniques of electrode materials, and the evaluation of the electrochemical performance of the supercapacitors.

Chapter 3 reviews the deposition of few-layer graphene nano-flakes using different deposition parameters, their characterization and applications to symmetric supercapacitor. The electrochemical performance of the few-layer graphene nano-flakes symmetric supercapacitor in different electrolytes concentration is presented.

Chapter 4 describes the deposition and characterization of MoS₂-graphite hybrid electrode for symmetric supercapacitor. The capacitances of the MoS₂-graphite hybrid electrodes based symmetric supercapacitor are optimized based on the amount of MoS₂ content used in the deposition.

Chapter 5 focuses on the Ni(OH)₂ deposition and application to supercapacitors. In this chapter the structural and electrochemical performance of the Ni(OH)₂ deposited with different parameters on nickel sheets are compared. The Ni(OH)₂ deposition on nickel foam and its application to supercapacitor is presented in this chapter.

Chapter 6 describes the deposition of nanostructure Ni(OH)₂-graphene hybrid electrodes. The capacitance of Ni(OH)₂-graphene hybrid is maximized based on the content of the Ni(OH)₂ in the hybrid electrode. An asymmetric supercapacitor fabricated based on Ni(OH)₂-graphene hybrid electrodes are described in this chapter with performance comparisons.

Chapter 7 concludes the thesis with major findings in terms of increasing specific capacitance and operating voltage to increase the energy density of supercapacitors. The latter part of this chapter focuses on future research recommended for the development of hybrid materials as electrode materials for supercapacitor applications.

Chapter 2

Experimental Section

2.1 Materials

Graphite powder (MGF 10 995A) was purchased from Samjung C&G, Korea with a particle size of 10 μm or larger. Molybdenum (IV) sulfide powder MoS_2 , average particle size $< 2 \mu\text{m}$, 99% (#1317-33-5) and Nickel (II) hydroxide (#12054-48-7) were purchased from Sigma-Aldrich. Stainless-steel sheets of 0.5 mm thickness and nickel sheets of 0.2 mm thickness were purchased from Nilaco Corporation, Japan. Nickel foam with a thickness of 1.6 mm was purchased from Invisible Inc., Gyeonggi-do, Korea. Polyvinyl alcohol (PVA) with an average molecular weight of 88000 g/mol (#6716-1405), phosphoric acid (H_3PO_4) with 85% purity (#7664-38-2), and Potassium hydroxide (KOH) $> 93 \%$ (#1310-58-3), sodium nitrate (NaNO_3) with purity 99% (#7631-99-4), sulfuric acid (H_2SO_4) with purity 98% (#7664-93-9), potassium permanganate (KMnO_4) with purity 99.3% (#7722-64-7), sodium borohydride (NaBH_4) with purity 97% (#16940-66-2), and hydrazine hydrate (N_2H_4) with purity 80% (#7803-57-8) were purchased from Daejung, Gyeonggi-do, Korea. Hydrochloric acid (HCl) with purity 35~37% (#7647-01-0), and hydrogen peroxide (H_2O_2) with purity 34.5% (#7722-84-1) were purchased from Samchun Chemical Co., Ltd., Seoul, Korea.

2.2 Materials Preparation

The material preparation and deposition parameters corresponding to different electrode materials are introduced in their related chapters.

2.3 Characterization Techniques

2.3.1 Field Emission-Scanning Electron Microscopy (FE-SEM)

SEM uses a condensed, accelerated electron beam to focus on a specimen. The electron beam hits the specimen and produces secondary and backscattered electrons. Secondary electrons are emitted from the sample and collected to create an area map of the secondary emissions. Since the intensity of secondary emission is very dependent on local morphology, the area map is a magnified image of the sample. In this thesis work, SEM images were measured by scanning electron microscopy (JSM-6500F, Jeol, Japan)

2.3.2 High-Resolution Transmission Electron Microscopy (HR-TEM)

Before measurement, focused ion beam (FIB) (Helios NanoLab 450, FEI, Netherlands) milling was carried out to prepare the HR-TEM sample. A FIB lift-out TEM grid (Omniprobe, FIB lift-out Cu TEM grid with 3 posts) was used to hold the milled HR-TEM sample. Finally, the sample prepared by the FIB was used for high resolution transmission electron microscopy (JEM-2100F, Joel, Japan).

2.3.3 X-Ray Diffraction (XRD)

X-ray diffraction (XRD) takes advantages of the coherent scattering of x-rays by polycrystalline materials to obtain a wide range of structural information. The x-rays are scattered by each set of lattice planes at a characteristic angle, and the scattered intensity is a function of the atoms, which occupy those planes. The scattering from all the different sets of planes results in a pattern, which is unique to a given compound. The peaks of this pattern is formed when a constructive interference between the reflected x-rays by the atomic planes takes place satisfying Bragg's law ($n\lambda=2d \sin \theta$) satisfied where λ is the x-ray wavelength, d

is the spacing distance and θ diffraction angle. The crystallite size can be calculated using the Scherrer equation:

$$D = \frac{\kappa\lambda}{\beta \cos \theta} \dots\dots\dots 2.1$$

where, κ is a constant (usually = 0.9), and β is the full width at half maximum intensity (FWHM)[93]. In the thesis crystalline structure was identified using by X-ray diffraction Ultima IV, Rigaku, Japan (Cu K α radiation, $\lambda=0.15418$ nm) operated at 40 kV and 30 mA.

2.3.4 Raman Spectroscopy

Raman spectroscopy is a spectroscopic technique used to study vibrational, rotational, and other low-frequency modes in a system. It relies on inelastic scattering or Raman scattering of monochromatic light, usually from a laser in the visible, near infrared, or near ultraviolet range. The laser light interacts with phonons or other excitations in the system, resulting in the energy of the laser photons being shifted up or down. The shift in energy gives information about the phonon modes in the system. In this thesis work, the Raman spectra were carried out using a using Raman spectroscopy (Alpha 300R, WITec, Germany) with a 532 nm wavelength laser operating at 1 mW as an excitation source.

2.3.5 X-ray photoelectron spectroscopy (XPS)

Chemical state of a sample is analyzed by X-ray Photoelectron Spectroscopy (XPS). An electron is emitted by the photoelectric effect when homogeneous light is applied material. The measuring method of electron energy and intensity distribution is called XPS method.

$$E_{kin} = h\nu - E_b - \phi \dots\dots\dots 2.2$$

where E_{kin} is the kinetic energy of emitted photoelectron, $h\nu$ is the incident X-ray energy, E_b is the binding energy of emitted electron, and ϕ is the work function for sample. If $h\nu$ is constant, binding energy can be obtained by measuring the kinetic energy of emitted electron. Identification of element is easily possible by measuring E_{kin} because binding energy of each electron orbit is different. On the other hand, binding energy of same orbit of same element is changed a little by an atomic surrounding state and environment. State analysis of element is possible by measuring this change variation called chemical shift. X-ray photoelectron spectroscopy was performed with K-alpha XPS system (Thermo Fisher Scientific, Waltham, MA, USA).

2.4 Electrochemical Performance

The symmetric capacitors were assembled from two identical working electrodes and polymer gel electrolyte. The polymer gel electrolyte was prepared as follows. 1 g of PVA was stirred in 10 ml of deionized water at 80 °C for 2 hours until completely dissolved. After cooling, 0.03 mol (2.94 gm) of H_3PO_4 were added to the PVA and stirring was continued until the solution became a viscous gel. The same procedure was followed to prepare 0.06 and 0.09 mol of H_3PO_4 -PVA gel electrolyte by adding 5.88 and 8.82 gm of H_3PO_4 to the 1 gm of PVA respectively.

1x1 cm² of the deposited thin films on stainless steel (few-layer graphene in chapter 3 and MoS₂-graphite in chapter 4) were dipped on the H_3PO_4 -PVA gel electrolyte for a few minutes as in Figure 7 (a), and two identical electrodes were allowed to dry for 3 hours at room temperature. After this, the two identical electrodes were sandwiched together. The structure of the fabricated supercapacitor is shown in Figure 7 (b).

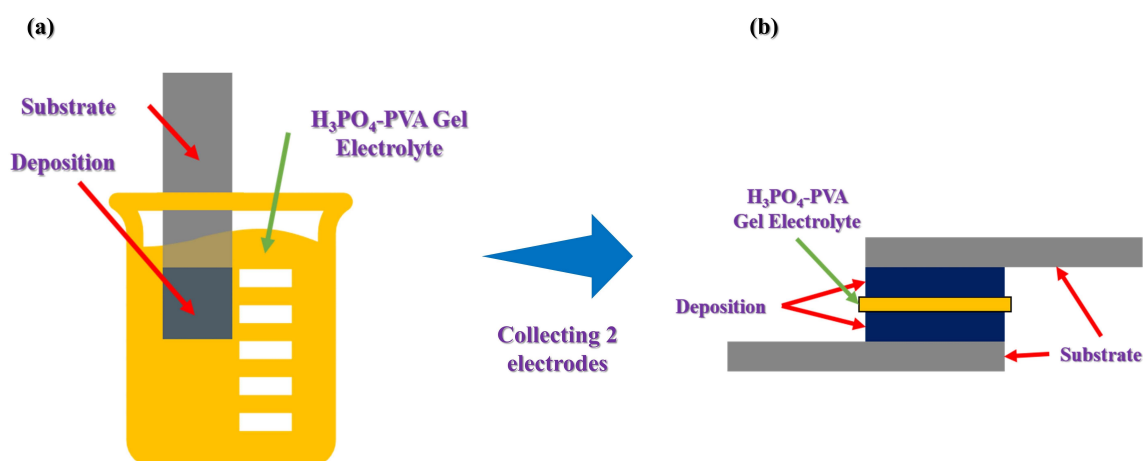


Figure 7 (a) dipping deposited electrode into the gel electrolyte; (b) assembly of the fabricated supercapacitor.

After cell fabrication, the electrochemical properties were measured using a two-electrode cell. The electrochemical performance was measured using the CorrTest electrochemical workstation (C350, Wuhan Corrtest Instruments Corp. Ltd., China), using cyclic voltammetry, galvanostatic charge/discharge, and electrochemical impedance spectroscopy. The cyclic voltammetry measurement was scanned between 0 and 1 V with different scan rates ranging from 2 to 100 mV/s. The galvanostatic charge/discharge tests were performed with different current densities (0.01 to 0.1 mA). Impedance data were collected from a 1 MHz to 1 Hz frequency range with an AC signal of 10 mV in amplitude.

For three-electrode configuration, the deposited samples by the NPDS were used as working electrodes. For the rGO samples, the working electrode was prepared for by mixing the rGO, carbon black, and polytetrafluoroethylene (PTFE) binder (ratio 85:10:5 wt.%) with few drops of ethanol to form a slurry. Then, the slurry was pressed into a nickel foam current collector and dried at 120°C overnight. The electrochemical measurements were carried out using CV and GCD in a 3-electrode cell. Pt mesh and Ag/AgCl electrode were used as the counter electrode and the reference electrode in 2M KOH electrolyte.

The electrochemical performance of the asymmetric supercapacitor was measured in a 2-electrode cell. The 10% Ni(OH)₂-Gr hybrid electrode and rGO electrode were sandwiched together, with cellulose filter paper soaked in 2 M KOH aqueous solution used as a separator. The masses of the positive and negative electrodes were balanced according to the following equation:

$$\frac{m_+}{m_-} = \frac{C_- \times \Delta V_-}{C_+ \times \Delta V_+} \dots\dots\dots 2.3$$

where *m* is the loading mass, *C* is the specific capacitance, and ΔV is the potential window for the positive (+) and negative (-) electrodes, respectively.

The specific capacitance, energy and power density of the ASC were calculated based on the total mass two electrodes in the ASC, according to the following equations:

$$C_m = \frac{I t_d}{m \Delta V} \dots\dots\dots 2.4$$

$$E = \frac{1}{2} C_m V^2 \dots\dots\dots 2.5$$

$$P = \frac{E}{t_d} \dots\dots\dots 2.6$$

where *C_m* is the specific capacitance of the ASC, *E* is energy density, *P* is the power density, *I* is the current, *m* is the total mass two electrodes, *V* is the maximum voltage applied during the charge/discharge measurement, and *t_d* is the discharge time determined from the discharge curve.

Chapter 3

Symmetric Supercapacitor

Fabricated Based on Few-

Layer Graphene Nano-

Flakes

3.1 Background

Supercapacitors, also called ultracapacitors, are promising electrochemical storage device due to their high-power density, fast charge/discharge rates and long charge-discharge cycles[5, 6, 8, 94]. Supercapacitors have the potential to supplement or replace the use of batteries for energy storage applications, namely those for wearable and portable electronics, energy storage systems, and electrical and hybrid vehicles[95]. There are two representative types of supercapacitor: (1) the electric double layer capacitor (EDLC) and (2) the pseudocapacitor. EDLCs store energy via ion adsorption/desorption on the electrode surface, exhibit an excellent cycle life and power density, but are restrained by limited adsorption capacity, which adversely impacts their energy density[96]. Carbon materials with a large specific surface area and excellent electrical conductivity, such as active carbon (AC), carbon nanotubes (CNTs), and graphene, have been used for EDLCs. In contrast, pseudocapacitors store energy via fast and reversible surface redox reactions. Typical pseudo-capacitive materials include transition metal oxides/hydroxides and conducting polymers. Pseudocapacitors hold a much higher energy density but have unsatisfactory cycle stability and rate capability, so power their density is generally low[96].

Graphene is a 2D plane of sp^2 bonded carbon atoms, organized in a honeycomb lattice. There are two reasons why graphene is a particularly suitable material for storage devices. The first reason is that graphene has good electrical conductivity. The electrical conductivity is a result of graphene's unique electronic properties, which include a massless Dirac fermion, an ambipolar electric field effect, and an extremely high carrier mobility[42]. These properties arise from the unique electronic band structure of graphene, which is considered a zero-gap conductor[43]. Moreover, due to the high quality of its 2D crystal structure, graphene exhibits fast transport properties, which also results in a low defect density, allowing graphene to behave like a metal with a high constant

mobility[44]. The second reason for graphene's suitability for electronic storage is its high surface area. The theoretical calculation of the specific surface area of graphene yields a value of 2630 m²/g. This is a high specific surface area even compared with the graphite (~10 m²/g)[5] or CNTs (1315 m²/g)[45]. These advantages make the graphene and their composites suitable for many applications, such as all-solid-state laser scribed flexible graphene supercapacitor[97], flexible and durable graphene oxide fabricated on cotton textile[98], electrochemically doped graphene[99], graphene/polyaniline nanofiber composite[100] and activation of microwave exfoliated GO (MEGO) and thermally exfoliated GO (TEGO) by KOH[101] for supercapacitor applications. And cuprous oxide/reduced graphene oxide (CuO₂/rGO) nanocomposites for light-controlled conductive switching[102]. Also CuO₂/rGO exhibits excellent photocatalytic activity[103], and AgInZnS-graphene oxide (GO) nanocomposites can be used as active biomarkers for noninvasive biomedical imaging[104]. Besides that, there are other properties about graphene and their composites such as the excellent mechanical properties and chemical tunability of graphene oxide paper reported by Dikin et al.[105]. However, there is drawback which limits use of graphene in some applications which is that the measured values of the graphene specific surface area are much lower than the theoretical value, in the range of 1000 and 1800 m²/g[106]. The lower specific surface area is a result of graphene agglomeration during fabrication of the electrode material, resulting in a loss of surface area[107].

In 2004, Geim and co-workers synthesized the first graphene single layers by mechanical exfoliation using the Scotch tape method[46]. Because of the manual operation, this method has a very small yield, but the graphene obtained by this method was useful for fundamental studies. This method is neither scalable nor can it be adapted for mass production[46, 108]. There are two major approaches for producing single layer graphene, the top-down and bottom-up

approaches. The purpose of the top-down approach is to reduce the graphite to single or few-layer graphene platelets. Graphite conversion into graphite oxide is a common method in the top-down strategies[105, 109]. This familiar top-down approach often requires strong reaction conditions, such as high reduction temperatures, while using concentrated sulfuric acid with highly hazardous procedures[110-112]. Moreover, the obtained graphene always suffers from many defects in the structure rendering its actual electric conductivity poor, thus restricting its applications[113]. The electrochemical exfoliation method has been reported to be promising for the large-scale production of high-quality graphene, however, this approach consumes a large amount of electric energy and the use of high voltages also facilitates the generation of oxygen groups, as well as structural damage of the graphene[110, 114]. Also, liquid-phase exfoliation[115] and graphite intercalation compounds (GICs)[116] are all included in the top-down approaches. The advantages of these approaches are that they produce a large area, with a low cost of fabrication. However, many defects are formed through the exfoliation, so it is impossible to get high-quality single-layer graphene[117]. The bottom-up methods require atom by atom growth, which includes growth on SiC, molecular beam epitaxy, chemical vapor deposition, and chemical synthesis[118]. CVD is a method in which graphene is grown directly on a transition metal substrate through saturation of carbon upon exposure to a hydrocarbon gas at a high temperature[119-125]. One of the major advantages of the CVD technique is its high compatibility with the current complementary metal–oxide–semiconductor (CMOS) technology. However, controlling the film thickness is difficult, and the formation of secondary crystals cannot be avoided[126]. Another disadvantage of the CVD method is that it requires expensive substrate materials for graphene growth, which limits the applications for large-scale production. Further, the transfer to another substrate is a complex process.

To avoid the disadvantages of the previous strategies, a promising vacuum kinetic spray method was used to deposit few-layer graphene nanoflakes from graphite microparticles, while under room temperature and low vacuum pressure conditions. This vacuum kinetic spray method is known as a nanoparticle deposition system (NPDS). Previously, a NPDS was developed to deposit metals and ceramics, such as tin, nickel, Al_2O_3 , TiO_2 , and WO_3 , at a low temperature. Additionally, few-layer graphene nanoflake layers have been successfully deposited[79, 80, 91, 92, 127, 128]. The NPDS uses relatively low pressure compressed air as a carrier gas and a low vacuum pressure (around 0.04 MPa), for low equipment and processing costs. The impact velocity of the micro-sized graphite particles deposited by NPDS is one of the critical process parameters, and its importance was studied with regard the formation of few-layer graphene flakes on copper foil without binders by Nasim and Chun[92]. Further, these researchers carried out computational fluid dynamics (CFD) simulations to study the relationship between the stand-off distance and the impact velocity. The CFD analysis predicts the critical velocity for fragmentation and interlayer separation of graphite particles for deposition of a few-layer graphene flake structure on copper, without the presence of unfragmented graphite particles[92]. Another important factor which can affect the deposition of micro-sized graphite particles is the substrate hardness. The substrate-dependent behavior of deposition showed that the degree of fragmentation and interlayer separation increase with an increase in the substrate hardness. By using the NPDS, thick and fragmented graphite particles were deposited on soft substrates, while the deposition on the hard substrates result in a few-layer graphene flake structure[91].

This research introduces a new deposition method for few layered graphene nano-flakes thin film from micro-sized graphite powders without any additives or chemicals so that this deposition method is low-cost, and eco-friendly manufacturing technique. The few layered graphene nano-flakes thin film

prepared by the NPDS is a novel for supercapacitor applications. Herein, the effect of the scan speed on the formation of a few-layer graphene flake structure was studied, and graphite microparticles were deposited on stainless steel using the NPDS for application in relatively low-cost supercapacitors. The surface morphology of the formed films was analyzed by a field-emission scanning electron microscope (FE-SEM), X-ray diffraction (XRD), and Raman spectroscopy. Then, the few-layer graphene nanoflake thin film was used as an electrode of a supercapacitor, with a polyvinyl alcohol with phosphoric acid (PVA-H₃PO₄) gel electrolyte serving as a separator and binding material[129]. A polymer gel electrolyte is often used to provide anions and cations, which participate in the surface process contributing to the electrochemical capacitance[130]. The electrochemical performance was evaluated in a 2-electrode system using cyclic voltammetry (CV), galvanostatic charge-discharge, and electrochemical impedance spectroscopy (EIS).

3.2 Materials and Methods

3.2.1 Graphene electrode preparation

The NPDS consists of a compressor, cylindrical powder feeder, nozzle, vacuum chamber, vacuum pump, vibrator, and controller, as shown in Figure 6. The compressor supplies a compressed air of pressure 0.2 MPa to carry the micro-sized graphite powder from the cylindrical powder feeder to the nozzle which is inside the vacuum chamber. In this research, a slit converging-diverging nozzle of dimensions 50 x 0.2 mm² was used to accelerate the powder for a large area deposition. A vibrator was used to shake the powder feeder to carry the powder easily to the nozzle. The distance between the nozzle and the stainless-steel substrate was set to be 5 mm. The y-stage is connected to permanent magnet AC (PMAC) motor to control the scan speed of the substrate. In this study the

deposition was carried out directly on a stainless-steel substrate by three different scan speeds without any additional chemical or binders as shown in Table 3.

Table 3 Process parameters for graphite deposition on the stainless-steel substrate.

Parameter	Value
Compressor pressure (MPa)	0.2
Chamber pressure (MPa)	0.036-0.04
Scan speed (mm/min)	0.4, 0.8, and 1.2
Distance between substrate and nozzle (mm)	5
Deposition shape	2x5 cm²
Substrate material	Stainless-steel

3.3 Results and Discussion

3.3.1 Morphology properties

After deposition, the masses per unit area and thicknesses of the deposited films with different scan speeds were calculated. The mass per unit area of the deposited films decreased as the scan speed increased from 0.4 mm/min to 0.8 mm/min and 1.2 mm/min. The thickness of each deposited film was measured by confocal microscopy, showing that as the scan speed changed from 0.4 to 1.2 mm/min the thickness decreased. The values of mass per unit area and the corresponding thicknesses are shown in Figure 8 and Table 4.

Table 4 Thickness and mass values of the deposited films with different scan speeds.

Scan speed (mm/min)	Thickness (μm)	Mass (mg/cm^2)
0.4	2.53	0.3
0.8	1.54	0.17
1.2	0.85	0.101

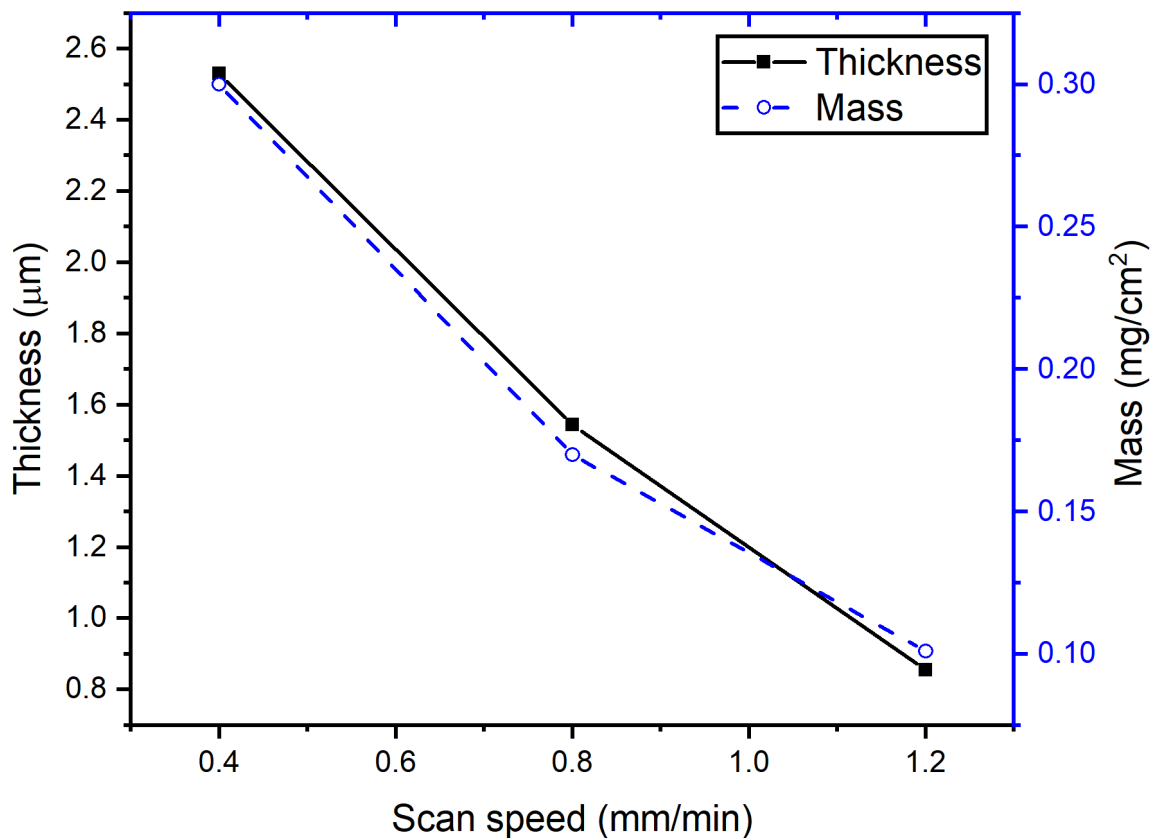


Figure 8 Mass per unit area versus the thickness of the deposited films with scan speeds 0.4, 0.8 and 1.2 mm/min.

The surface morphology of the original graphite powder and the deposited thin film, on a stainless-steel substrate, was observed with an FE-SEM. Figure 9 (a) is the FE-SEM image of the original graphite powder, showing that the sizes of the original powder particles are around $10\ \mu\text{m}$ and the shapes are irregular.

Figure 9 (b-g) shows the surface morphology of the deposited films on stainless steel, by comparing Figure 9 (a) and (b, c) we can see that most of the graphite powder fragmented to small particles; some of these particles are still in microscale graphite form, but most of the other particles are converted to very small flakes. As seen in Figure 9 (d-g), as the scan speed increased, the relative proportion of the microscale graphite particles on the deposited films become smaller relative to the slow scan speed case (0.4 mm/min). For 1.2 mm/min scan speed of deposition, the sizes of most of the fragmented particles ranged from about 100 nm to 180 nm, however, there were some fragmented particles with much smaller size. In Figure 9 (c, e, and g), red arrows indicate some of the graphene nano-flakes. The thin layers of graphite were separated during the NPDS deposition due to their high impact velocity. The orientation of the particle may be random during deposition, and particles with different orientations collided with the substrate. Due to the high-velocity impact, interlayer sliding and interlayer separation occurred and very thin structures were deposited on the stainless-steel substrate. In addition, large particles broke into small pieces to make nano-sized, thin structures.

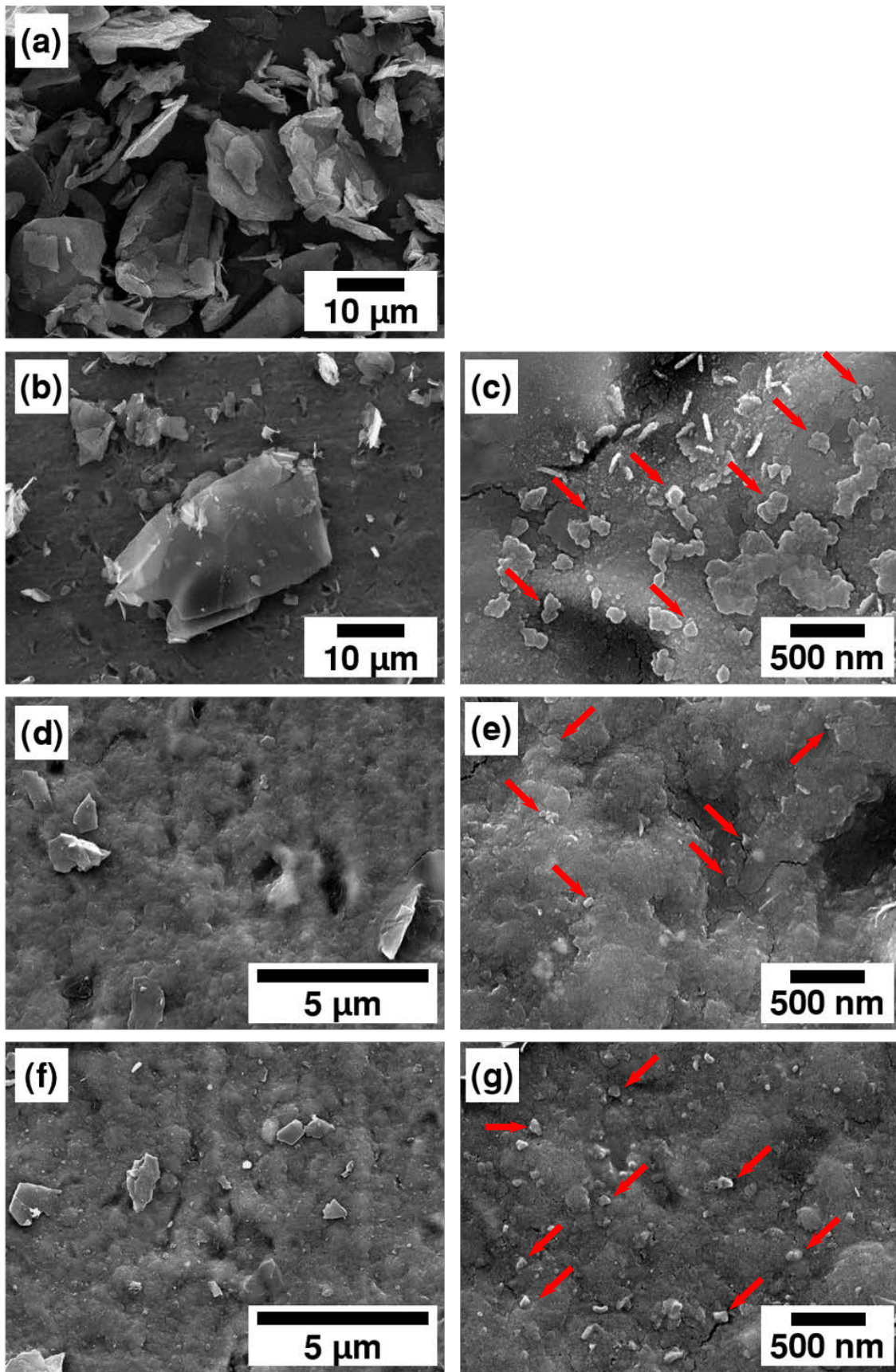


Figure 9 FESEM of (a) graphite powder, deposited film at scan speeds (b, c) 0.4 mm/min, (d, e) 0.8 mm/min and (f, g) 1.2 mm/min, respectively.

Figure 10 shows the TEM image of the deposited film with a scan speed of 1.2 mm/min. The high-resolution TEM image shown in Figure 10 (a) indicates the crystalline structure of randomly oriented graphene nano-flakes with some areas of amorphous structure. The Fast Fourier transformer (FFT) of the HR-TEM image in Figure 10 (b) shows a polycrystalline structure which has arisen from the short-range randomly oriented graphene flakes. The obtained histogram plot is shown in Figure 10 (c) at the surrounded position by the yellow rectangle in Figure 10 (a) indicates an in-plane lattice spacing of 0.26 nm corresponding to the graphene lattice spacing[48]. Other crystalline areas showed the same lattice spacing of 0.26 nm, as all positions were measured using the histogram plot. This suggests that all crystalline areas are graphene structured. In Figure 10 (d), the highly magnified image of the surrounded position by the yellow rectangle in Figure 10 (a) shows a triangular sublattice pattern of carbon atoms instead of a hexagonal pattern. This triangular pattern may come from few-layer graphene flake structures[131, 132]. The corresponding FFT clearly shows a hexagonal pattern of the graphene structure corresponding to the (100) plane.

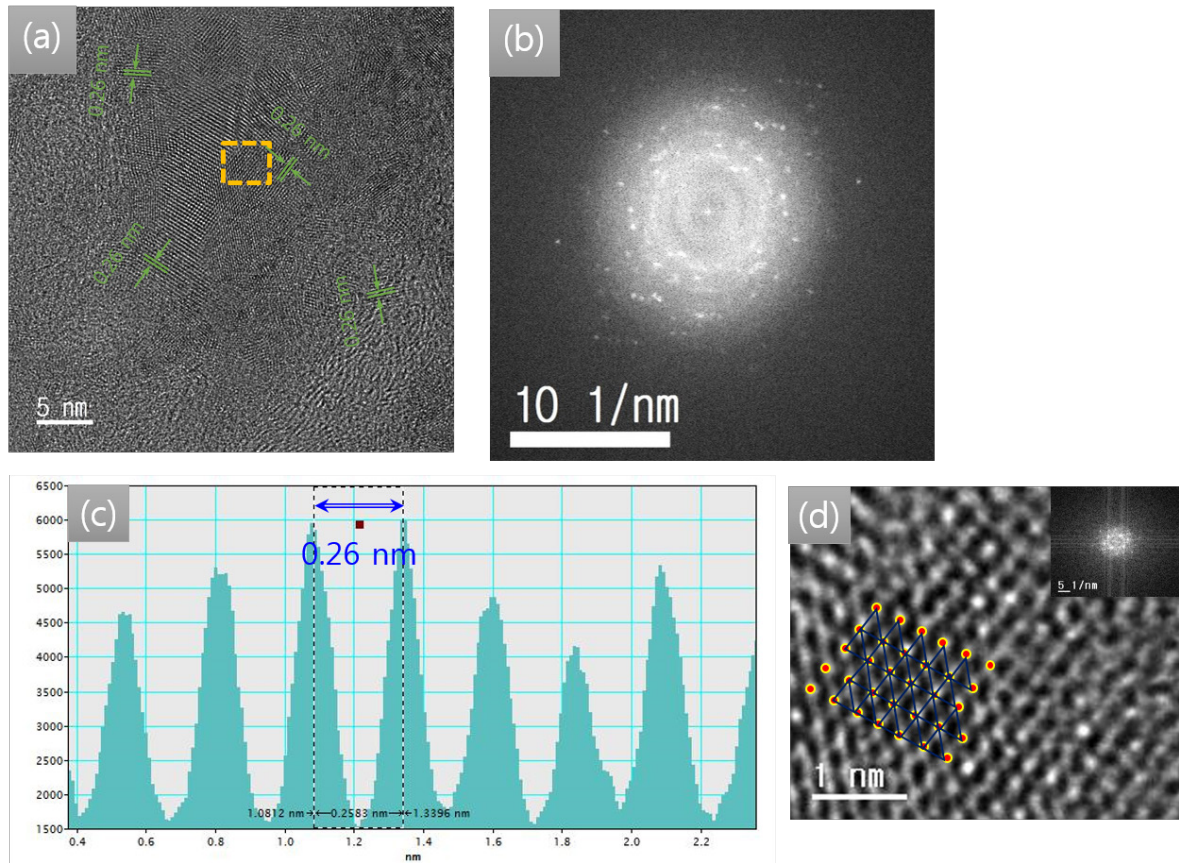


Figure 10 (a) HR-TEM image of the deposited film with scan speed 1.2 mm/min, (b) FFT of image (a), (c) Histogram plot of the area surrounded by the yellow rectangular in (a), and (d) magnified HR-TEM of the area surrounded by the yellow rectangular in (a) (In the top right, inset FFT of image (d)).

3.3.2 X-ray diffraction analysis

The structural properties of original graphite powder, and the deposited films with different scan speeds (0.4, 0.8, and 1.2 mm/min) and stainless-steel substrate were characterized using XRD analysis. Figure 11 shows the XRD spectrum of the original graphite powder, the sharp and high amplitude peak (002) at $2\theta=26.5^\circ$, which is the strongest peak obtained in the diffraction pattern in the direction perpendicular (c-axis) to the graphite hexagonal plates, indicates a highly organized layered structure with an interplanar spacing of 0.365 nm. The XRD spectrum of the deposited films shows peaks $\gamma(111)$, $\gamma(200)$, and $\alpha(211)$ at 43.6° , 50.5° , and 82° corresponding to the stainless steel substrate. In the of 0.4

mm/min case, there is (002) graphite peak at 26.3°. This peak disappeared when the scan speed was increased to 0.8 and 1.2 mm/min, which means that the graphene/graphite structure in case of 0.4 mm/min scan speed of deposition transformed to graphene structure as the scan speed increased. Also, the deposited films show a broad carbon (002) peak between 15 to 25°, the broadness of the (002) peak and the shift to a smaller angle indicates a decrease in the particle size due to defragmentation of graphite microparticles to graphene nano-flakes and an increase in the interplanar spacing.

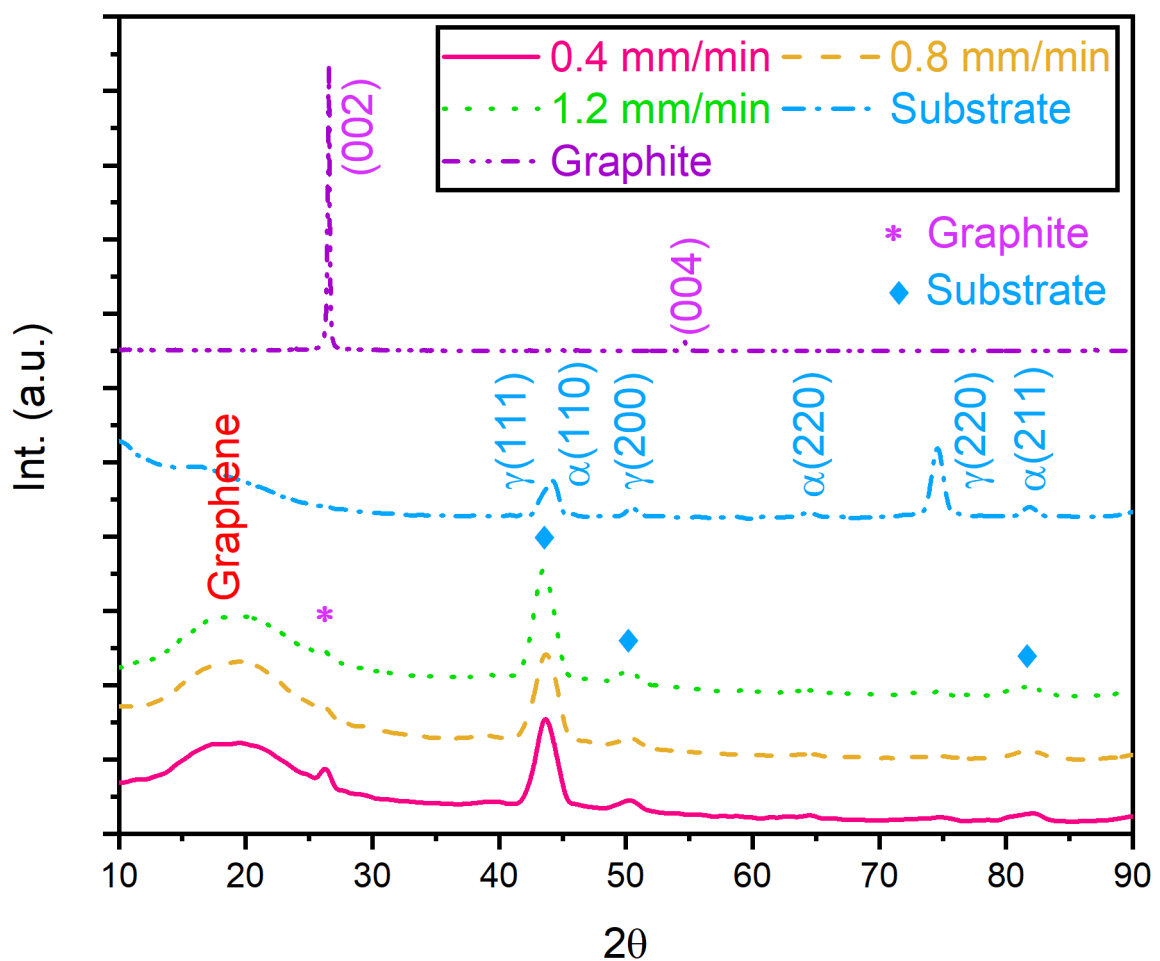


Figure 11 XRD of the graphite powder, SUS304 substrate, and deposited films at different scan speeds.

3.3.3 Raman Spectroscopy

The Raman spectroscopy results of the original graphite powder and deposited films is shown in Figure 12. It is obvious that the graphite powder has mainly three bands D, G, and 2D at 1352.4, 1582.1, and 2720.77 cm^{-1} , respectively. The G peak is due to the doubly degenerate zone center E_{2g} mode[133]. The G band has the most intense peak and the D band has negligible intensity. The negligible intensity of the D band suggests a crystalline structure with almost no disorder. The 2D band for graphite is consists of two bands $2D_1$ and $2D_2$, as shown in the enlarged view of the 2D peak, the double band structure of the 2D peak was explained by other researchers[55–60]. For all the deposited films under all scan speeds (0.4, 0.8 and 1.2 mm/min), the deposited film on stainless steel substrate showed two different behaviors. During measurement, the laser beam was focused in two different positions for a more accurate measurement. When the laser beam was focused on a large sized, fewer fragmented particles were produced, as shown in Figure 12 (a). In this case, the D peak was located at 1352.4 cm^{-1} for all deposited films, the G peak positions, for the slower to faster scan speeds, were at 1586, 1592 and 1596 cm^{-1} . We can observe that the ratio of I_D/I_G , as shown in Table 5, becomes higher when the scan speed of deposition increases, which confirms that the amount of graphite structure on the deposited films decreases as the scan speed of the deposition is increases. 2D peaks appear around 2718, 2708 and 2699 cm^{-1} , respectively for the different scan speeds of deposition. The shift of the G band to a higher energy compared to the graphite powder, the sharpness of 2D peak, and the shift in the 2D band to a lower energy, all indicate that while increasing the scan speed of deposition, more of micro-sized graphite particles gradually transform from graphite to a few-layer graphene structure.

When the laser beam was focused on the fragmented particles, the Raman spectrum of the deposited thin films under all scan speeds (0.4, 0.8 and 1.2

mm/min) has a different interesting behavior; as seen in Figure 12 (b), the intensity of D band peaks at 1352.4, 1352.4 and 1350.8 cm^{-1} respectively, which represents the disorder was higher than the G band appears around 1598.5, 1597 and 1595 cm^{-1} , respectively for the different scan speeds of deposition, which means that the I_D/I_G for the deposited film is much higher than that of the graphite powder. This increase in I_D/I_G can be described because of the fragmentation of the micro-sized graphite particles to graphene nano-flakes which increase the edge defects and disorder of the graphene. The G band is shifted to a higher energy compared to the graphite powder, as shown in Figure 12 (b). The G band has a shoulder at 1654 cm^{-1} (D' band). Also, the 2D band, which appears around 2698 cm^{-1} , for all deposited films, is shifted to lower energy compared to the graphite powder. The 2D band of the deposited film is sharper than that of the original powder. Moreover, the shift in the 2D band indicates that the thickness of the deposited film is decreases after deposition of the original graphite powder on stainless steel using the NPDS. Based on the shifts in the G and 2D peaks, we concluded that the layers of micron-sized graphite powder were separated due to the high impact velocity during deposition, and that few-layer graphene structures have formed on the stainless steel[134-140]. Furthermore, the strong and sharp D band peak and D' band peak suggest a nanocrystalline structure, as well as the presence of graphene edges and defects[141, 142]. These graphene edges may appear due to fragmented graphene flake structures. Furthermore, defects may have occurred during the high impact velocity deposition, or by interactions between the stainless steel and graphene, which may have produced vacancies, dislocation, and/or dangling bonds[143]. The positions of the D, G, and 2D peaks for the graphite powder and deposited films are shown in Table 5.

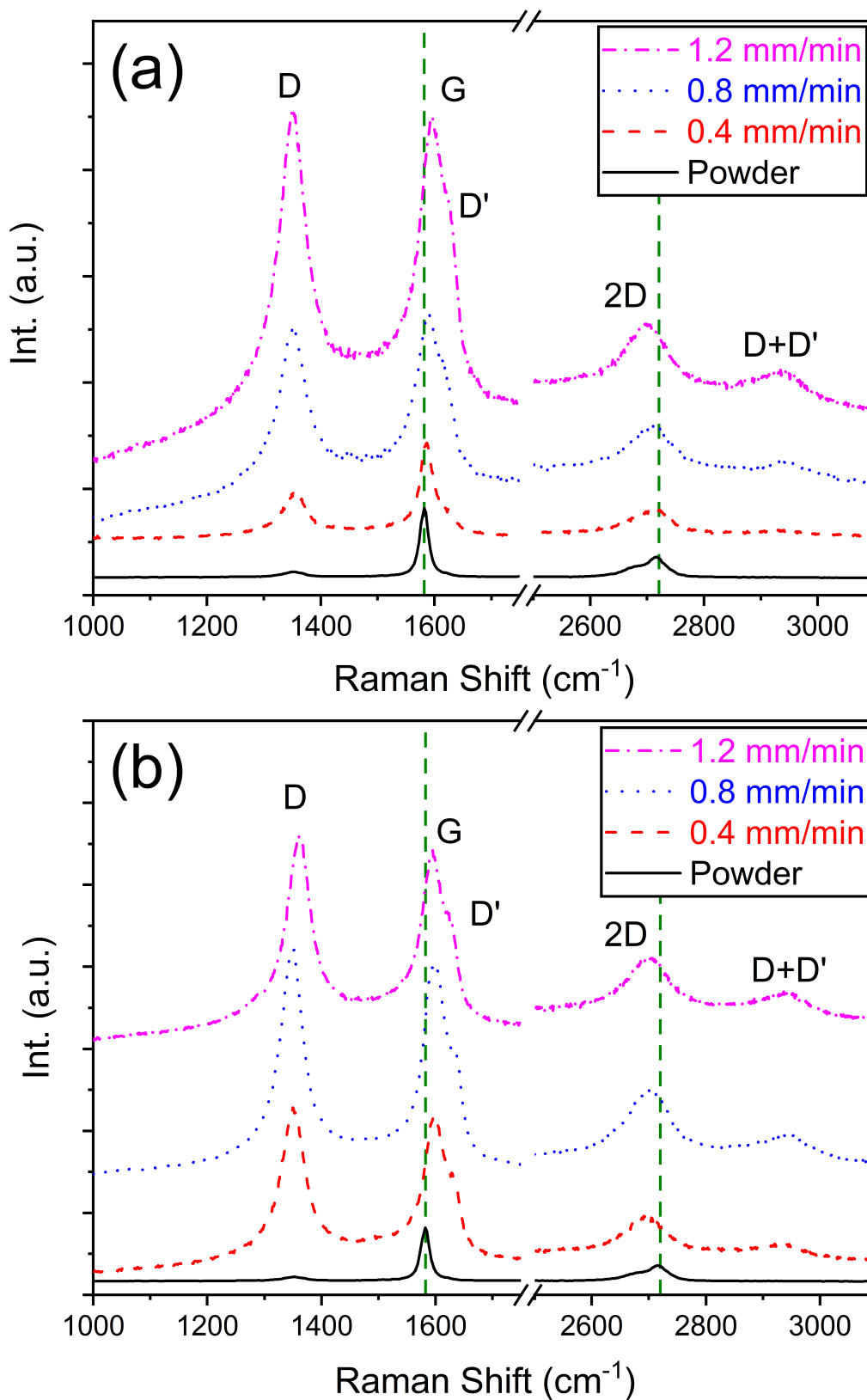


Figure 12 Raman spectroscopy of (a) the graphite powder and deposited films at different scan speeds on larger size particles with less fragmentation, (b) graphite powder and deposited films at different scan speeds on the more fragmented particles.

Table 5 D, G, and 2D peaks and I_D/I_G for the graphite powder and deposited films.

Film	large size & less fragmented particles.				fragmented particles			
	D peak (cm ⁻¹)	G peak (cm ⁻¹)	2D peak (cm ⁻¹)	I _D /I _G	D peak (cm ⁻¹)	G peak (cm ⁻¹)	2D peak (cm ⁻¹)	I _D /I _G
Powder	1352.4	1582.1	2720.8	0.269	1352.4	1582.1	2720.8	0.269
0.4 mm/min	1352.4	1586	2718	0.647	1352.4	1598.5	2698	1.054
0.8 mm/min	1352.4	1592	2708	0.970	1352.4	1597	2698	1.064
1.2 mm/min	1352.4	1596	2699	1.009	1350.8	1595	2698	1.069

3.3.4 Electrochemical properties

The electrochemical performance of graphene supercapacitors, fabricated from the deposited films (0.4, 0.8 and 1.2 mm/min scan speeds), with the addition of 0.03 mol of H₃PO₄-PVA gel electrolyte, were investigated as part of a 2-electrode system. Figure 13 (a-c) shows the cyclic voltammetry curves measured at the scan rates 2 to 100 mV/s and potential window 0 to 1 V. The areal capacitance calculated from the CV curves using the formula

$$C_a = \frac{\int I dV}{s A \Delta V} \dots \dots \dots 3.1$$

where *I* is the response current, *s* is the scan rate, ΔV is the potential window and *A* is the area of graphene electrode in contact with the electrolyte. The CV curves of graphene supercapacitor are symmetrical and have a near-rectangular shape over the 1 V potential window, which is typical of an ideal capacitor. The value of areal capacitance was increased from 0.68 mF/cm² at 2 mV/s for 0.4 mm/min scan speed to 1.28 mF/cm² at 2 mV/s for 1.2 mm/min scan speed, as shown in Figure 13 (d), two factors explain this improvement of the capacitance: In case of a fast scan speed, after the graphite particles were accelerated to supersonic speeds through the converging-diverging nozzle, the graphite particles impact with the stainless steel substrate, which has relatively high hardness, so a thin

layer of graphene will be formed on the substrate, the deposition quickly will cover another location until it covers the required area of substrate. On the other hand, for the slow scan speed, after the acceleration of graphite powder, the impact takes place at first between the powder and stainless-steel substrate. As in the case of a fast scan speed, a thin graphene layer will form over the substrate, but due to the slow scan speed the impact will happen between the graphite powder and the deposited film, which has a lower hardness than the stainless steel. Therefore, the amount of fragmentation of graphite powders becomes lower than that which occurs with a fast deposition scan speed. This is clear from the (002) graphite peak intensity found in the XRD analysis, which decreased as the scan speed increased. Also, this is clear from the Raman spectroscopy, as previously mentioned. In summary, a slow scan speed shows graphene/graphite structure which has a smaller surface area and lower conductivity than graphene structure in the fast scan speed. As such, the improvement of the capacitance can be explained as a result of two reasons. The first reason is that the graphite structure of the deposited film forms more readily with a slow scan speed deposition, such that the specific surface area becomes higher than in the case of a fast scan speed deposition and allow more charge transfer on the surface of the electrode[144]. The second reason is that the number of graphene layers is decreases with an increase in the scan speed, since the value of I_D/I_G for a fast scan speed is larger than that of low scan speed and the decreased number of graphene layers can improve the charge transfer inside the electrode material[145, 146].

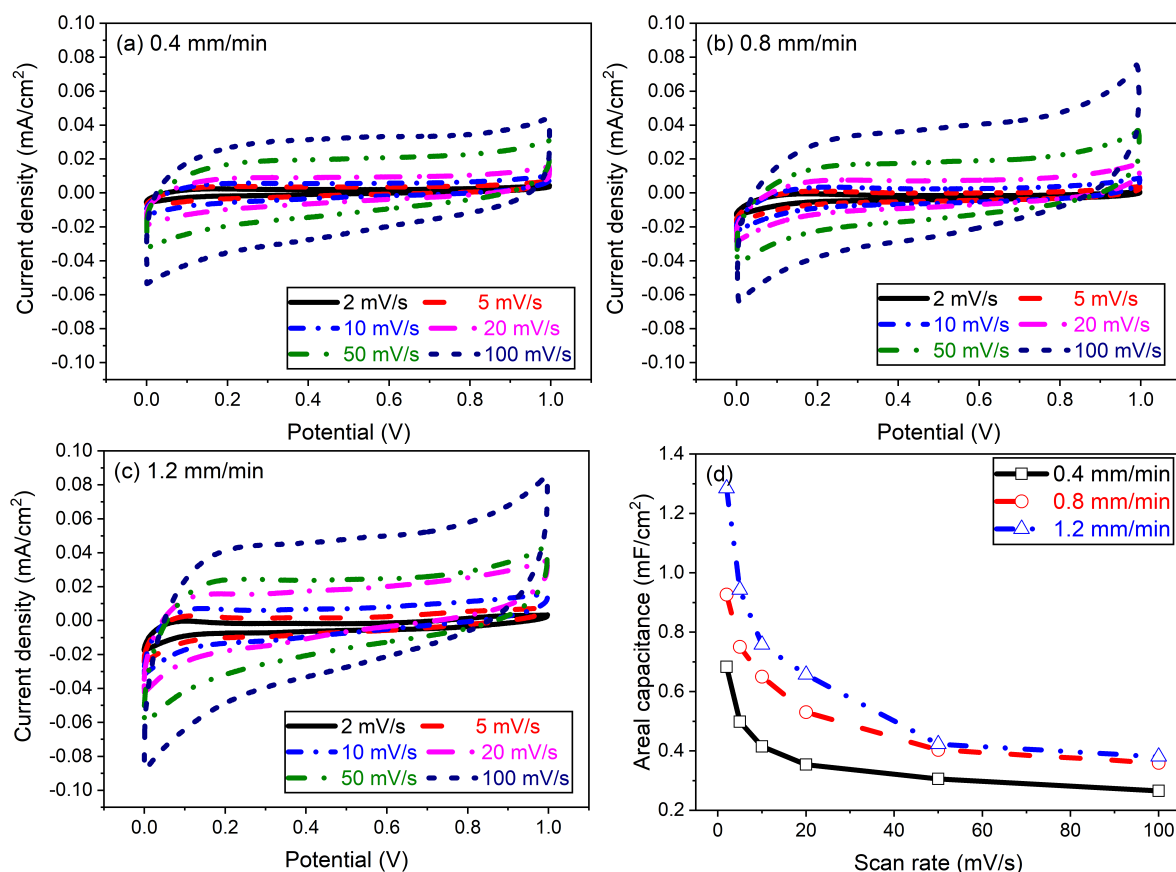
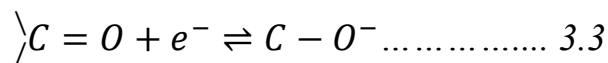
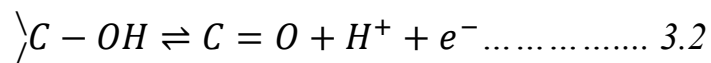


Figure 13 (a-c) CV curves of 0.03 mol of H_3PO_4 gel electrolyte with different scan speeds, (d) calculated specific areal capacitance from CV curves.

In Figure 14, the cyclic voltammetry was measured again for the deposited films using 0.06 and 0.09 mol H_3PO_4 -PVA gel electrolytes. Both electrolytes have quasi-rectangular CV curves and the areal capacitance was 1.28 mF/cm² at 2 mV/s for the case of a 1.2 mm/min scan speed with 0.03 mol of H_3PO_4 -PVA gel electrolyte. This value became 1.47 mF/cm² at 2 mV/s when the concentration of H_3PO_4 was increased to 0.06 mol and increased to 1.67 mF/cm² at 2 mV/s for the case of 0.09 mol of H_3PO_4 . It appears that the areal capacitance increases gradually while increasing the concentration in the range of 0.03-0.09 mol. These results confirm the assumption that the high ion concentration cloud improves the areal capacitance value, which also agrees with previous research[147, 148]. The capacitance of graphene electrode is mainly due to the diffusion of ions from the electrolyte to the surface of the electrode, and the rate of the whole electrode

reaction will be enhanced if the diffusion resistance is decreased. In this sense, a high concentration of H₃PO₄-PVA gel electrolyte with a high ionic conductivity will provide a low diffusion resistance. The diffusion resistance (R_{ct}: charge transfer resistance) can be seen in the Nyquist plot. Previous studies have also found that there is a relationship between the specific capacitance of the activated carbons and the electrolyte conductivity, i.e., the specific capacitance increased with increasing electrolyte conductivity[149]. For 0.06 mol of H₃PO₄, the oxidation and reduction peak at ~0.4 and 0.25 V in Figure 9(a) are corresponding to the pseudocapacitance after phosphorus-doping in graphene layers[150-152]. The doping of phosphorus may be happened during the electrochemical measurement due to the porous structure of the carbon atoms. The existence of phosphorus atoms introduces a positive charge on the neighboring carbon atoms and creates centers for oxygen reduction reaction[151]. Also, in case of 0.09 mol of H₃PO₄, there is a small oxidation and reduction humps at the same potentials due to the same reason. The samples with relatively low concentration of H₃PO₄ (0.03 mol) did not showed the oxidation and reduction peak in CV curves. Therefore, relatively high concentration of H₃PO₄ may easily create the doping of phosphorus during the electrochemical measurement. The reactions related to pseudocapacitance can be considered as follows[153, 154]:



The redox reaction attributed to the reversible quinone/hydroquinone pair.

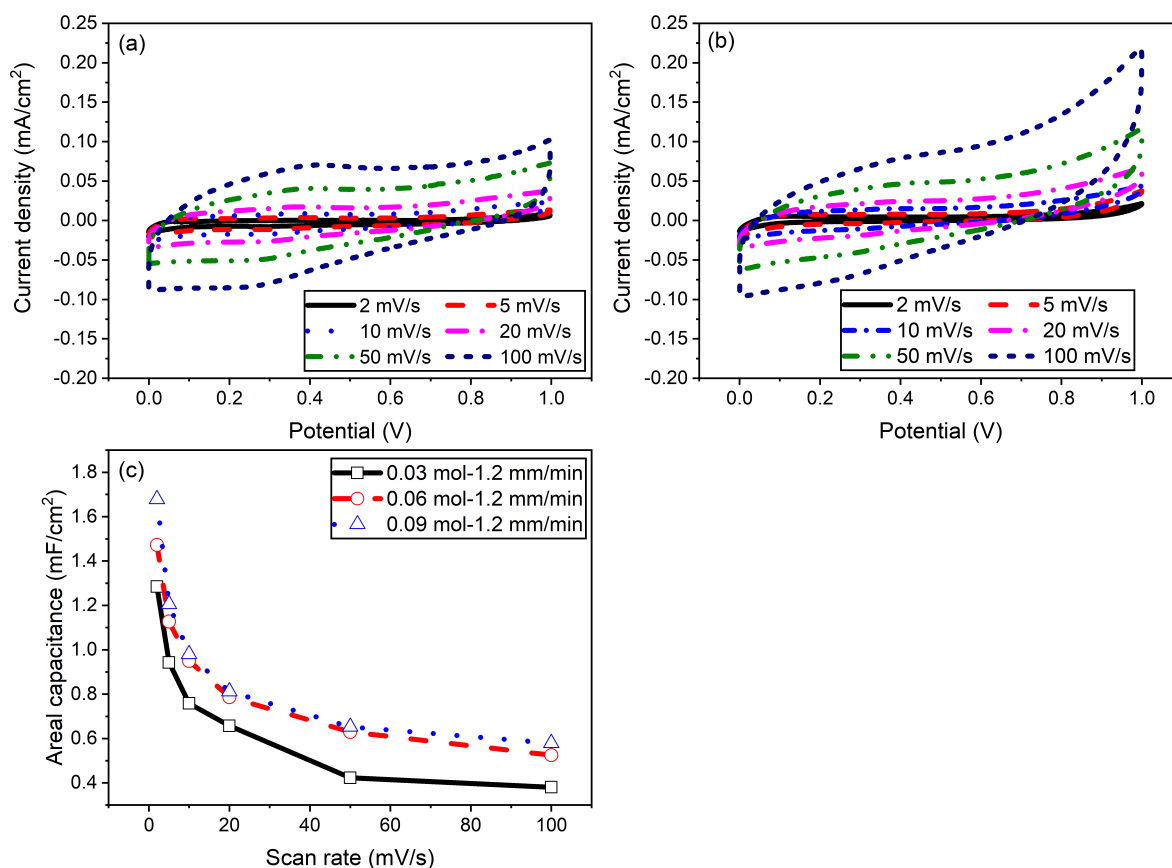


Figure 14 CV curves of (a) 0.06, (b) 0.09 mol of H_3PO_4 gel electrolyte with a 1.2 mm/min scan speed electrode, and (c) the calculated areal capacitance for 0.06 and 0.09 mol of H_3PO_4 gel electrolyte with a 1.2 mm/min scan speed electrode.

The galvanostatic charge-discharge curves for the supercapacitors assembled from the deposited films, with different scan speeds (0.4, 0.8 and 1.2 mm/min), in Figure 15 (a-c), and 0.03, 0.06 and 0.09 mol of H_3PO_4 -PVA gel electrolyte, in Figure 16, were investigated at current densities 0.01 to 0.1 mA. The areal capacitance was calculated from the CV curves using the formula

$$C_a = \frac{I}{dV/dt} \dots\dots\dots 3.4$$

where I is the current density and dV/dt is the slope of discharge curve after the iR drop. Figure 15 (a-c) shows the galvanostatic charge-discharge curves for all of the supercapacitors, linear charge and discharge curves with a neglectable iR

drop, indicating that the electrodes have a lower internal resistance, which leads to better EDL performance. The areal capacitance calculated from discharge curves is shown in Figure 15 (d). The results are in agreement with cyclic voltammetry, where the areal capacitance is increased by controlling the thickness of the deposited films by the scan speed of the deposition, for 0.03 mol of H_3PO_4 -PVA gel electrolyte the areal capacitance was 0.39 mF/cm^2 for the case of a 0.4 mm/min scan speed. This value increased to 1.07 mF/cm^2 when the thickness of the deposited film decreased by increasing the scan speed to 1.2 mm/min . Also increasing the concentration of H_3PO_4 in the gel electrolyte from 0.03 to 0.09 mol improves the areal capacitance, which increased to 1.2 mF/cm^2 for the case of a 1.2 mm/min scan speed with 0.09 mol of H_3PO_4 -PVA gel electrolyte. All areal capacitances are calculated from galvanostatic charge-discharge at 0.01 mA of current.

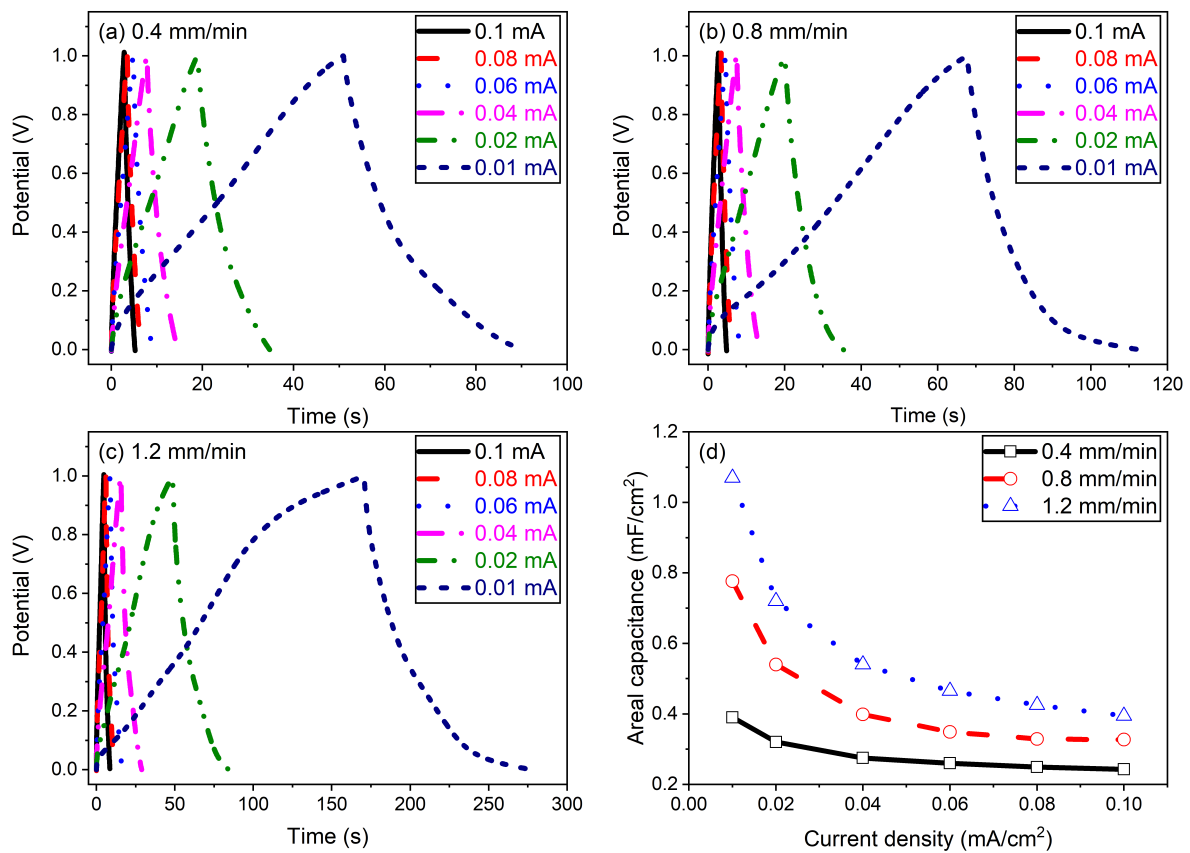


Figure 15 (a-c) Galvanostatic charge/ discharge curves of 0.03 mol of H_3PO_4 gel electrolyte with different scan speeds, (d) Calculated specific areal capacitance from charge/ discharge curves.

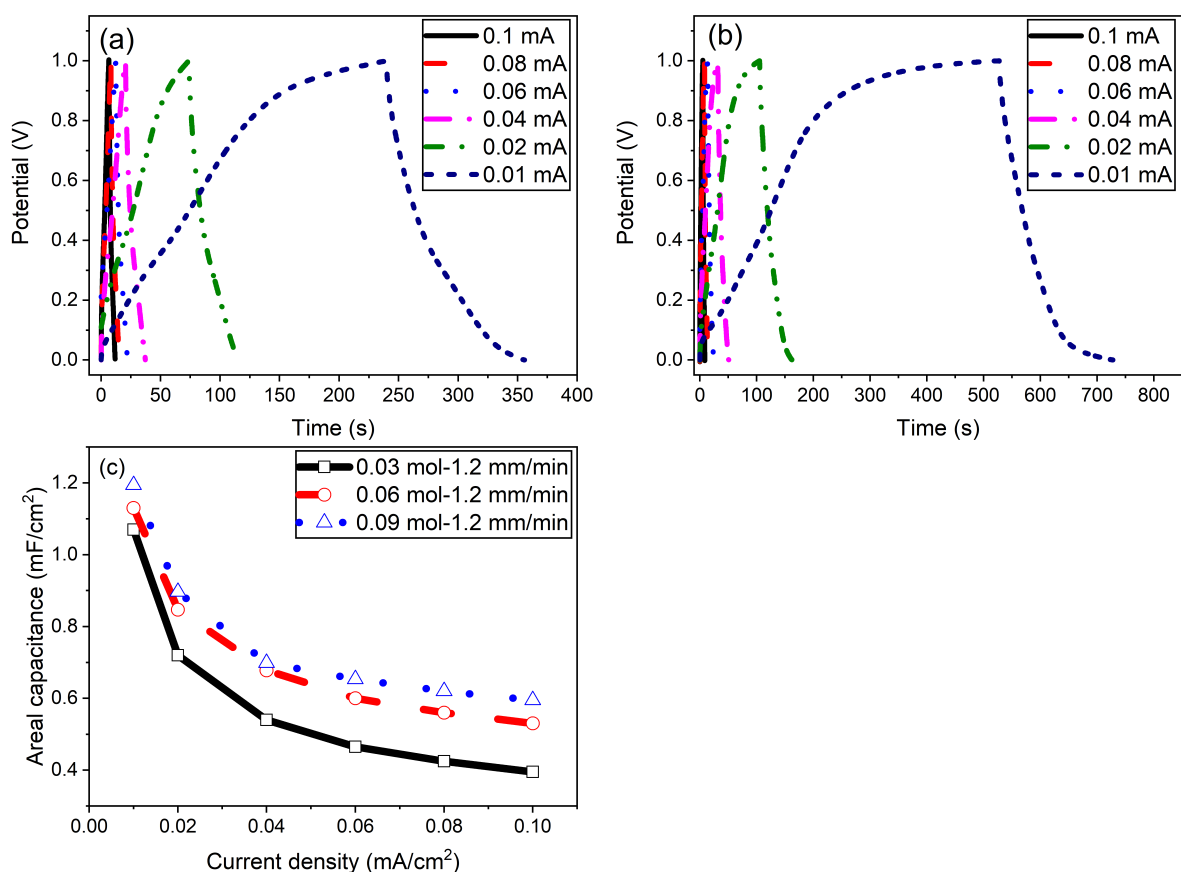


Figure 16 galvanostatic charge/ discharge curves of (a) 0.06, (b) 0.09 mol of H_3PO_4 gel electrolyte with a 1.2 mm/min scan speed electrode, and (c) the calculated areal capacitance for 0.06 and 0.09 mol of H_3PO_4 gel electrolyte with a 1.2 mm/min scan speed electrode.

Other researchers previously have reported areal capacitances of 3.7 and 2.13 mF/cm² by CVD[129] and CVD with chemical treatment[155]. The supercapacitor prepared by NPDS shows an areal capacitance 1.67 mF/cm²; even though the value is smaller than those found by other researchers, but the fabrication process is much easier, cheaper, and it can be easily applied in industry because it allows a large area deposition in a small amount of time. The supercapacitor prepared by NPDS is superior to those produced by many other techniques such as LBL (394 μ F/cm²)[156], electrochemical reduction of GO (487 μ F/cm²)[157], vertically oriented graphene (0.087 mF/cm²)[158], graphene–

CNT carpets (0.23 mF/cm^2)[159], and graphene–PEDOT: PSS hybrid films (0.179 mF/cm^2)[160].

Electrochemical impedance spectroscopy (EIS) measurements were carried out to understand the electrochemical details in the frequency range from 1 Hz to 1 MHz with an open-circuit voltage and an AC amplitude of 10 mV.

As shown in Figure 17 (a), the fabricated supercapacitors from the three electrodes deposited with different scan speed (0.4, 0.8 and 1.2 mm/min) and 0.03 mol H_3PO_4 -PVA all exhibited typical AC impedance characteristics of supercapacitors[53]. In the high-frequency region (Figure 17 (a) enlarge view), the intercept with a real impedance (Z') represents an equivalent series resistance (R_s), which includes the resistance of electrode materials, ionic resistance of electrolyte, and contact resistance between the electrode and current collector; the radius of semicircle is indicative of the electrode conductivity and the charge-transfer resistance (R_{ct}) of electrode materials. R_s is estimated to be around 1.1Ω for a 0.4 mm/min scan speed electrode, which was larger than that given by a 0.8 mm/min electrode scan speed (0.97Ω) and 1.2 mm/min scan speed electrode (0.85Ω). The semicircle diameter represents the value of R_{ct} obtained for the three electrodes and has a small diameter. This may be due to the formation of graphene-graphite structures on the surface of the 0.4 mm/min scan speed electrode; the amount of this formation may have decreased when the scan speed is increased to 0.8 and 1.2 mm/min, thus improving the impedance of the electrodes. In the intermediate frequency region, the slope of the 45° portion of the curves is the Warburg resistance, which represents the ion diffusion/transport in the electrolyte. In the low-frequency region, the capacitive behavior of the 1.2 mm/min scan speed electrode is evident in the curve. The curve is slightly bent but overall exhibits a good capacitive performance.

Nyquist plots of the three typical 1.2 mm/min scan speed electrodes with 0.03, 0.06 and 0.09 mol H_3PO_4 -PVA electrolytes were measured, as shown in

Figure 17 (b). R_s values were 0.85, 0.62, and 0.42 Ω respectively, the supercapacitor fabricated with 0.09 mol H_3PO_4 -PVA electrolyte exhibits a lower internal resistance and a smaller semicircular diameter at high frequencies, indicating a better interface between the electrolyte and electrode. The conductivity is dependent on the concentration of the H_3PO_4 in the gel electrolyte; as the H_3PO_4 concentration increases, the conductivity also increases, meaning the value of R_s decreases as the concentration increases. As a result of increasing the conductivity, mobility of the H_3PO_4 is increased; this can consequently decrease the value of R_{ct} , which is represented by the radius of semicircle. This result agrees with previous reports[129, 161].

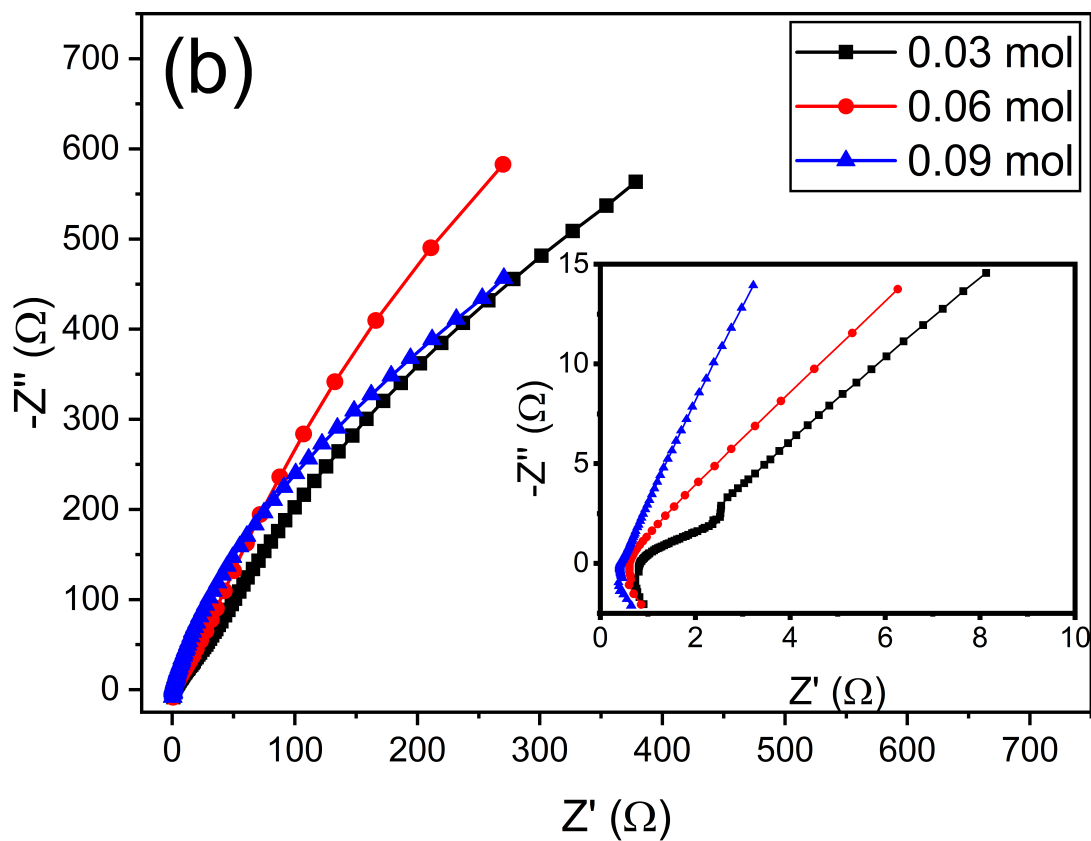
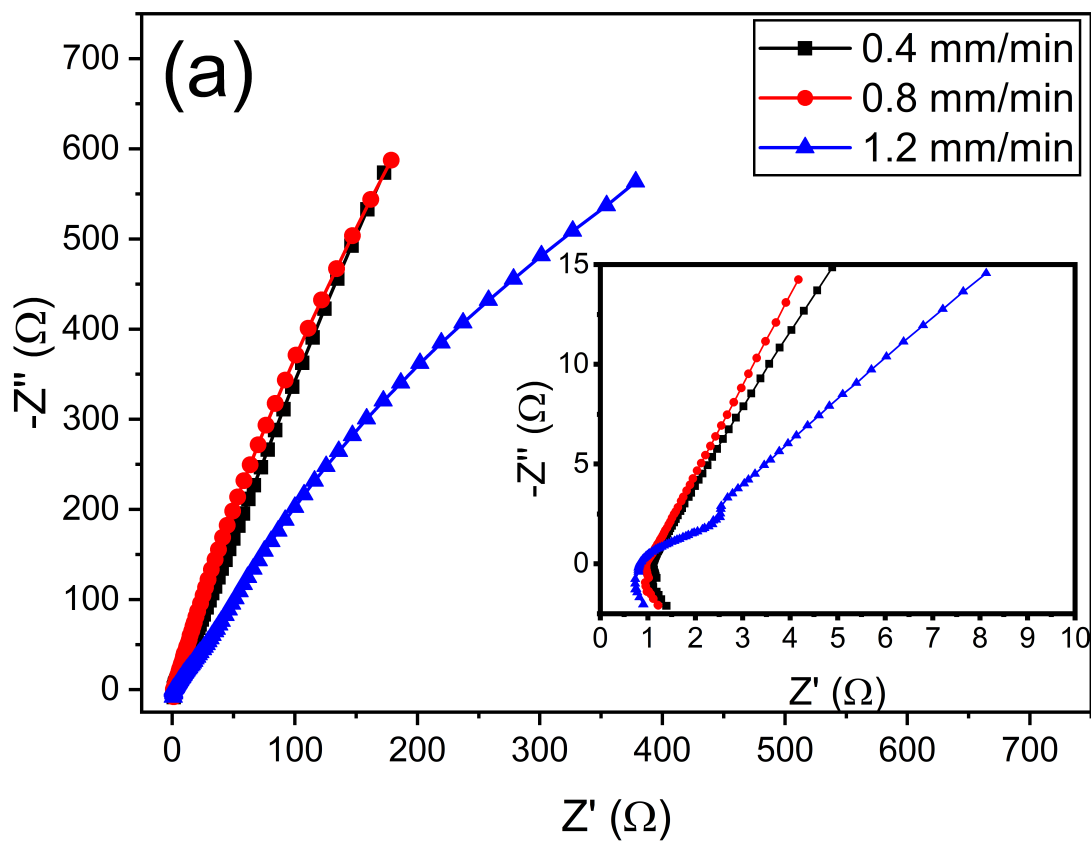


Figure 17 Nyquist plots of (a) 0.03 mol of H_3PO_4 gel electrolyte with different scan speeds, (b) 0.03, 0.06 and 0.09 mol of H_3PO_4 gel electrolyte with a 1.2 mm/min scan speed electrode.

The cyclic stability of the deposited film with a 1.2 mm/min scan speed and 0.09 mol of H₃PO₄-PVA was investigated at current 0.06 mA, repeating the galvanostatic charge/discharge measurement ranging from 0 to 1 V. As shown in Figure 18, the supercapacitor has a coulombic efficiency of 98% at the beginning, which decreased to 95% after 5000 cycles. The good cycling performance of the electrode material indicated a good stability and strong adherence to the stainless-steel substrate. The good cycling stability can be attributed to two reasons. The first reason is that the few-layer graphene nanoflake structure is randomly oriented on the substrate, which allows the electrolyte ions to diffuse through the graphene layers, leading to a good improvement in the electrochemical performance of the supercapacitor. The second reason is the mechanical stability caused by the strong adherence of the few-layer graphene nanoflake structures on the stainless-steel substrate. The degradation in the coulombic efficiency after 5000 cycles is likely due to the consumption of the electrolyte as a result of irreversible reactions between the graphene electrode and the H₃PO₄-PVA gel electrolyte.

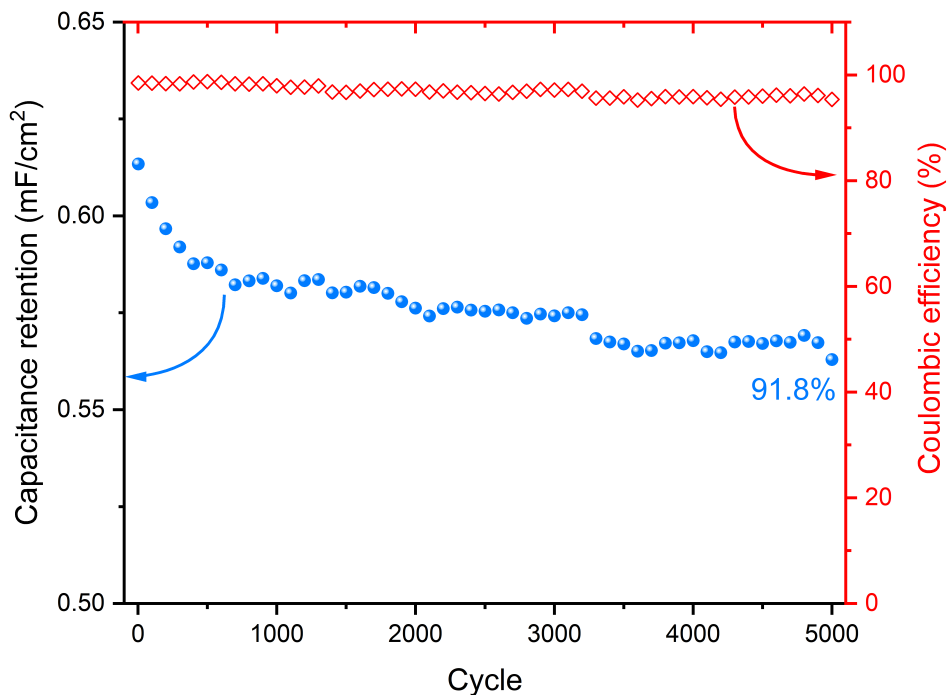


Figure 18 Charge /discharge stability over 5000 cycles for a 1.2 mm/min scan speed and 0.09 mol of H₃PO₄- PVA at a current of 0.06 mA.

3.4 Summary

In this research, a vacuum kinetic spray was used to deposit micro-sized graphite powder on stainless steel substrate at room temperature and low-pressure conditions. The NPDS results in the formation of randomly oriented few-layer graphene nano-flakes; as confirmed by FE-SEM, HR-TEM, XRD, and Raman spectroscopy. Some of the graphite particles fragmented to graphene nano-flakes and some particles did not fragment and were converted to graphite particles with a smaller size than the particles in the original graphite powder. The amount of graphite structure on the deposited films decreases with an increase in the deposition scan speed.

The electrochemical capacitive behavior of the supercapacitors assembled from the deposited films using NPDS, with 0.03 mol PVA-H₃PO₄, showed an areal capacitance comparable to other research, and it was improved by increasing scan speed of the deposition. Also, increasing the amount of H₃PO₄ in the PVA gel electrolyte can improve the areal capacitance. The very affordably fabricated supercapacitor with 0.09 mol H₃PO₄-PVA gel electrolyte, produced with a 1.2 mm/min deposition scan speed, showed a good stability over 5000 cycles.

Chapter 4

Symmetric Supercapacitor

Based on MoS₂-Graphite

Composite

4.1 Background

Recently, the claim for energy storage devices has become a significant problem and attracted worldwide attention. Supercapacitors or electrochemical capacitors are considered as promising electrochemical storage devices on account of their high energy density, fast charging/discharging rate, long cyclic stability and easy layout[5, 6, 8]. Generally, supercapacitors can be sorted into two types according to their charging techniques. The first type is comprised of electric double-layer capacitors (EDLCs), in such kind of capacitors, the storage mechanism is based on the interface layer formed between the liquid/solid (electrolyte/electrode) surface. High conductivity and large surface area carbon materials, such as activated carbon, graphene, carbon nanotubes, and reduced graphene oxide are used as the electrode materials for EDLCs[97, 162-169]. The second type is comprised of pseudocapacitors, wherein the storage mechanism is via fast and reversible faradaic reactions on the electrode materials. Typical pseudocapacitive materials include transition metal oxides/hydroxides, metal chalcogenides, and conducting polymers and their composites. They hold a much higher energy density but have unsatisfactory cycle stability and rate capability. Thus, their power density is generally low[96, 170-172].

Molybdenum disulfide (MoS_2) is belonging to the family of transition-metal dichalcogenides (TMDs) and has been shown to be a promising electrode material for supercapacitors due to its high theoretical specific capacitance and layered structure. The origin of the large specific surface area is the structure of MoS_2 , which is composed of a Mo layer sandwiched between two sulfur layers by a covalent bond. The adjacent two layers are stacked together with a weak van der Waal interaction, which is like the graphite structure. MoS_2 layers can be exfoliated to a single layer or a few layers by different chemical or physical approaches[173-175].

Recently, the researchers have focused on MoS₂ as a supercapacitor mainly because it has a theoretical capacity that is larger than that of graphite[176] and a faster ionic conductivity than oxides[177]. As well as its electric double-layer capacitance, MoS₂ provides a pseudocapacitance at low scan rates because of the electrolyte ions transfer into the layers of MoS₂, which improves its charging behavior. But because of the 2H phase of MoS₂ (stacking sequences of trigonal prismatic) which has a band gap of 2 eV for monolayer, which makes MoS₂ a poor conductor. To increase the electrical conductivity of MoS₂, composite electrodes consists of graphene/MoS₂[178] and polyaniline/MoS₂[176] have been studied. However, the electrochemical performance of MoS₂/graphene hybrid electrodes is quite different from those of graphene[176, 179] and MXene electrodes[173]. Only a few previous reports on MoS₂ composite supercapacitors address intricate synthesis approaches using toxic-reducing agents and high temperatures[180-182]. The present study focused on developing a facile low-temperature method to prepare high-performance MoS₂ composites.

The promising and facile strategy of the vacuum kinetic spray method at room temperature and low-pressure conditions was used to deposit the MoS₂-graphite composite from MoS₂-graphite powder mechanically mixed by ball milling. One of the vacuum kinetic spray methods is known as the nanoparticle deposition system (NPDS). NPDS presents a facile, low cost and environmentally friendly deposition method which can deposit both metals and ceramics, such as tin, nickel, Al₂O₃, TiO₂, and WO₃ at a low temperature without any binding chemicals. Additionally, few-layer graphene nanoflakes have been successfully deposited using this vacuum kinetic spray for supercapacitor applications[80, 91, 92, 183-185]. Also, vacuum cold spray method was used to deposit composites such as hydroxyapatite/graphene-nanosheet for the biomedical application[186] and polyimide-copper coating for antifouling applications[187].

In this study, MoS₂ and graphite micro-sized powders were mechanically mixed by ball milling with different compositions (5, 10, 15, 20, 25 and 30% wt. of MoS₂). The NPDS was used to deposit the composite powder. The electrochemical performances of the all-solid-state supercapacitors were evaluated in a two-electrode system by using cyclic voltammetry (CV), galvanostatic charge/discharge (GCD), and electrochemical impedance spectroscopy (EIS) to determine the best composition ratio. The surface morphology for the bulk and composite powders and deposited films were analyzed by a field emission electron microscope (FE-SEM), X-ray diffraction (XRD), and Raman spectroscopy.

4.2 Experiment

4.2.1 MoS₂-graphite powder mixing

Ball milling (GLBM-G, Global Lab Co., Ltd., Korea) was used to mix different compositions of MoS₂ and graphite powders with compositions 5, 10, 15, 20, 25 and 30% wt. of MoS₂ for 20 h. Stainless steel balls with a 5 mm diameter were used in this process. The ball-to-mass ratio was 20:1 and the rotation speed was 600 rpm.

4.2.2 MoS₂-graphite composite deposition

The NPDS consisted of an air compressor, powder feeder, nozzle, vacuum chamber, vacuum pump, and controller, as in Figure 6. The air compressor supplies compressed air to carry MoS₂-graphite powder from the powder feeder to the nozzle. In this research, a slit converging-diverging nozzle with dimensions of 50 × 0.2 mm² was used to accelerate the powder for a large-area deposition. The process parameters are shown in Table 6.

Table 6 Process parameters for MoS₂-graphite composite deposition on a stainless-steel substrate

Parameter	Value
Compressor pressure (MPa)	0.3
SoD (mm)	5
Piston speed (mm min⁻¹)	17
Brush speed (rpm)	7000
Scan speed (μm s⁻¹)	100
Chamber pressure (MPa)	0.0427
Deposition shape	2x5 cm ²
Substrate material	AISI 304

4.3 Results and Discussion

4.3.1 Surface Morphology

The surface morphologies of the bulk MoS₂, the bulk graphite, the mechanically mixed MoS₂-graphite, and the deposited 15% MoS₂-graphite composite on a stainless-steel substrate were observed by FE-SEM. Figure 19 (a, b) clearly show that the bulk MoS₂ powder has irregular flakes with a lateral size less than 2 μm, and the lateral size of the bulk graphite powder is larger than 10 μm with an irregular shape. After mixing by ball milling, as shown in Figure 19 (c), the MoS₂ flakes were well attached to the graphite flakes. The lateral sizes of the MoS₂ and graphite were the same as those of the bulk powders. After deposition, as shown in Figure 19 (d-f), the graphite fragmented to smaller flakes of less than several micrometers in size. A small amount of the graphite particles was less than 100 nm. In addition, the MoS₂ particles were fragmented to smaller particles of less than 1 μm in size, and some particles were less than 200 nm in size. The deposited MoS₂-graphite composite exhibited smaller size particles than the mechanically mixed 15% MoS₂-graphite powder. The orientation of the

particle appears random during deposition owing to the high impact velocity between the powder and the substrate. The composite particles are fragmented to smaller flakes and are randomly oriented.

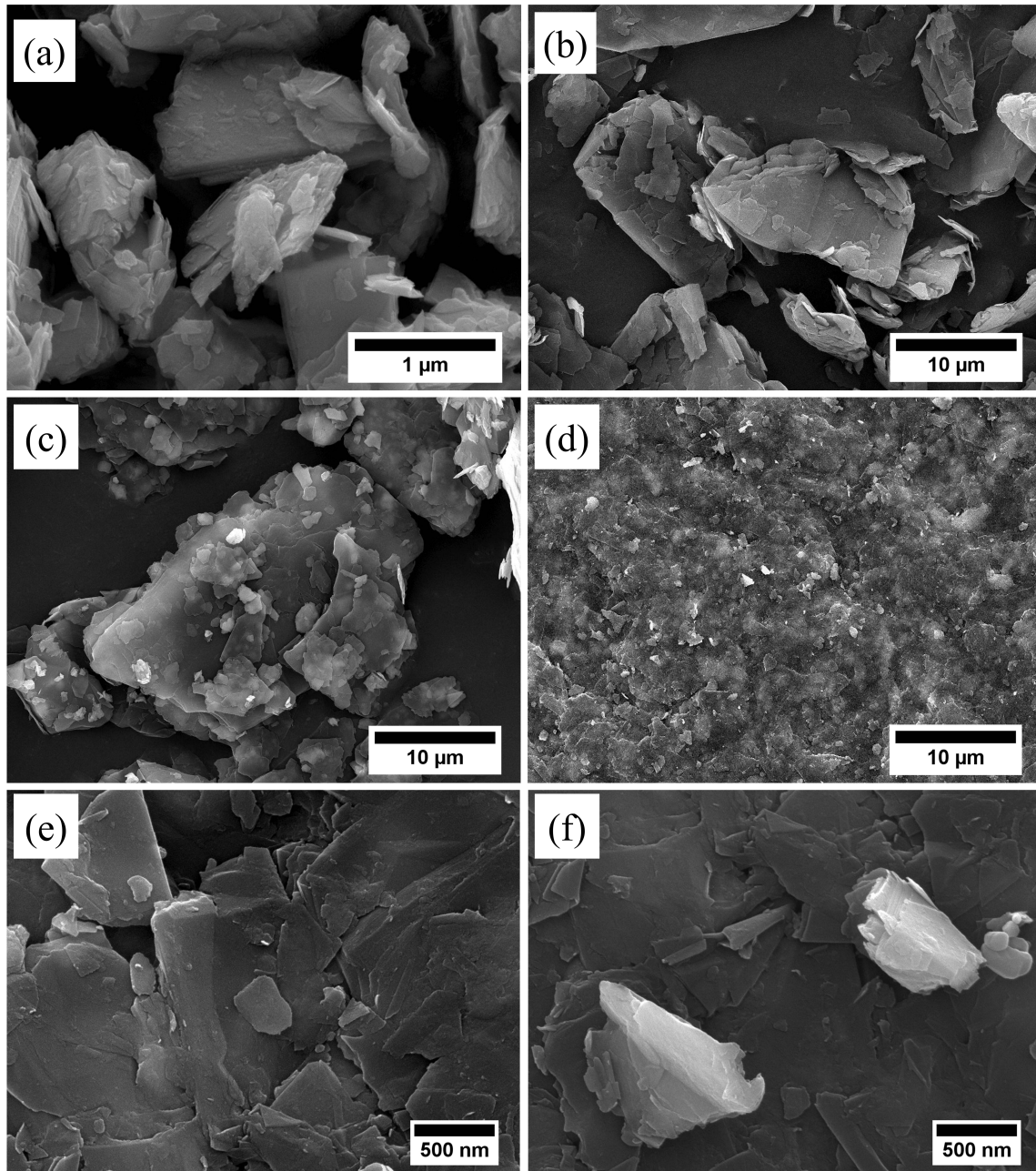


Figure 19 FE-SEM images of (a) bulk MoS₂, (b) bulk graphite, (c) mechanically mixed 15% MoS₂-graphite powder, and (d–f) 15% MoS₂-graphite deposited composite on stainless steel.

The cross-sectional image of the deposition prepared by focused ion beam show that the thickness of the deposition is ranging from 3.3 to 5 μm depending on the position as shown in Figure 20 (a). Also, the cross-sectional view indicates that the deposition is very dense with average porosity of less than 2%. The enlarged view of the cross-sectional SEM image, Figure 20 (b), suggests that the interface between the deposition and the substrate is shown almost no pores. The EDS was performed for the mechanically mixed 15% MoS_2 -graphite composite powder as shown in Figure 20 (c), and the 15% MoS_2 -graphite deposited composite film on stainless steel from the cross-section SEM as shown in Figure 20 (d). The contents of Mo, S, and C from powder and film were summarized in Table 7. The EDS results confirmed that the weight ratio of MoS_2 to graphite did was slightly changed after deposition.

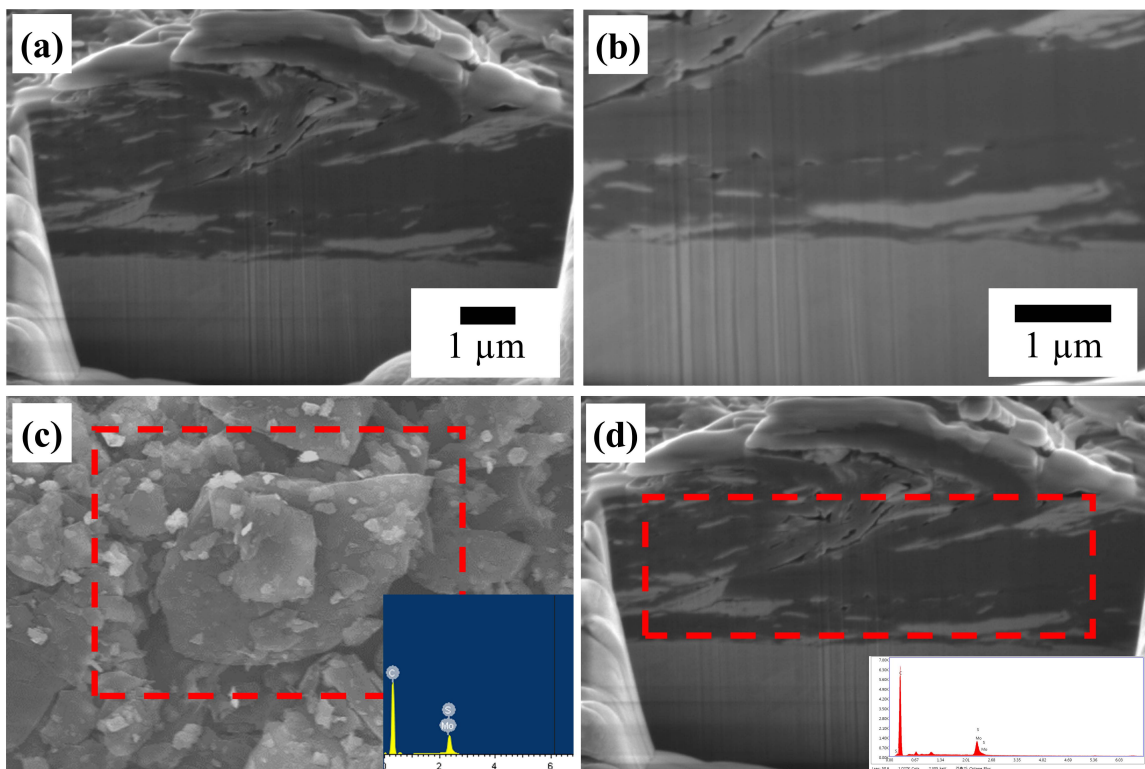


Figure 20 (a) the cross-sectional SEM image, (b) enlarged cross-sectional SEM image of 15% MoS_2 -graphite deposited composite on stainless steel, (c) FE-SEM and EDS of mechanically mixed 15% MoS_2 -graphite composite powder, and (d) SEM and EDS of 15% MoS_2 -graphite deposited composite on stainless steel.

Table 7 Composition ratio of 15% MoS₂-graphite composite before and after the deposition

	mechanically mixed 15% MoS₂-graphite composite powder	15% MoS₂-graphite deposited composite on stainless steel
	Weight %	Weight %
C	86.04	85.8
S	3.72	3.4
Mo	10.24	10.8
MoS₂:	13.96	14.2
Graphite		

4.3.2 XRD

The crystalline nature of the bulk MoS₂, bulk graphite, mechanically mixed MoS₂-graphite, and deposited MoS₂-graphite composite was measured using XRD, as shown in Figure 21. The XRD spectrum of the graphite powder shows a sharp and intensive peak (002) at $2\theta=26.39^\circ$, which is corresponding to the direction perpendicular (c-axis) to the graphite hexagonal plane. This peak indicates the highly organized layered structure with an interplanar spacing of 0.365 nm. The diffraction pattern of the bulk MoS₂ shows strong, sharp 2θ peaks at 14.261° , 32.572° , 39.429° , 44.029° , 49.677° , 58.218° and 60.02° , which corresponding to the (002), (100), (103), (006), (105), (110) and (008) planes, respectively. These peaks have a good matching with the previous reports on the hexagonal structure of MoS₂ (JCPDS card no. 37-1492)[188]. When MoS₂ and graphite were mechanically mixed by ball milling, both diffraction peaks of pure

MoS₂ and graphite appear in the pattern, which confirms that MoS₂ and graphite were successfully combined to form the MoS₂-graphite composite. After deposition, the peaks corresponding to the (100), (103), and (105) planes of the MoS₂ have vanished. The peak due to the (002) plane of the MoS₂ still appears at 14.193°. Also, peaks at 43.968° and 59.96° can be detected, corresponding to (006) and (008), respectively. These characteristics arise from the restacking of the hexagonal structure of MoS₂ layers. The full width at half maximum (*FWHM*) for the peak corresponding to the MoS₂ (002) plane is 0.168 for the bulk MoS₂ and 0.215 for the deposited MoS₂-graphite composite. The existence of peaks with high diffraction angles and planes such as (002), (006), and (008), in addition to the disappearance of the (100), (103), and (105) planes, are reliable with a restacking of the exfoliated sheets during the ball milling process. Recently, it was reported that the exfoliation of 2D TMD nanosheets by ball milling with high quality still displayed prominent peaks at higher angles[189]. Moreover, a clear peak appeared at 26.36°, corresponding to the graphite (002) peak. The *FWHM* of the deposited MoS₂-graphite composite was 0.25, which indicates the decrease in particle size of the graphite particles because of the fragmentation of the particles during the deposition since the *FWHM* was 0.172 for the MoS₂-graphite composite powder. After deposition, the MoS₂-graphite composite fragmented to a smaller size and it may show an exfoliation of MoS₂ layers after deposition of the composite.

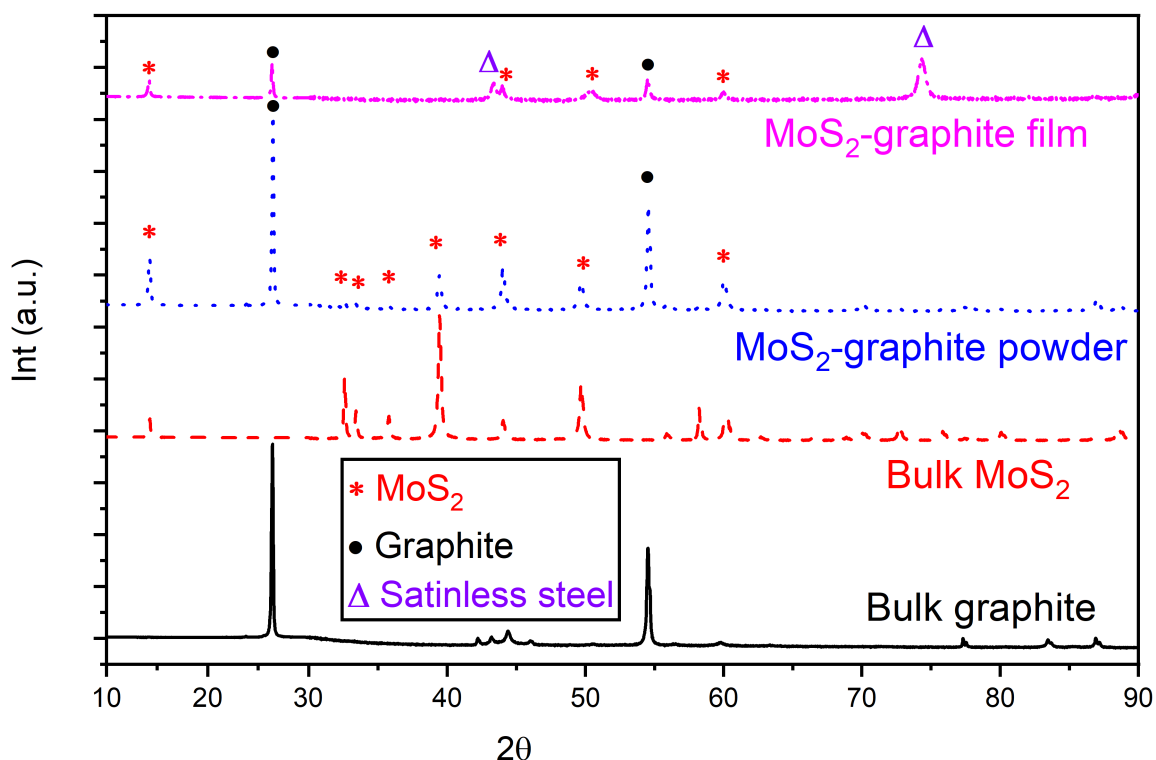


Figure 21 XRD results of bulk MoS_2 , bulk graphite, mechanically mixed 15% MoS_2 -graphite powder, and 15% MoS_2 -graphite deposited composite on stainless steel.

4.3.3 Raman Spectroscopy

For further characterization, Raman spectra were measured for the bulk MoS_2 , bulk graphite, mechanically mixed MoS_2 -graphite, and deposited MoS_2 -graphite composite. As shown in Figure 22, the D, G, and 2D peaks appear in 1350 , 1579 , and 2717 cm^{-1} , respectively, in the case of the bulk graphite, and 1350 , 1579 and 2717 cm^{-1} for the mechanically mixed MoS_2 -graphite. The G and 2D peaks are shifted to 1583 and 2706 cm^{-1} for the deposited MoS_2 -graphite composite, which confirms that the layers of graphite particles were fragmented owing to the high impact velocity during deposition on the stainless steel[134, 140]. Furthermore, the shift in the 2D peak to lower energy indicates that, during deposition of the composite, the layers of graphite particles separated to a smaller number of layers. Additionally, the increase of the D peak intensity after deposition indicates the amount of disorder in the deposited film[141, 142, 190].

For bulk MoS₂, there are two strong signals at 375.6 and 403.5 cm⁻¹, corresponding to the in-plane mode E_{2g}¹ and out-of-plane A_{1g}. Compared to the mechanically mixed powder and deposited MoS₂-graphite composite, E_{2g}¹ and A_{1g} modes appear at 380.25 and 408.09 cm⁻¹, respectively, for both cases. Meanwhile, the difference in the Raman shift is 27.84 cm⁻¹, which is the same as the bulk MoS₂. This result is different from previous reports, namely the Raman peak of in-plane E_{2g}¹ has a blue shift and the Raman peak of out-of-plane A_{1g} has a red shift. This abnormal Raman result is possibly related to an exfoliation mechanism[191]. The result also differs in that the obtained composite comprises MoS₂ and graphite.

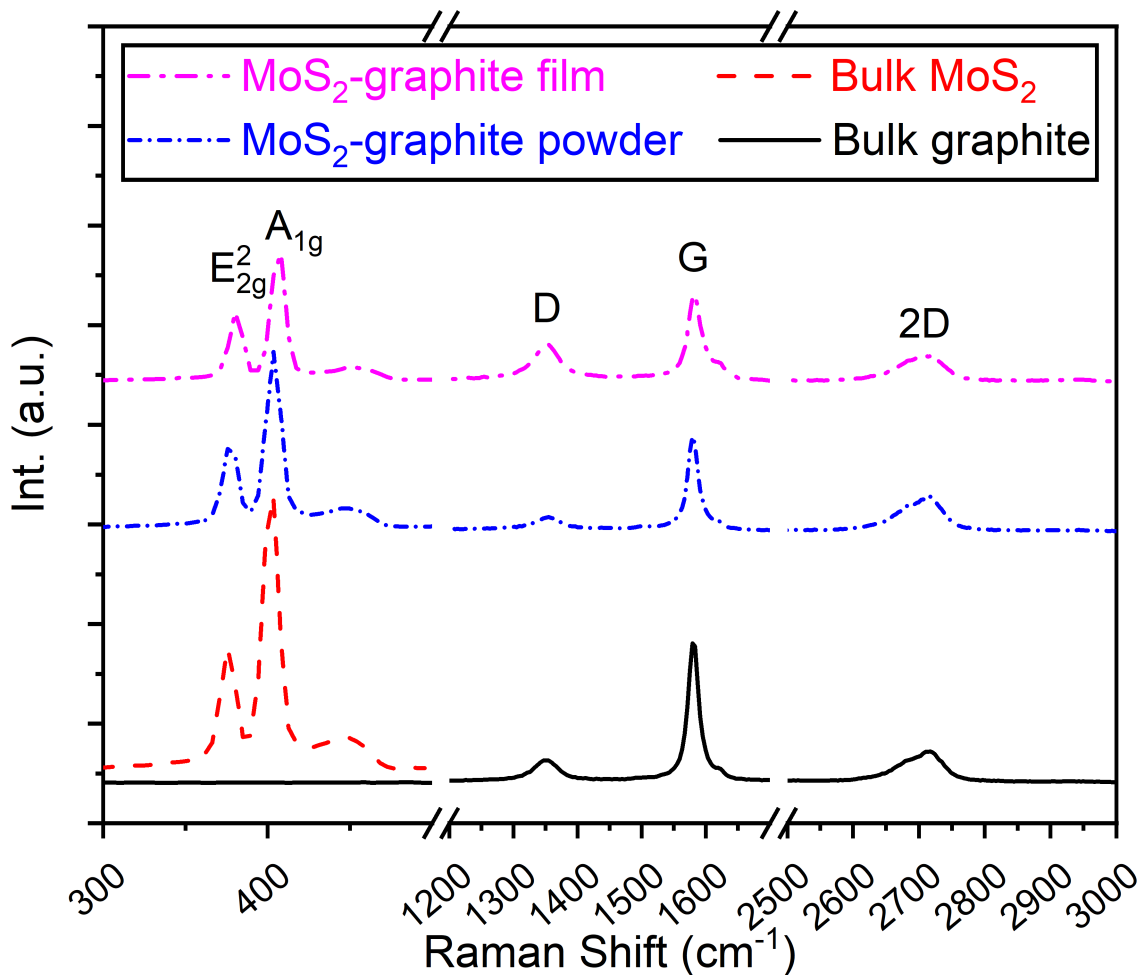


Figure 22 Raman spectra of bulk MoS₂, bulk graphite, mechanically mixed 15% MoS₂-graphite powder, and deposited 15% MoS₂-graphite composite on stainless steel.

4.3.4 Electrochemical performance

To evaluate the electrochemical performance of the MoS₂-graphite composite supercapacitor, cyclic voltammetry, and galvanostatic charge/discharge tests were performed. Figure 23 (a) shows the CV curves of the pure graphite and the MoS₂-graphite composite with supercapacitors of different composition ratios (5–30% wt.). The CV curves were measured at the scan rate of 20 mV/s and the potential window ranged from 0 to 1 V. The areal capacitance was calculated in Figure 23 (c) from the CV curves using the formula:

$$c_a = \frac{\int IdV}{sA\Delta V} \dots\dots\dots 4.1$$

where I is the response current, s denotes the scan rate, ΔV is the potential window, and A is the area of the electrode in contact with the electrolyte. The CV curves of the supercapacitors are symmetrical and have a semi-rectangular shape at the scan rate of 20 mV/s over a 1 V potential window, which is typical of an ideal capacitor. The electrosorption of H₃PO₄ ions on the surface of the film leads the rectangular shape of CV curves to be changed[192, 193]. The area of the CV curves of the MoS₂-graphite composite is larger than those of pure graphite, indicating a higher specific capacitance. The value of capacitance was 4.14 mF/cm² at a 15% composition ratio, which was the maximum value among the pure graphite supercapacitor and other MoS₂-graphite composite supercapacitors with different composition ratios.

Furthermore, the same result was measured by galvanostatic charge/discharge, as shown in Figure 23 (b), which was measured for the pure graphite supercapacitor and the MoS₂-graphite composite supercapacitors at a current 0.04 mA between 0 to 1 V potential. The areal capacitance was calculated in Figure 23 (c) from the charge/discharge curves using the formula:

$$c_a = \frac{I}{A \frac{dV}{dt}} \dots\dots\dots 4.2$$

where I is the current, A denotes the area of the electrode in contact with the electrolyte, and dV/dt is the slope of the discharge curve after the IR drop. The galvanostatic charge/ discharge curves for graphite and MoS₂-graphite composite supercapacitors showed linear charging and discharging variation with a small IR drop, showing that the electrodes had a lower internal resistance, leading to a better electric double-layer performance. At a 15% MoS₂ composition ratio, the specific capacitance was 3.77 mF/cm², which was the highest value among the pure graphite supercapacitor and other MoS₂-graphite composite supercapacitors with different composition ratios. The small MoS₂ content is not enough to increase capacitance values, while the large amount of MoS₂ may suffer from restacking and volume variation during charging/discharging. The great performance of the 15% MoS₂-graphite composite is attributed to the balance between highly conductive graphite combined with a proper amount of MoS₂ flakes to prevent restacking and provide extra surface area.

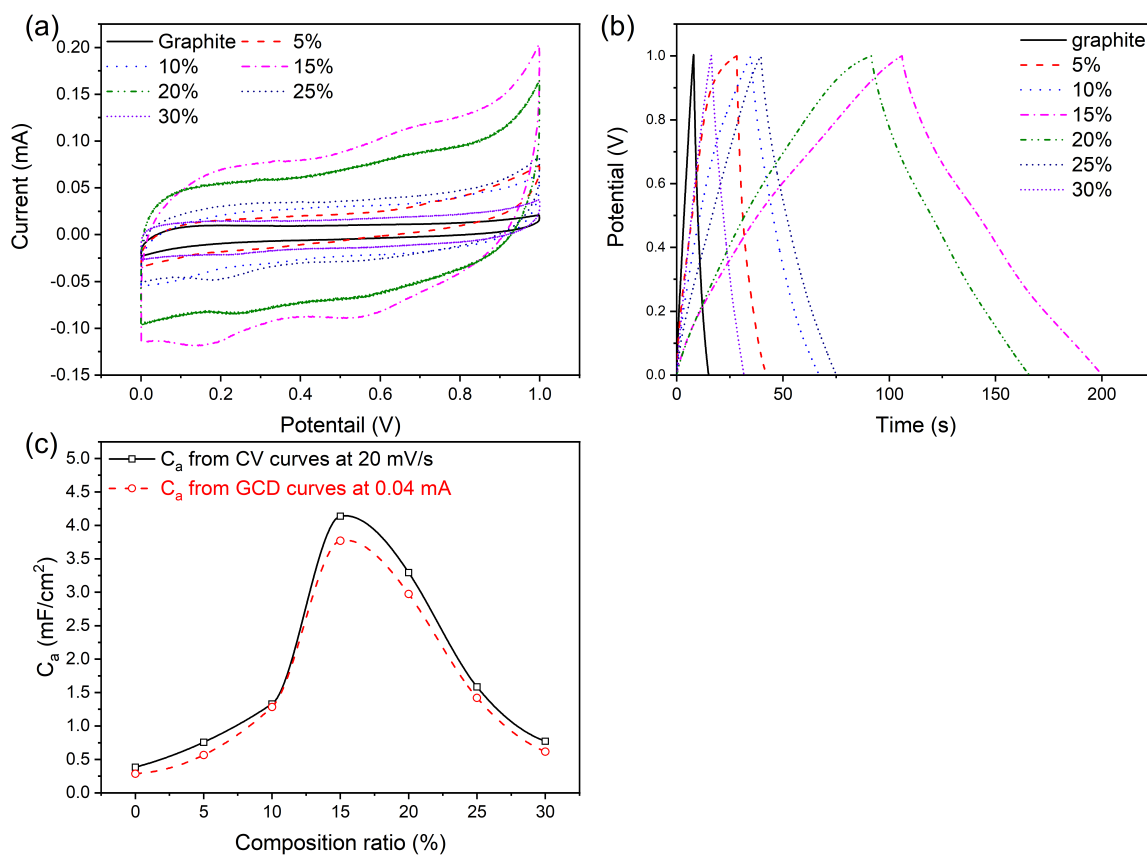
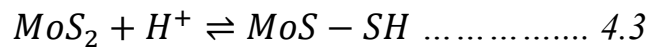


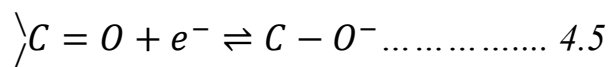
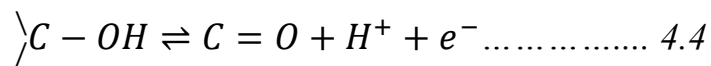
Figure 23 (a) CV curves at a scan rate of 20 mV/s, (b) galvanostatic charge/discharge at a current of 0.04 mA, and (c) specific areal capacitance calculated from CV curves and galvanostatic charge/discharge of graphite and MoS₂-graphite composite supercapacitors with different composition ratios ranging from 5 to 30%.

In a further evaluation, the CV curves for the 15% MoS₂-graphite composite supercapacitor were measured at different scan rates ranging from 2 to 100 mV/s over potential window ranging from 0 to 1V. As shown in Figure 24 (a), the CV curves have a rectangular shape at the different scan rates (2 to 100 mV/s) over a potential window of 1 V with anodic peaks, indicating that the 15% MoS₂-graphite composite supercapacitor has an EDLC effect combined with pseudocapacitance. The anodic peak around 0.6 V is observed only at slow scan rates below 20 mV/s, the slow scan rate allows the H₃PO₄ ions to diffuse into the MoS₂ layers, where there are more sites for redox charge transfer. One possible

mechanism is the electrochemical adsorption of H^+ ions into the MoS_2 layers described by the following equation[192, 193]



The other anodic peak around 0.2 V may be corresponding to the faradic reaction of the oxygen groups (quinone/hydroquinone pair) formed into the graphite layers which is described as follows[194, 195]:



The value of the specific capacitance was 5.1 mF/cm^2 at 2 mV/s , which was about eight times greater than that of the pure graphite supercapacitor. This value is comparable with the results obtained previously by other researchers. As reported previously, the MoS_2 -graphene composite (1:3 weight ratio) prepared by solution phase exfoliation showed a specific capacitance of 11 mF/cm^2 at 5 mV/s after cycling for 10,000 cycles[196]. The $MoS_2@S$ -RGO microsupercapacitor consisting of sulfonated reduced graphene oxide (S-RGO) and MoS_2 nanoflowers showed a specific capacitance of 6.56 mF/cm^2 in KOH-PVA gel electrolyte[197].

Figure 24 (b) shows the galvanostatic charge/discharge curves obtained with 15% MoS_2 -graphite composite electrodes by using two-electrode system at different currents ranging from 0.01 mA to 0.1 mA in the potential window from 0 to 1 V. The curve is nearly symmetric, and the time needed for charging and discharging is almost same, suggesting a good capacitive behavior. The IR voltage drop is observed to be negligible, which shows that the electrode has a small internal resistance. The value of the specific capacitance shown in Figure 24 (c) was 4.5 mF/cm^2 at 0.01 mA, which was approximately 11 times higher than that of the pure graphite electrode.

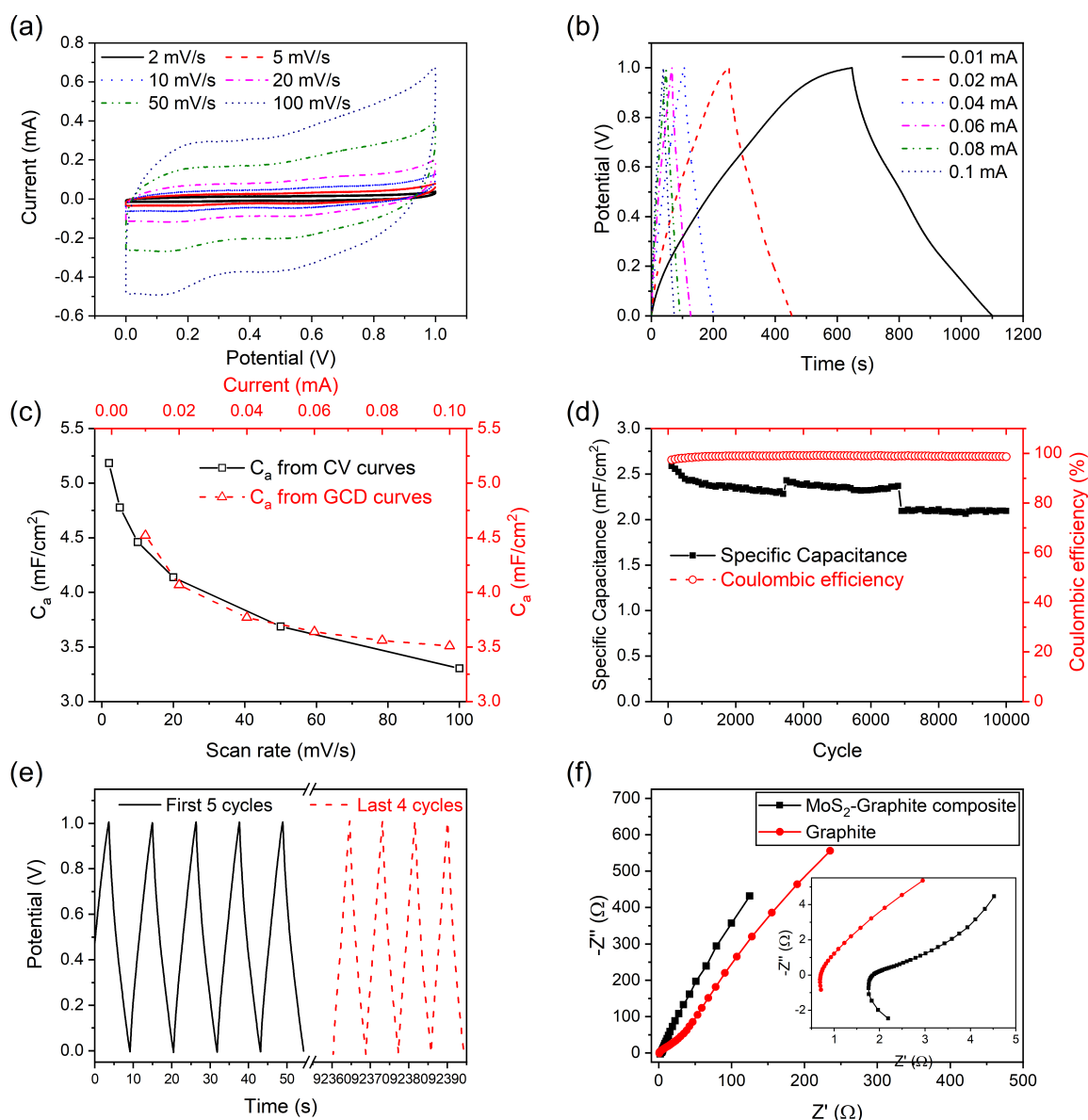


Figure 24 (a) CV curves at different scan rates of 2–100 mV/s, (b) galvanostatic charge/ discharge at a current range of 0.1–0.01 mA, (c) specific areal capacitance calculated from CV curves and galvanostatic charge/discharge, and (d) cycling performance of 15% MoS₂-graphite composite supercapacitor, (e) the charge/discharge of first 5 cycles and last 4 cycles, (f) Nyquist plots of 15% MoS₂-graphite composite supercapacitor.

The cycling stability of the 15% MoS₂-graphite composite was evaluated by repeating the galvanostatic charge/discharge test between 0 and 1 V at a current density of 0.5 mA for 10,000 cycles. Figure 24 (d) shows the performance of the 15% MoS₂-graphite composite electrode before and after the cycling test.

The charging/discharging time was almost the same before and after the cycling test as shown in Figure 24 (e). The supercapacitor has a retention of 80% of the initial value. The supercapacitor has a coulombic efficiency, which is gradually increased in the 1,000th cycle until reached a 99% coulombic efficiency. It is maintained constant until 10,000 cycles. The good cycling performance of the electrode material indicates good stability and strong adherence of MoS₂-graphite thin film to the stainless-steel substrate.

Electrochemical impedance spectroscopy provides information about the equivalent series resistance of electrode material and the charge transfer resistance between the electrode and the electrolyte. The impedance spectrum for the MoS₂-graphite composite is shown in Figure 24 (f). The spectrum is investigated using Nyquist plots. The charge transfer resistance (R_{ct}) can be calculated from the diameter of the semicircle in the high-frequency region, and the straight line in the low-frequency region represents an ideal capacitive behavior. The diameter of the semicircle is equal to the charge transfer resistance (R_{ct}) in the cell which is measured to be 1.97 Ω . The solution resistance (R_s) for the MoS₂-graphite composite is found to be 1.86 Ω . This indicates that the MoS₂-graphite composite electrode has low charge transfer resistance, and the composite, therefore, shows high specific capacitance. These results are consistent with those obtained in the CV results.

4.4 Summary

In this study, MoS₂ powder and graphite powder were mechanically mixed by ball milling with different composition ratios (5–30% wt. of MoS₂). NPDS was used to deposit pure graphite and MoS₂- graphite composites on a stainless-steel substrate at room temperature under a low vacuum condition with no chemicals. The NPDS thus provides low-cost facile preparation of the MoS₂-graphite supercapacitor having a high specific areal capacitance at room

temperature under a low vacuum condition with commercially available low-cost micro-sized powders (not nano-sized) without any toxic chemicals. The surface morphology of the 15% MoS₂-graphite composite before and after the deposition was analyzed, and it was confirmed that the composite powder was fragmented to structures smaller in size than the bulk powders. The fragmentation and layer thinning of the MoS₂-graphite flakes could be clearly observed by XRD pattern and Raman spectra. The deposited films were used as an electrode for the all-solid-state supercapacitor and the H₃PO₄-PVA gel electrolyte was used as a separator. The electrochemical performances of the fabricated all-solid-state supercapacitors were checked by CV and galvanostatic charge/discharge. The results showed that, among the supercapacitors, a 15% MoS₂-graphite composition ratio showed the best performance of 5.1 mF/cm² at 2 mV/s. The supercapacitor had good cycling stability until 10,000 cycles and low internal resistance.

Chapter 5

**Deposition of Ni(OH)₂ on
nickel substrate using
vacuum kinetic spray and its
application to high-
performance supercapacitor**

5.1 Background

The requirement of energy storage devices for wearable and portable devices, electrical and hybrid automobiles attracted a lot of researchers to focus their study on the supercapacitors. Supercapacitors or electrochemical capacitors have high-power density, ultrafast charging-discharging capability, and long durability than the conventional rechargeable batteries, and it has the ability to accumulate higher energy than the commercial capacitors[1, 5, 7]. According to the electric energy storage technique, there are two sorts of supercapacitors, electrochemical double-layer capacitors (ELDCs) and pseudocapacitors. ELDCs store energy at the electrode-electrolyte (solid-liquid) boundary, whereas in pseudocapacitors energy is stored by a reversible electrochemical redox reaction of the electrode material. Relative to ELDCs, pseudocapacitors have theoretically higher specific capacitance and thus draw interesting research attention. Several transition metal oxides or hydroxides, such as RuO_2 [52, 198-200], MnO_2 [201-203], NiO [204, 205], Co_3O_4 [206-208], and $\text{Co}(\text{OH})_2$ [209-211] exhibits high performance as active materials for pseudocapacitors. Among various pseudocapacitive materials, nickel hydroxide ($\text{Ni}(\text{OH})_2$) is an attractive candidate for pseudocapacitors due to its high theoretical capacitance caused by the large interlayer spacing, low-cost, well-defined redox activity, and eco-friendly characteristics[212, 213]. The electrochemical performance of $\text{Ni}(\text{OH})_2$ supercapacitors depend strongly on the morphology and crystal structure directly related to the fabrication techniques. Several morphologies and crystal structures of $\text{Ni}(\text{OH})_2$ have been prepared by various techniques. Few-layered $\text{Ni}(\text{OH})_2$ nanosheets were prepared by a solvothermal method with a specific capacitance of 1837 F g^{-1} at 20 A g^{-1} [214]. Spherical $\beta\text{-Ni}(\text{OH})_2$ superstructures were prepared by microwave-assisted synthesis with a specific capacitance of 2147 F g^{-1} at 1 A g^{-1} [213]. Nanostructured $\text{Ni}(\text{OH})_2$ thin films were prepared by chemical bath deposition with a specific capacitance of 610 F g^{-1} at scan rate 2 mV s^{-1} [215]. An

open-ended hexagonal nanotube nickel hydroxide electrode was fabricated by hydrolysis of NiCl_2 and hexagonal ZnO nanorods with a specific capacitance of 1328 F g^{-1} at 1 A g^{-1} [216]. However, the above techniques involve high temperature or complex processes.

In this research, direct deposition of $\text{Ni}(\text{OH})_2$ on nickel sheet and nickel foam substrates was carried out at room temperature and low vacuum condition using one of the vacuum kinetic spray methods, nano-particle deposition system (NPDS). NPDS presents a facile, low cost and environmentally friendly deposition method, which can deposit both metals and metal oxides, such as Sn, Ni, Al_2O_3 , TiO_2 , and WO_3 at room temperature without any binders. Furthermore, few-layer graphene nanoflakes and MoS_2 -graphite composite thin films have been successfully deposited using this method[79, 81, 89, 91, 92, 128, 185, 217]. The surface morphology and structures of the as-purchased $\text{Ni}(\text{OH})_2$ powder, nickel substrate, and deposited $\text{Ni}(\text{OH})_2$ on nickel sheet substrates were studied by field-emission electron microscopy (FE-SEM), X-ray diffraction (XRD), and Raman spectroscopy. The electrochemical performances of the deposited $\text{Ni}(\text{OH})_2$ on nickel sheet and nickel foam substrates were examined in a 3-electrode cell by using cyclic voltammetry (CV) and galvanostatic charge-discharge (GCD).

5.2 Experimental

5.2.1 $\text{Ni}(\text{OH})_2$ Deposition on Ni sheets

The NPDS comprised of an air compressor, powder feeder, nozzle, vacuum chamber, vacuum pump, and controller as shown in Figure 6. The air compressor supplies compressed air as a carrier gas to move micro-sized $\text{Ni}(\text{OH})_2$ powder from the powder feeder to the nozzle. The powder feeder controls the powder feeding rate by piston movement and brush. In this paper, the powder was accelerated through a rectangular opening converging-diverging nozzle with

outlet dimensions of $50 \times 0.2 \text{ mm}^2$. The process parameters are listed in Table 8. To study the deposition of $\text{Ni}(\text{OH})_2$ on nickel sheets, the deposition was carried with different carrier gas pressures and different stand-off distances (SoD) between the nozzle and substrate.

Table 8 Process parameters for $\text{Ni}(\text{OH})_2$ deposition on a nickel sheet.

Parameter	Value			
Carrier gas pressure (MPa)	0.1	0.1	0.3	0.3
SoD (mm)	2.5	5	2.5	5
Piston speed (mm min^{-1})	2			
Brush speed (rpm)	7000			
Scan speed ($\mu\text{m s}^{-1}$)	200			
Chamber pressure (MPa)	0.005	0.005	0.028	0.028
Flow rate (l min^{-1})	10	10	40	40
Substrate material	Nickel sheet			

5.3 Results and Discussion

5.3.1 Surface Morphology

The surface morphology of the $\text{Ni}(\text{OH})_2$ powder, Ni sheets substrate, and the deposited $\text{Ni}(\text{OH})_2$ films with different carrier gas pressures and SoD were analysed with FE-SEM images, as shown in Figure 25 and Figure 26. In Figure 25 (a) the FE-SEM images of the original $\text{Ni}(\text{OH})_2$ powder shows that the particles have a non-uniform size distribution of average size $8 \mu\text{m}$. The Ni sheets in Figure 25 (b) are smooth and do not have any structure. The low magnification FE-SEM images in Figure 26 (a, c, e, and g) of the deposited $\text{Ni}(\text{OH})_2$ on Ni sheet substrate with different carrier gas pressures (0.1 and 0.3 MPa) at SoD of 2.5 and

5 mm show that the films are well covered. The high magnified FE-SEM images of the deposited films, as shown in Figure 26 (b, d, f, and h), demonstrate that the micro-sized $\text{Ni}(\text{OH})_2$ particles were fragmented into nanostructures with irregular shape and oriented randomly. However, the effect of carrier gas pressure and SoD to $\text{Ni}(\text{OH})_2$ deposition on Ni sheet substrates could not clearly be confirmed with FE-SEM images. For further confirmation of the effect of carrier gas pressure and SoD, the deposition results were analyzed by the x-ray diffraction and Raman spectroscopy.

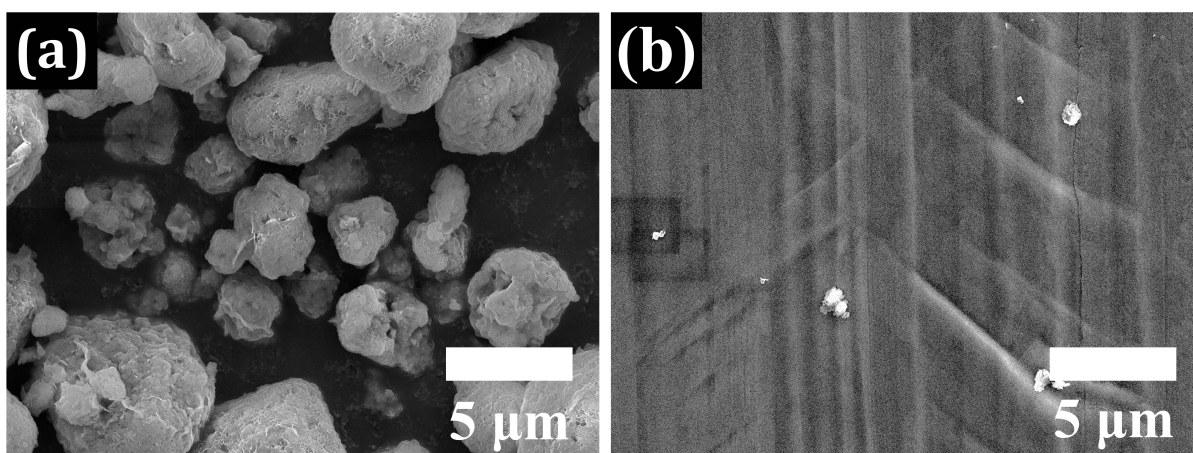


Figure 25 FE-SEM images of (a) $\text{Ni}(\text{OH})_2$ powder and, (b) Ni sheet substrate.

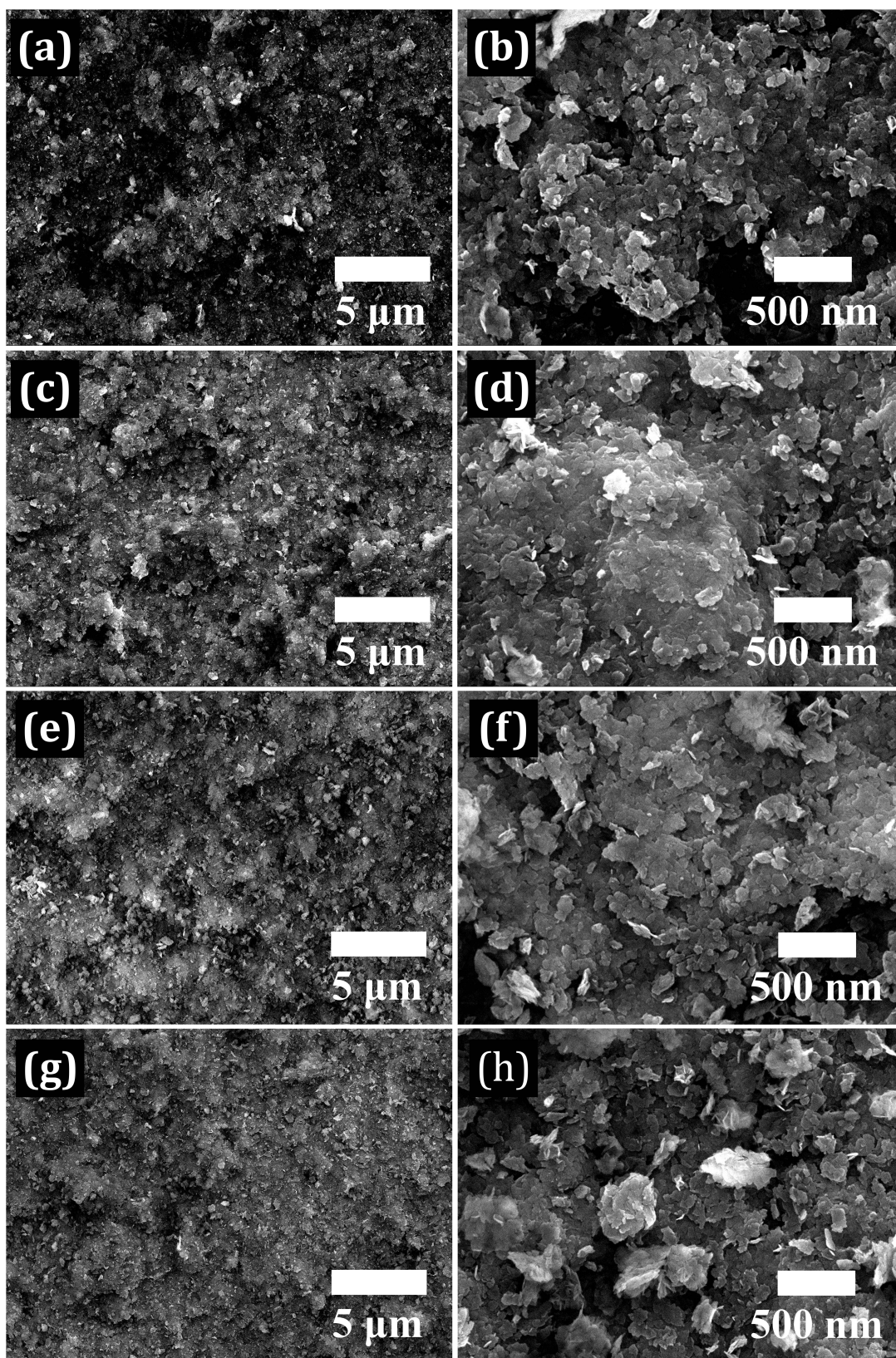


Figure 26 FE-SEM images of the deposited $\text{Ni}(\text{OH})_2$ thin films on Ni sheets with different deposition conditions, (a, b) 2.5 mm – 0.1 MPa, (c, d) 2.5 mm – 0.3 MPa, (e, f) 5 mm – 0.1 MPa and, (g, h) 5 mm – 0.3 MPa (the right images are low-magnified, and the left images are high-magnified).

5.3.2 X-ray Diffraction

The crystal structure of the original Ni(OH)₂ powder, Ni sheets, and the deposited Ni(OH)₂ film on the Ni sheet substrate were studied by X-ray diffraction (XRD). In Figure 27 (a and b), the XRD spectrum of the Ni(OH)₂ powder is well matched to a hexagonal β-Ni(OH)₂ phase (JCPDS card No. 14-0117). The XRD spectrum of the deposited Ni(OH)₂ film on the nickel sheets substrate shows the peaks at 44.3, 51.6, and 76.2° corresponding to (111), (200), and (220) respectively, which is typically observed from the Ni sheet substrate. Furthermore, the (001) shows broadening and lower shifting in the XRD peak which indicates the fragmentation of micro-sized Ni(OH)₂ powder to small crystalline Ni(OH)₂ size during deposition. This result showed that the effect of carrier gas pressure may be more dominant than SoD, so the crystallite size becomes smaller by increasing the powder pressure from 0.1 MPa to 0.3 MPa in both SoDs 2.5 and 5 mm. The crystallite size of the Ni(OH)₂ powder and deposited Ni(OH)₂ films on Ni sheets with different conditions was calculated by the Scherrer equation and shown in Table 9.

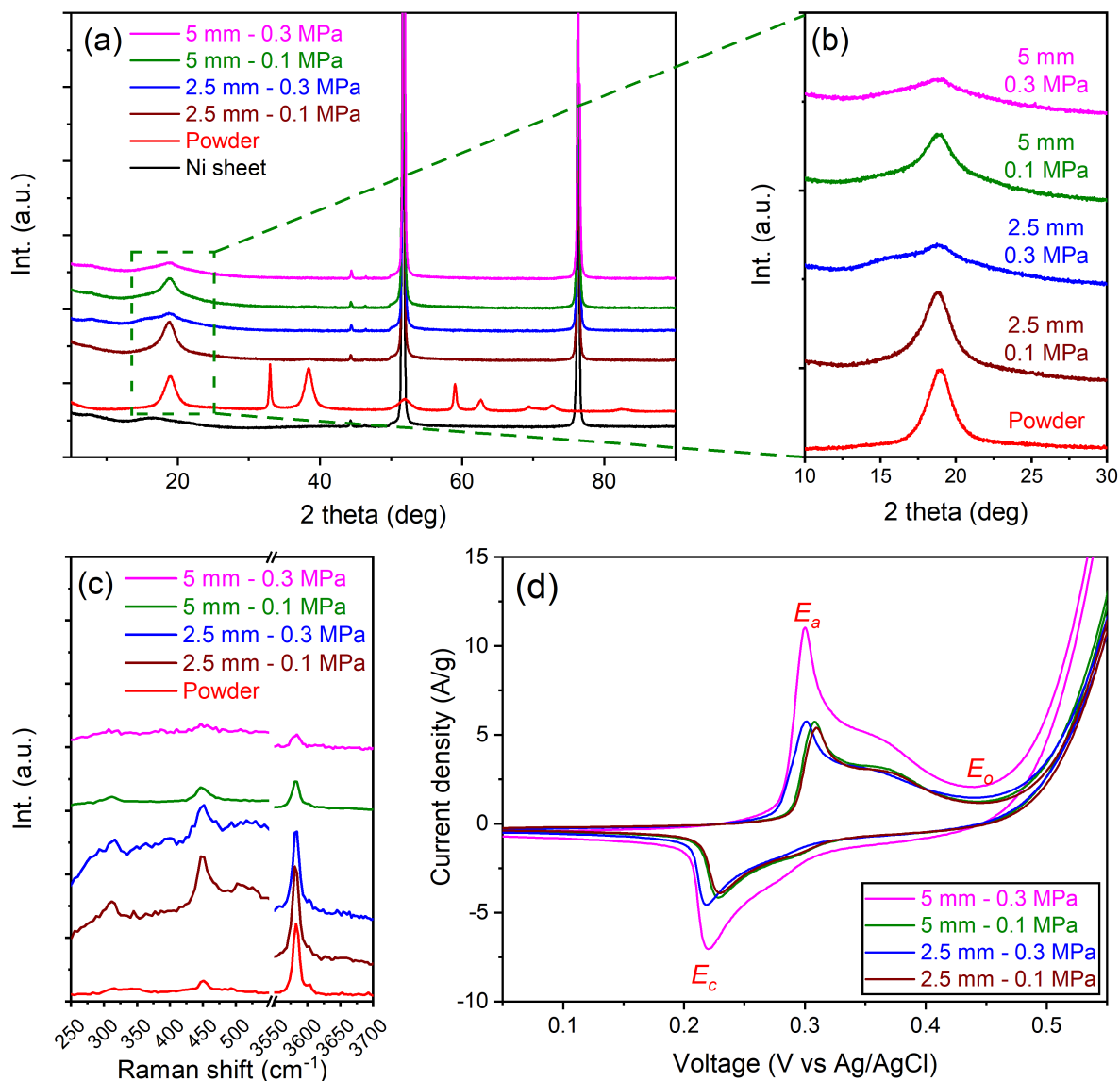


Figure 27 (a) XRD spectra, (b) enlarged view of (001) XRD peak, (c) Raman spectra of Ni(OH)₂ powder, nickel sheet, and deposited Ni(OH)₂ films with powder pressure of 0.1 MPa and 0.3 MPa in both SoDs 2.5 and 5 mm, and (d) CV curves of deposited films on nickel sheet with powder pressure of 0.1 MPa and 0.3 MPa in both SoDs 2.5 and 5 mm .

Table 9 Crystallite size of the powder and deposited films with different deposition conditions for (001) XRD peak and FWHM of 3581 cm⁻¹ Raman peak.

Sample	2θ	FWHM of (001) XRD peak	Crystallite size (nm)	FWHM of 3581 cm⁻¹ Raman peak
Powder	19	1.93	4.36	10.94
2.5 mm - 0.1 MPa	18.7	2.3	3.66	11.30
2.5 mm - 0.3 MPa	18.65	3.73	2.25	11.69
5 mm - 0.1 MPa	18.78	2.38	3.53	12.15
5 mm - 0.3 MPa	18.5	4.59	1.83	16.17

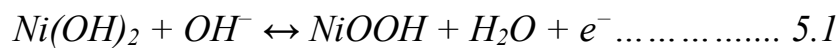
5.3.3 Raman Spectroscopy

The Raman spectra of the original Ni(OH)₂ powder, and the deposited Ni(OH)₂ film on the nickel sheets substrates were shown in Figure 27 (c). The Ni(OH)₂ powder has a peak at 311.67 cm⁻¹ assigned from E_g lattice mode, 446.8 cm⁻¹ corresponds to A_{1g} lattice mode, 3581 cm⁻¹ corresponds to A_{1g} O-H stretch where only the hydrogen atom actually vibrates[218], and 3604 cm⁻¹ due to the disordered O-H stretch. These Raman modes were observed previously in the same region[218-224]. The Raman spectra for the deposited films exhibit the same behaviour of the powder except for the value of full-width at half-maximum (FWHM) of the peak at 3581 cm⁻¹. The FWHM of the peak at 3581 cm⁻¹ increased as the powder pressure of the deposition increased from 0.1 to 0.3 MPa, and the broadening of the 3581 cm⁻¹ peak with decreasing the crystallite size for Ni(OH)₂ is also discussed by other researches[221, 225, 226]. This confirms that the increase of the impact velocity due to increased powder pressure can show a

higher degree of fragmentation and smaller crystallite size. Table 9 shows the relation between the carrier gas pressures, SoD, crystallite size calculated from XRD, and the FWHM of 3581 cm⁻¹ peak from Raman spectra.

5.3.4 Electrochemical performance

The electrochemical performance of the deposited Ni(OH)₂ films on Ni sheet with different deposition parameters were evaluated by cyclic voltammetry using a 3-electrode cell in 2M KOH aqueous solution at 10 mV s⁻¹ scan rate within the potential window from 0 to 0.6 V (vs. Ag/AgCl). In the CV curves, as shown in Figure 27 (d), a couple of redox peaks is clearly detected, and this reveals that the origin of the capacity of the deposited Ni(OH)₂ films on Ni sheet is due to faradic redox reaction. The anodic peak indicates oxidation of Ni(OH)₂ to nickel oxyhydroxide (NiOOH), whereas the cathodic peak corresponds to the reverse process. The faradic reaction at the surface of Ni(OH)₂ electrode is well defined by the following equation:



The specific capacitances were estimated from the CV curves according to the equation,

$$C_m = \int I dV / (s m \Delta V) \dots\dots\dots 5.2$$

where *I* represents the current, *s* denotes the scan rate, ΔV expresses the potential window, and *m* is the active material mass. It is clear that the deposition results with 5 mm of SoD and 0.3 MPa of carrier gas pressure shows the highest capacitance value among all deposition conditions. In addition, as shown in Table 10, this film shows the largest potential difference between the anodic potential (*E_a*) and oxygen-evolution potential (*E_o*), which indicates that the electrode is more charged before oxygen-evolution. Also, this condition has the smallest

potential difference between the anodic (E_a) and cathodic (E_c) potentials, indicating better reversibility for this film[226, 227]. Thus, the deposition with 5 mm of SoD and 0.3 MPa of carrier gas pressure is the best deposition condition as an electrode for supercapacitor application. This can be attributed to the smallest crystallite size as calculated from the XRD results in Table 9.

Table 10 Characteristic potential data of the deposited films with different deposition conditions obtained from CV curves at 10 mV s^{-1} .

Sample	E_a	E_o	E_c	E_{ac}	E_{oa}	C_m
	(mV)	(mV)	(mV)	(mV)	(mV)	(F g⁻¹)
2.5 mm - 0.1 MPa	309.8	440.9	227.4	82.41	131.14	78.3
2.5 mm - 0.3 MPa	301.5	440.1	218.6	82.89	138.65	87.1
5 mm - 0.1 MPa	307.9	440.5	228.1	79.83	132.59	80.6
5 mm - 0.3 MPa	299.9	440.1	220.1	79.83	140.23	141.4

E_a : anodic potential, E_c : cathodic potential, E_o : oxygen-evolution potential, E_{ac} : the potential difference between E_a and E_c , E_{oa} : the potential difference between E_o and E_a , and C_m : specific capacitance.

However, the capacitance of Ni(OH)_2 deposition on nickel plate was not large enough for supercapacitors.

5.3.5 Deposition of Ni(OH)_2 on nickel foam

Since nickel foam has been widely used as a substrate for electrode materials in supercapacitors due to its high porosity and large surface area, the condition of 5 mm of SoD and 0.3 MPa of carrier gas pressure was used to deposit Ni(OH)_2 powder on Ni foam substrate.

The FE-SEM image of the nickel foam in Figure 28 (a) has a microporous structure, and the high-magnified FE-SEM image of the nickel foam shows quite smooth and clean surface as shown in Figure 28 (b, c). The low-magnified image of the deposited Ni(OH)_2 film on nickel foam substrate has the similar microporous structure to the nickel foam as in Figure 28 (d). The high-magnified FE-SEM image of the deposited film shows that the micro-sized Ni(OH)_2 particles were fragmented to nanosheets with irregular shape and were deposited with random orientation on the nickel foam surface.

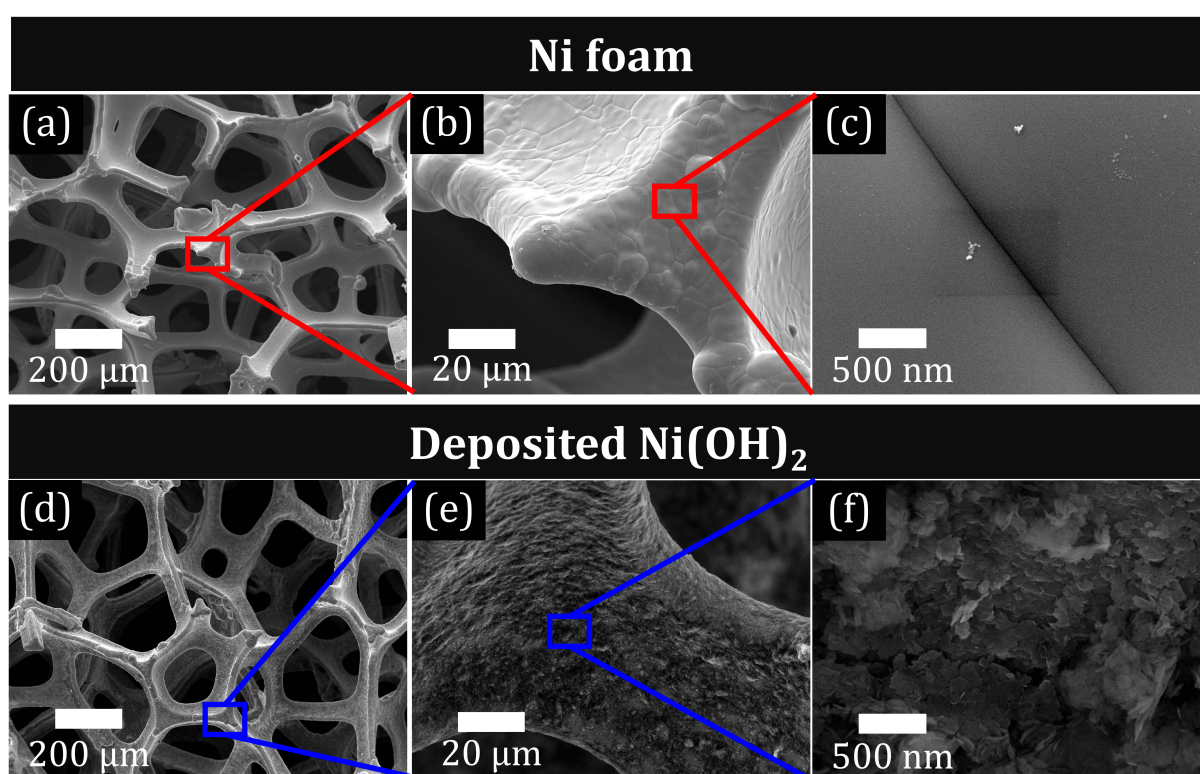


Figure 28 FE-SEM images of (a-c) nickel foam, (d-f) deposited Ni(OH)_2 on nickel foam substrate.

In Figure 29 (a), the XRD spectrum of the deposited Ni(OH)_2 film on the nickel foam substrate shows peaks at 44.25° , 51.56° , and 76.14° corresponding to (111), (200), and (220) respectively. These peaks are typically from the nickel foam substrate, and there are no more clear Ni(OH)_2 peaks appeared in the

spectrum because the deposited film might be very thin and had high degree of disorder.

The Raman spectrum of the deposited $\text{Ni}(\text{OH})_2$ film on nickel foam substrate shows peaks at 311.67, 446.8, 3581 and 3600 cm^{-1} as shown in Figure 29 (b) and the peaks correspond to E_g lattice mode, A_{1g} lattice mode, A_{1g} O-H stretch, and the disordered O-H stretch, respectively. The FWHM of the peak at 3581 cm^{-1} was 13.27 cm^{-1} and this result indicates high fragmentation degree of the micro-sized $\text{Ni}(\text{OH})_2$ powder due to the high velocity impact to the nickel foam substrate during the deposition.

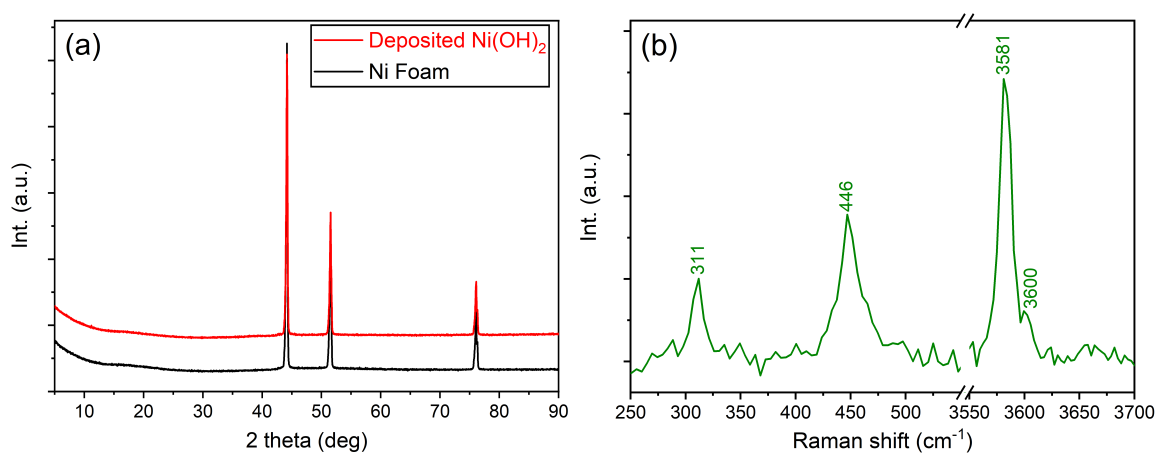


Figure 29 (a) XRD of nickel foam and deposited $\text{Ni}(\text{OH})_2$ on nickel foam substrate, (b) Raman spectrum of the deposited $\text{Ni}(\text{OH})_2$ on nickel foam substrate.

The surface chemistry of the deposited $\text{Ni}(\text{OH})_2$ was analysed by X-ray photoelectron spectroscopy (XPS). Figure 30 (a) shows that the main elements including Ni, O, and C were detected. The presence of C may be due to the adsorbed atmospheric CO_2 and sample storage in air. As shown in Figure 30 (b) for the high resolution scan of Ni 2p state, there are two major peaks with binding energies 857.74 eV and 874.94 eV corresponding to Ni $2p_{2/3}$ and $2p_{1/2}$ for $\text{Ni}(\text{OH})_2$, respectively. The high-resolution scan of Ni 2p state also contains two additional satellite peaks at 863 eV and 880.81 eV which are attributed to

Ni(OH)₂[228]. Additionally, there is a peak at 854.72 eV is due to NiO formed at the surface of the Ni foam substrate. Moreover, Figure 30 (c) shows the high-resolution spectrum of O 1s. The strong peak at 530.32 eV corresponds to Ni-O-H. After deconvolution of the O 1s spectrum, there were two additional peaks at 531.8 eV attributed to Ni-O-Ni, which revealed that the nickel foam contains NiO[228], and 533.57 eV, which ascribed to intercalated H₂O molecules within the layered Ni(OH)₂ structure and adsorbed species on the surface[229].

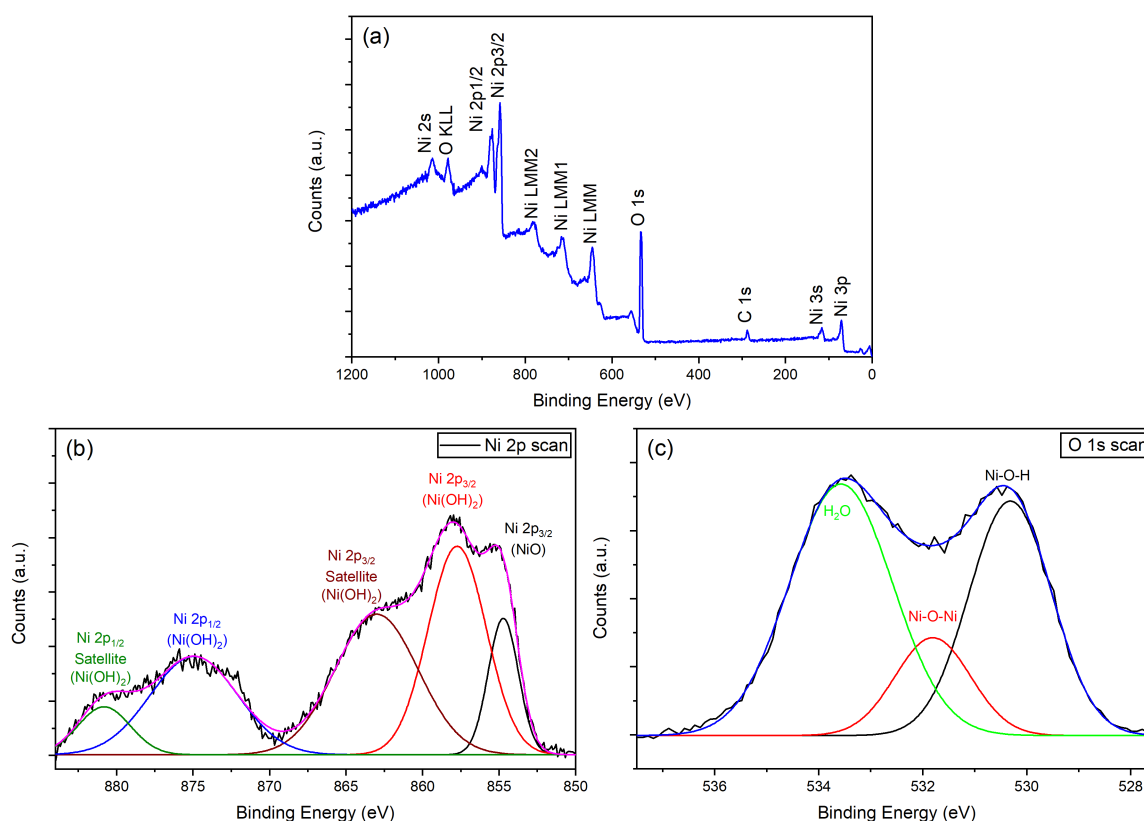


Figure 30 (a) XPS survey, (b) high-resolution XPS scan of Ni 2p, and (c) high-resolution XPS scan of O 1s for the deposited Ni(OH)₂ on nickel foam substrate.

The CV curves of the deposited film on nickel foam with scan rates from 2 to 100 mV s⁻¹ are shown in Figure 31 (a). The shape of CV curves does not show any clear significant change, and it reveals outstanding electrochemical performance of the electrode due to the straightforward adsorption and diffusion of ions onto the deposited Ni(OH)₂ film. From the CV curves, the specific

capacitance was 2377 F g⁻¹ at 2 mV s⁻¹ scan rate. The specific capacitance contribution from the nickel foam as a current collector can be ignored since the area of the CV curve of the pure Ni foam is negligibly small compared to the deposited Ni(OH)₂ film. This phenomenon is consistent with previous reports[230, 231]. Figure 31 (b) shows the GCD curves of the deposited Ni(OH)₂ films in 2M KOH aqueous solution from 0 to 0.4 V (vs. Ag/AgCl) at different current densities ranging from 1 to 20 A g⁻¹. The shape of charge-discharge curves ascribed to the pseudocapacitive behaviour of the deposited Ni(OH)₂ films. The specific capacitance can be estimated from,

$$C_m = I \Delta t / (m \Delta V) \dots\dots\dots 5.3$$

where *I* expresses the current, *Δt* denotes the discharging time, *m* is the mass of active material, and *ΔV* is the potential window. The specific capacitance was 2092 F g⁻¹ at 1 A g⁻¹. The performance of the deposited Ni(OH)₂ film on nickel foam substrate by the NPDS is comparable or even better than other researches such as spherical β-Ni(OH)₂ superstructures by microwave-assisted synthesis of specific capacitance 2147 F g⁻¹ at 1 A g⁻¹ current density[213], Ni(OH)₂ nanorods of 1150 F g⁻¹ at 1 mV s⁻¹[232], and mesoporous α-Ni(OH)₂ with the capacitance of 1718 F g⁻¹ at 5 mV s⁻¹ [233]. Ni(OH)₂ nanosheets demonstrates a specific capacitance of 2384.3 F g⁻¹ at 1 A g⁻¹[234]. Ni(OH)₂ nanoflowers/graphene hydrogel exhibits a specific capacitance of 1632 at 1 A g⁻¹[235]. 3D Flower-Like Ni(OH)₂ shows a specific capacitance of 1567 F g⁻¹ at 1 A g⁻¹[236]. Chemically precipitated Ni(OH)₂ over graphite foil shows a capacitance of 701 F g⁻¹ at 1 A g⁻¹[237]. Hierarchical Ni(OH)₂ nanotubes with ultrathin nanoflakes exhibit a specific capacitance of 1319 F g⁻¹ at 3 A g⁻¹[238]. The cyclic stability of the deposited Ni(OH)₂ film on nickel foam substrate was tested by repeating cyclic voltammetry for 3000 cycles at 100 mV s⁻¹. As shown in Figure 31 (d), the specific capacitance showed 83% capacitance retention from its initial

capacitance value after 3000 cycles, which reveals that the deposited Ni(OH)₂ electrode exhibited long-term cyclic stability.

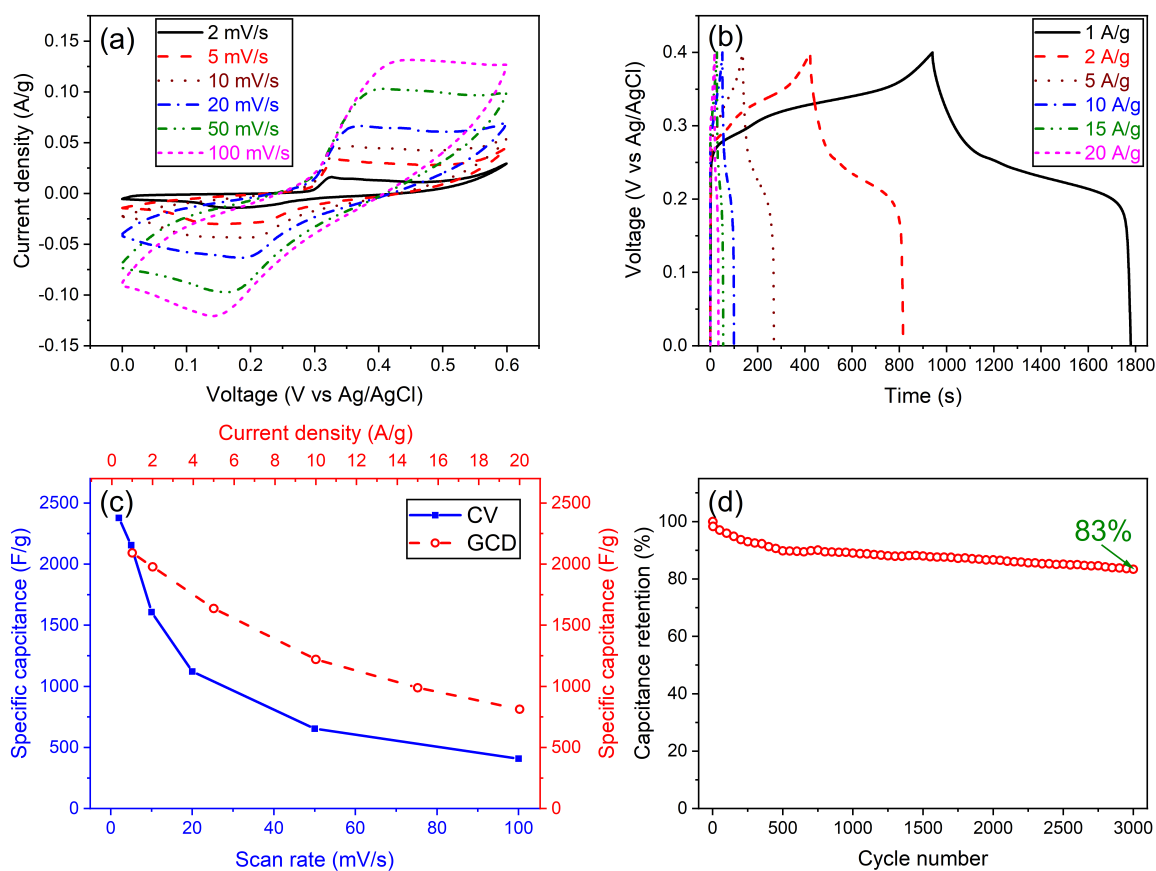


Figure 31 (a) CV curves at different scan rates, (b) galvanostatic charge-discharge curves at different current density, (c) calculated specific capacitance from CV and GCD curves, and (d) cyclic stability of the deposited Ni(OH)₂ films on nickel foam substrate.

5.4 Summary

In summary, micro-sized Ni(OH)₂ powder was directly deposited on a nickel sheet and nickel foam for supercapacitor without any binders by the NPDS, which is a facile, room temperature, and low vacuum deposition method. The deposition behaviour of Ni(OH)₂ on nickel sheets by NPDS was characterized by FE-SEM, XRD, and Raman spectroscopy, and those results showed that the size of the nano-structured Ni(OH)₂ depended on the SoD and the carrier gas pressure. Electrochemical studies of the nano-structured Ni(OH)₂ deposited on nickel sheets suggested that the deposition with 5 mm of SoD and 0.3 MPa of carrier

gas pressure was the optimum deposition condition for the nano-structured Ni(OH)₂ as an electrode material. The nano-structured Ni(OH)₂ deposited on nickel foam demonstrates a very high specific capacitance of 2377 F g⁻¹ at 2 mV s⁻¹ scan rate from CV curves and 2092 F g⁻¹ at 1A g⁻¹ current density from GCD curves. NPDS exhibits binder-free, low-cost deposition of nano-structured Ni(OH)₂ on nickel foam and excellent cyclic stability for 3000 cycles with 83% capacitance retention, which makes it a promising electrode material for high-performance supercapacitors.

Chapter 6

**High energy density
asymmetric supercapacitors
based on Ni(OH)₂-graphene
hybrid electrode**

6.1 Background

Recently, supercapacitors have received extensive attention because they can rapidly deliver energy and power densities higher than conventional capacitors and batteries. Therefore, they have been extensively used in several applications, such as wearable devices, electric vehicles, and several other devices. These applications require high power density and long cycling stability. Commonly, supercapacitors are classified into two categories according to their charging mechanism, electric double-layer capacitors (EDLCs) and pseudocapacitors. The storage mechanism of EDLCs is achieved by the interface layer formed between the electrode and the electrolyte. EDLCs use carbon materials, such as graphene, reduced graphene oxide, carbon nanotubes, or activated carbon, because of their large surface area and excellent electrical conductivity[97, 162-169]. Pseudocapacitors use metal oxides, metal hydroxides, or conducting polymers, in addition to their composites with carbon-based materials. Pseudocapacitive behavior is achieved by reversible redox reactions on the electrode material. The advantage of pseudocapacitors over EDLCs is their high energy density, but they have insufficient cycle stability[96, 170-172]. However, the energy density of the supercapacitors is much lower than that of conventional batteries (it is typically less than 10 W h kg^{-1} for supercapacitors) which hinders their extensive application in energy storage devices[239]. To increase the energy density (E) of supercapacitors, great progress has been made to increase the specific capacitance (C) or operational potential (V) according to the equation $E=0.5CV^2$. Recently, asymmetric supercapacitors (ASCs) have experienced excellent performance due to their small ionic resistivity, low cost, and environmentally friendly aqueous electrolytes[240]. These ASCs usually consist of two different electrodes. The positive electrode is a composite-based redox electrode (as an energy source). The negative electrode is an EDLC electrode (as a power source). This combination uses the operating potentials of both electrodes to increase the

operating potential of the ASC. To improve the performance of the ASCs, choosing the positive and negative electrode materials becomes essential[241].

Nickel hydroxide ($\text{Ni}(\text{OH})_2$) is a promising candidate for the positive electrode material due to its high theoretical capacitance of 2082 F g^{-1} caused by the large interlayer spacing, low cost, well-defined redox activity, and eco-friendly characteristics[212, 213]. However, the poor conductivity of $\text{Ni}(\text{OH})_2$ limits its ability to reach the theoretical capacitance. To solve this problem, a hybrid electrode is composed of $\text{Ni}(\text{OH})_2$ and carbon-based materials, such as carbon nanotubes, activated carbon, or graphene. Graphene has been studied extensively as an energy storage material due to its large surface area, excellent electrical conductivity, chemical stability, and fast ion diffusion. The combination of $\text{Ni}(\text{OH})_2$ and graphene has the advantages of the two components to achieve high capacitance and fast electron and ion transportation. Additionally, the combination between $\text{Ni}(\text{OH})_2$ and graphene can increase stability during cycling.

Many studies have sought to design a binder-free electrode to overcome the poor conductivity of polymeric binders. Moreover, binders affect the charge transfer between the active material and electrolyte, resulting in poor performance[242].

In the present work, a one-step, binder-free nickel hydroxide-graphene ($\text{Ni}(\text{OH})_2\text{-Gr}$) hybrid electrode has been successfully deposited on nickel foam by a nanoparticle deposition system (NPDS). NPDS offers a facile, low cost, and eco-friendly deposition method. NPDS is a vacuum kinetic spray method that works at room temperature and low vacuum conditions. NPDS has been used to deposit several materials, such as Cu, Sn, Ni, NiO, Al_2O_3 , TiO_2 , WO_3 , and other composites[79, 83, 84, 89, 90, 127, 128, 243]. Furthermore, NPDS has been used successfully for multiple applications, such as supercapacitors[185, 244],

photocatalysis[245], smart windows[246], and dye-sensitized solar cells (DSSCs)[82].

The electrochemical performances of the Ni(OH)₂-Gr hybrid on nickel foam were tested with different Ni(OH)₂ contents. The Ni(OH)₂-Gr hybrid achieves a high specific capacitance of 3400 F g⁻¹ for 10% Ni(OH)₂ content and shows good rate capability and cyclic stability. An asymmetric supercapacitor was successfully assembled from the Ni(OH)₂-Gr hybrid as a positive electrode and reduced graphene oxide (rGO) as a negative electrode. This supercapacitor presents a high energy density of 64 W h Kg⁻¹ and also good stability.

6.2 Experiment

6.2.1 Deposition of Ni(OH)₂-Gr composite powder

Ni(OH)₂ and graphite powders were mixed with different Ni(OH)₂ contents (10~80 wt.%) using ball milling (GLBM-G, Global Lab Co., Ltd., Korea) for 6 h rotating at 600 rpm. 5 mm zirconia balls with a ball-to-powder mass ratio of 10:1 were used in this process. Then, NPDS (Figure 6) was used to deposit pure graphite (denoted as 0%), pure Ni(OH)₂ (denoted as 100%), and the composite powders (10~80%). The deposition was carried out at a scanning speed of 100 μm/s through a slit converging-diverging nozzle (dimensions: 50 × 0.2 mm²; flow rate: 25 l/min; carrier gas pressure: 0.2 MPa; stand-off distance (SoD): 5 mm). The powder feeding rate was controlled by brush rotation at 7000 rpm and piston movement. The piston speed was changed according to Ni(OH)₂ content to achieve loading masses that are relatively near to each other, as shown in Table 11. Finally, blown air was used to remove the residual powder.

Table 11 Deposition parameters for the Ni(OH)₂-graphene hybrid electrodes deposited on nickel foam with different Ni(OH)₂ content (0~100% by wt.). (The piston speed was reduced according to Ni(OH)₂ content to achieve similar loading masses).

Parameter	Deposition parameters for different Ni(OH) ₂ content (0~100% by wt.)							
	0%	10%	20%	30%	40%	60%	80%	100%
Carrier gas pressure (MPa)	0.2							
SoD (mm)	5							
Piston speed (mm min ⁻¹)	17	17	17	14	12	10	10	8
Brush speed (rpm)	7000							
Scan speed (μm s ⁻¹)	100							
Chamber pressure (MPa)	0.01~0.016							
Flow rate (l min ⁻¹)	25							
Loading mass (mg cm ⁻²)	0.73	1.11	1.42	1.37	1.29	1.49	1.5	1.23

6.2.2 Preparation of reduced graphene oxide (rGO)

Graphene oxide (GO) was prepared by Hummer's method[247]. Then, 10 μl of hydrazine hydrate was added to 100 mL aqueous solution of GO (1 mg/mL). The mixture was stirred for 1 hour at 80°C. Hydrazine hydrate was used to reduce oxygen-containing functional groups excluding carboxyl groups. To reduce the carboxyl groups and remaining oxygen-containing functional groups, 1 mg of NaBH₄ was added to the mixture and stirred for 36 hours at 100°C. The mixture was filtered and washed by deionized water and dried at 60°C to obtain the rGO powder.

6.3 Results and Discussion

6.3.1 Positive electrode material

The morphologies of the raw graphite and Ni(OH)₂ powders and the 10% Ni(OH)₂-Gr composite deposited on the nickel foam substrate were observed by FESEM. Figure 32 (a) shows that the graphite powder has a size of around 20 μm and irregularly shaped flakes. Additionally, the FESEM images of the Ni(OH)₂ powder show that the particles have a non-uniform size distribution with an

average size of 8 μm , as shown in Figure 32 (b). Figure 32 (e) shows the SEM images of the 10% $\text{Ni}(\text{OH})_2\text{-Gr}$ deposited composite, indicating a high porous structure similar to the nickel foam substrate (Figure 32 (d)). Additionally, it is obvious that the micro-sized $\text{Ni}(\text{OH})_2\text{-graphite}$ mixed powder (Figure 32 (c)) was fragmented into nanoflakes of sizes ranging from several tens to several hundreds of nanometers with irregular shapes and were deposited with random orientation on the nickel foam surface. The 3D interconnected structure of the nickel foam does not suffer any collapse, demonstrating the strong mechanical strength of the 10% $\text{Ni}(\text{OH})_2\text{-Gr}$ deposited composite. Furthermore, the energy dispersive X-ray spectroscopy (EDS) mappings of C, O, and Ni were considered from a small region on the deposited film, as shown in Figure 32 (f), demonstrating a continuous, uniform distribution of $\text{Ni}(\text{OH})_2$ and graphene nanoflakes on the nickel foam surfaces.

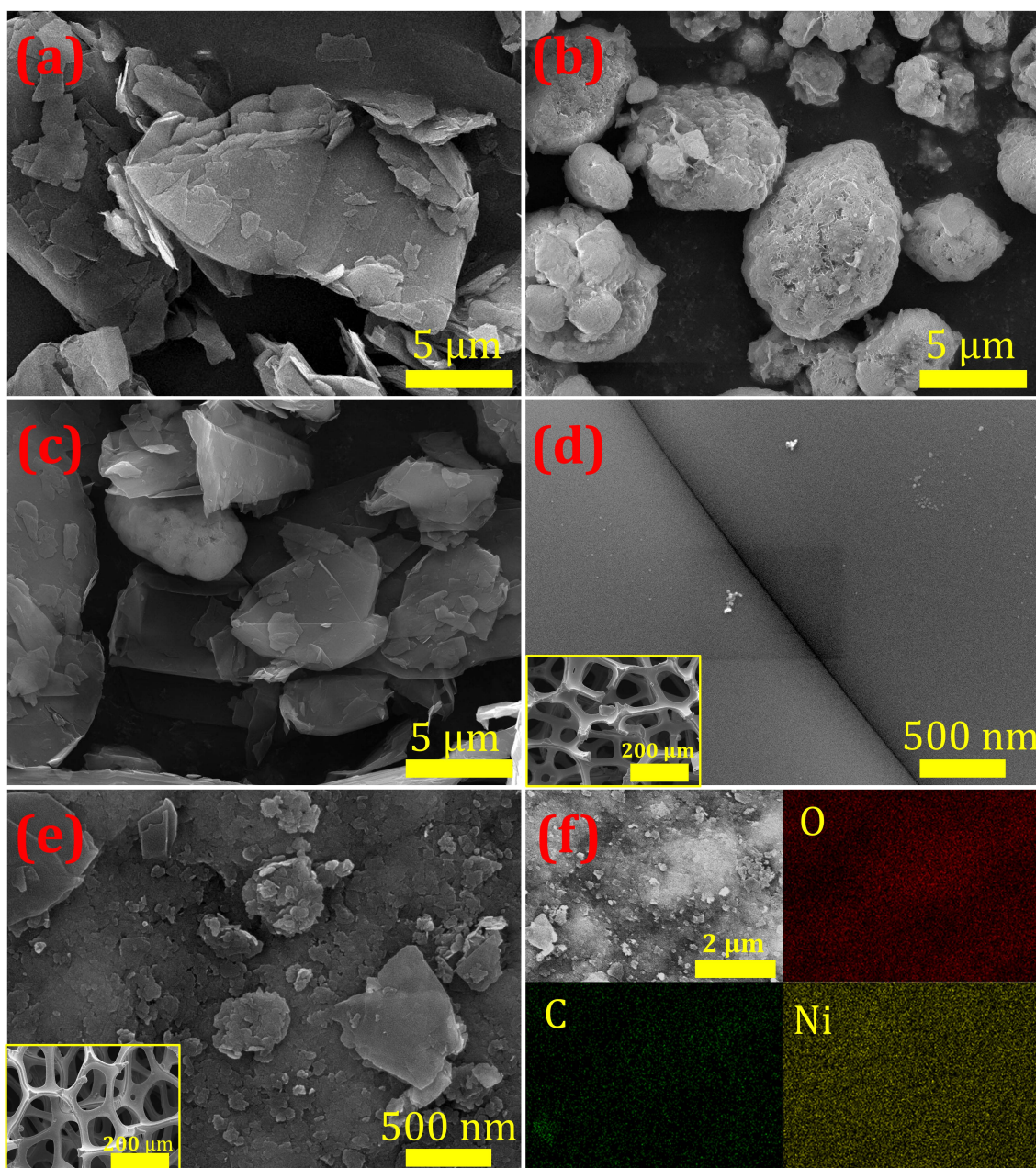


Figure 32 FESEM images of (a) raw graphite powder, (b) raw Ni(OH)_2 powder, (c) mixed Ni(OH)_2 -graphite powder, (d) nickel foam, (e) 10% Ni(OH)_2 -Gr deposited composite, and (f) EDS mapping of the 10% Ni(OH)_2 -Gr deposited composite.

The structural properties of raw powders and the deposited film on nickel foam was characterized using XRD analysis. Figure 33 (a) shows the XRD pattern of the raw graphite powder. The sharp peak (002) at $2\theta=26.5^\circ$ corresponds

to the interplanar spacing of 3.65 Å. The XRD pattern of the Ni(OH)₂ powder is well matched to a hexagonal β-Ni(OH)₂ phase (JCPDS no. 14-0117)[248]. The XRD spectrum of the 10% Ni(OH)₂-Gr deposited film on the nickel foam substrate shows peaks at 44.25°, 51.56°, and 76.14°, corresponding to (111), (200), and (220), respectively. These peaks are typically from the nickel foam (JCPDS no. 01-1258)[249]. A broad peak appearing around 17.7° corresponding to ~5 Å is very weak and highly dispersive. This peak neither matches with β-Ni(OH)₂ nor α-Ni(OH)₂ phases. This characteristic is related to β_{bc} (bc: badly crystalline) Ni(OH)₂ with interstratification of α and β motifs[250]. The new phase of Ni(OH)₂ has formed as a result of stacking faults randomly distributed in the crystal lattice[248, 251]. The existence of stacking faults leads to high electrochemical performance as reported previously[218, 251].

The Raman spectra of the graphite and Ni(OH)₂ powders and deposited composite film are displayed in Figure 33 (b). It is clear that the raw graphite powder has three bands at 1350 cm⁻¹, 1579 cm⁻¹, and 2717 cm⁻¹, corresponding to D, G, and 2D, respectively. The Raman spectrum of the raw graphite suggests a highly crystalline structure as described previously[91, 92, 217, 244, 245]. The Raman spectrum of the raw Ni(OH)₂ powder has a peak at 311.67 cm⁻¹ assigned to the E_g lattice mode, 446 cm⁻¹ corresponds to the A_{1g} lattice mode, 3582 cm⁻¹ corresponds to A_{1g} O-H stretch, and the shoulder at 3604 cm⁻¹ is due to the disordered O-H stretch.

The 10% Ni(OH)₂-Gr deposited composite film shows Raman peaks at 1350 cm⁻¹, 1589 cm⁻¹, and 2684 cm⁻¹, corresponding to D, G, and 2D, respectively. The D band intensity is higher than that of the G band. In other words, I_D/I_G (~1.24) for the deposited film is much higher than I_D/I_G (~0.35) for the graphite powder. Increasing the intensity of the D band is ascribed to the disorder and edge defects of the deposited graphene[143]. This disorder originates from the fragmentation that occurred during the deposition due to the

impact between the deposited particles and the substrate, and the deposited particles were randomly oriented. The G and 2D peaks were shifted to higher and lower Raman shifts, respectively, compared with graphite powder. Additionally, the 2D peak became sharper. Moreover, a shoulder appears at 1617 cm^{-1} , corresponding to D' . From these observations, we can say that the micro-sized graphite powder was fragmented and exfoliated to few-layer graphene nanoflakes on the nickel foam[134-139]. Additionally, the peaks at 311.67 cm^{-1} , 446.8 cm^{-1} , and 3582 cm^{-1} may be attributed to the E_g lattice mode, A_{1g} lattice mode, and A_{1g} O-H stretch, respectively.

XPS was employed to analyze the chemical state of the 10% $\text{Ni(OH)}_2\text{-Gr}$ deposited composite. As shown in Figure 33 (c), the survey scan of the 10% $\text{Ni(OH)}_2\text{-Gr}$ deposited composite confirms the presence of Ni, O, and C in the composite. This result is consistent with the EDS result. The high-resolution scan of the C 1s spectrum is represented in Figure 33 (d). There are some oxygen-containing functional groups, including the non-oxygenated C in sp^2 C-C at 284.4 eV, the carbon in C-O at 286 eV, and the carbon in C=O at 287.6 eV. These groups are hydrophilic functional groups. The hydrophilicity of the $\text{Ni(OH)}_2\text{-Gr}$ composite can improve the wettability of the electrode and further improve the interface layer formed between the electrolyte and the electrode surface. Moreover, these functional groups can interact with Ni(OH)_2 by several types of bonds, such as covalent bonds, van der Waals forces, or hydrogen bonds, thus allowing good adhesion between the graphene and Ni(OH)_2 in the composite. This is also clear from the formation of the Ni-C bond at 284.9 eV. As shown in Figure 33 (e) for the high-resolution scan of the Ni 2p state, there are two major peaks with binding energies at 855.8 eV and 873.5 eV ascribed to Ni $2p_{3/2}$ and $2p_{1/2}$, respectively, with a spin-energy separation of 17.7 eV, which is characteristic of a Ni(OH)_2 phase. Furthermore, the satellite peaks at 861.7 eV (Ni $2p_{3/2}$ sat.) and 879.5 eV (Ni $2p_{1/2}$ sat.) are attributed to Ni(OH)_2 , and they are

in agreement with earlier reports[228]. Figure 33 (f) shows the high-resolution scan of the O 1s spectrum. The peak at 530.5 eV is attributed to the C-O-Ni bond. The peak at 531.1 eV corresponds to C=O groups or the peak of O 1s in Ni(OH)₂, and the peak at 531.7 eV is assigned to C-OH and/or C-O-C. The Raman and XPS results confirm that Ni(OH)₂ has been anchored onto the graphene nanoflakes.

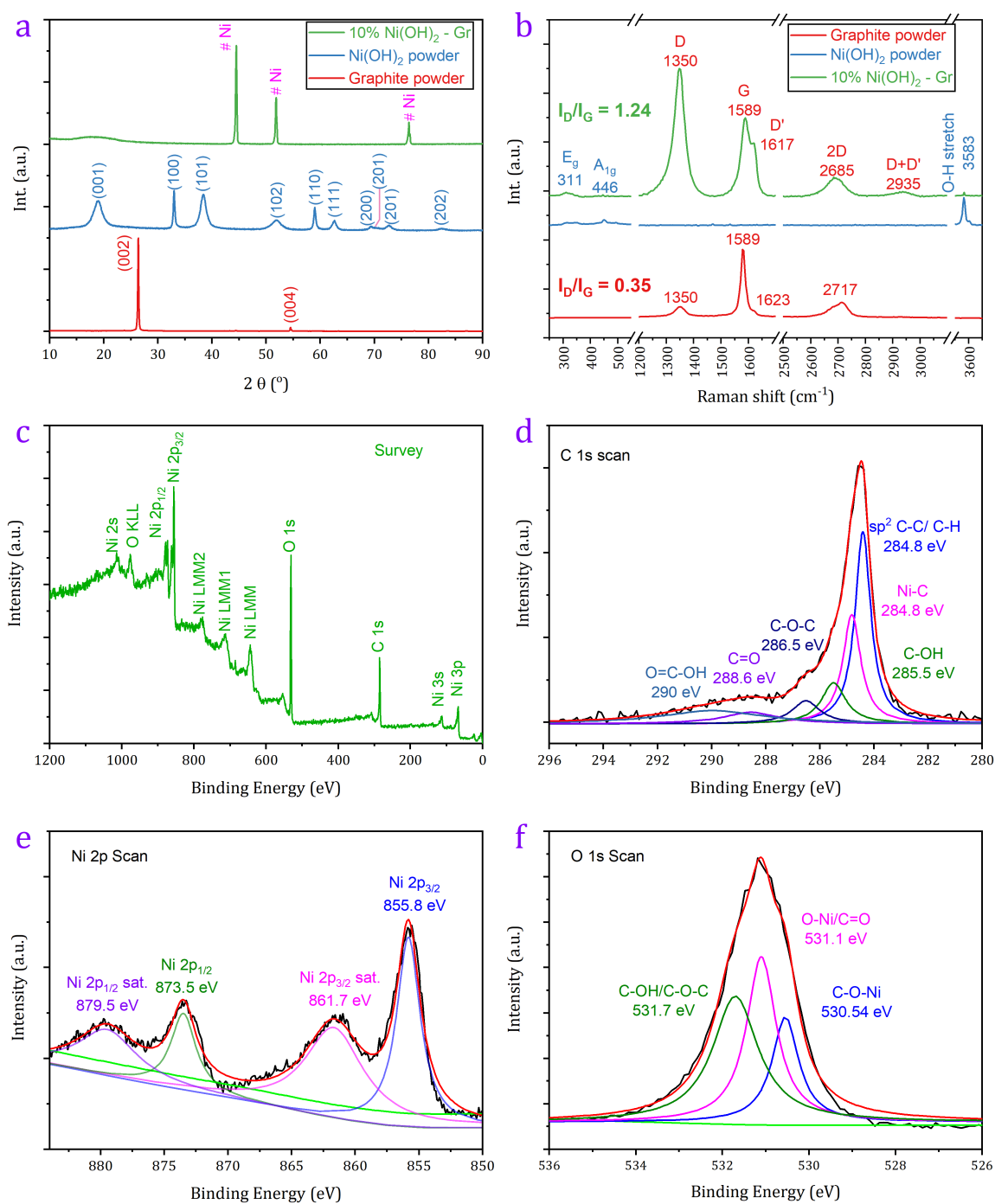
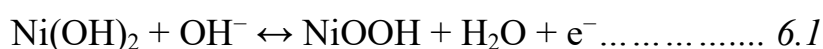


Figure 33 (a) XRD spectra, (b) Raman spectra of the graphite and Ni(OH)₂ powders and the 10% Ni(OH)₂-Gr deposited composite, (c) XPS survey scan, (d) high-resolution C 1s scan, (e) high-resolution Ni 2p scan, and (f) high-resolution O 1s scan.

The specific capacitance of the Ni(OH)₂-Gr hybrids with different Ni(OH)₂ content (0~100% by wt.) were compared at various current densities from 1 A g⁻¹

¹ to 20 A g⁻¹, as shown in Figure 34 (a). The calculated specific capacitances from galvanostatic charge-discharge (GCD) curves are shown in Table 12. The comparison indicated that the 10% content of Ni(OH)₂ in the hybrid electrode has the maximum specific capacitance since the value of the specific capacitance is decreased after that from 20%, then becomes a plateau region until 100% in wt. content of Ni(OH)₂.

Figure 34 (b) represents the CV curve of the 10% Ni(OH)₂-Gr hybrid electrode at different scan rates in 2 M KOH within a potential window of 0-0.6 V. A couple of redox peaks is clearly observed in the CV curves, indicating that the origin of the capacitance in the hybrid electrode is due the pseudocapacitive behavior. The redox peaks correspond to the reversible redox reaction Ni(OH)₂ ↔ nickel oxyhydroxide (NiOOH). The faradic reaction at the surface of the 10% Ni(OH)₂-Gr hybrid electrode is well-defined by the following equation:



By increasing the scan rate from 2 mV s⁻¹ to 100 mV s⁻¹, the position of the anodic peak is shifted to higher potential, and that of the cathodic peak is shifted to lower potential. This behavior is due to the internal resistance of the electrode that arises from the diffusion of the electrolyte ions within the electrode[252]. The specific capacitances, C_m (F g⁻¹), were estimated from the CV curves according to the equation

$$C_m = \int I dV / (v m V) \dots\dots\dots 6.2$$

where I is the response current, v denotes the scan rate, V is the potential, and m is the active material mass. The hybrid electrode demonstrates a specific capacitance of 2676 F g⁻¹ at 2 mV s⁻¹.

Figure 34 (c) shows the GCD curves of the 10% Ni(OH)₂-Gr hybrid electrode at different scan rates in 2 M KOH electrolyte. The GCD tests were

performed in a potential window of 0-0.4 V and at current densities from 1 A g⁻¹ to 20 A g⁻¹. The symmetric and non-linear behavior of the GCD curves further confirms the pseudocapacitance of the hybrid electrode. The specific capacitance of the hybrid electrode can be estimated from

$$C_m = I \Delta t / (m \Delta V) \dots\dots\dots 6.3$$

where I is the discharging current, Δt is the discharging time, m is the mass of active material, and ΔV is the discharging potential window. Figure 4 (d) shows the specific capacitance of the hybrid electrode. The 10% Ni(OH)₂-Gr hybrid electrode demonstrates a specific capacitance of 3408 F g⁻¹ at 1 A g⁻¹. This capacitance value is superior to previously reported values, as shown in Table 13. Furthermore, a high rate capability of 47% was obtained at a current density of 10 A g⁻¹. The high capacitance value of the 10% Ni(OH)₂-Gr hybrid electrode could be due to: (1) the synergistic effect between Ni(OH)₂ and the graphene nanoflakes; (2) the oxygen-containing functional groups in the Ni(OH)₂-Gr composite can provide extra capacitance, as well as improved wettability of the electrode, which can improve the interface layer formed between the electrolyte and the electrode surface[253, 254]. Figure 34 (d) shows the variation of the specific capacitances of the 10% Ni(OH)₂-Gr hybrid electrode as a function of scan rate and current density. The specific capacitance was decreased with increasing the scan rate (or the current density). The high specific capacitance observed at the low scan rate (low current density) may be due to the high accessibility of the electrolyte ions to the electrode surface during the faradic process. Meanwhile, the low accessibility of the electrolyte ions to the electrode surface leads to a slow faradic reaction at the high scan rate (high current density).

The cyclic stability is a very important parameter to evaluate the electrochemical performance of the electrode material. Figure 34 (e) presents the cyclic stability of the pure graphene and Ni(OH)₂ electrodes and the 10%

Ni(OH)₂-Gr hybrid electrode, which were further tested by repeating CV tests at a scan rate of 100 mV s⁻¹ for 3000 cycles. It is clear that the capacitance retention of the Ni(OH)₂-Gr hybrid electrode after 3000 cycles is 90.5%, which is much higher than the pure Ni(OH)₂ electrode with 63%. The excellent cyclic stability is ascribed to the good binding between the Ni(OH)₂ and the graphene nanoflakes as confirmed previously from XPS results. This good binding allows facile electron transport through Ni(OH)₂ to the graphene nanoflakes, and also enhances the electron transportation to the current collector. Subsequently, the ionic and electronic conductivities were improved.

Table 12 The calculated specific capacitance of the Ni(OH)₂-graphene hybrid electrodes deposited on nickel foam with different Ni(OH)₂ content (0~100% by wt.) from the GCD curves at different current densities from 1 A g⁻¹ to 20 A g⁻¹.

Current density (A g ⁻¹)	<i>Specific capacitance (F/g) for different Ni(OH)₂ contents (0~100% by wt.) from GCD curves</i>							
	0%	10%	20%	30%	40%	60%	80%	100%
1	1194.8	3407.8	1772.2	1761.7	1738.434	1565.73	1634.2	1750.4
2	1073.3	3030.6	1704.4	1688.6	1624.377	1239.93	1434.5	1540.6
5	924.36	2261.8	1286.7	1372.6	1190.16	576.855	787.86	1033.4
10	764.28	1627.6	936.48	1084	811.5795	185.094	273.65	615.37
15	668.15	1286.5	748.89	898.52	617.7522	78.894	109.11	436.15
20	576.19	1059.1	625.31	746.15	509.0196	37.3914	15.02	322.33

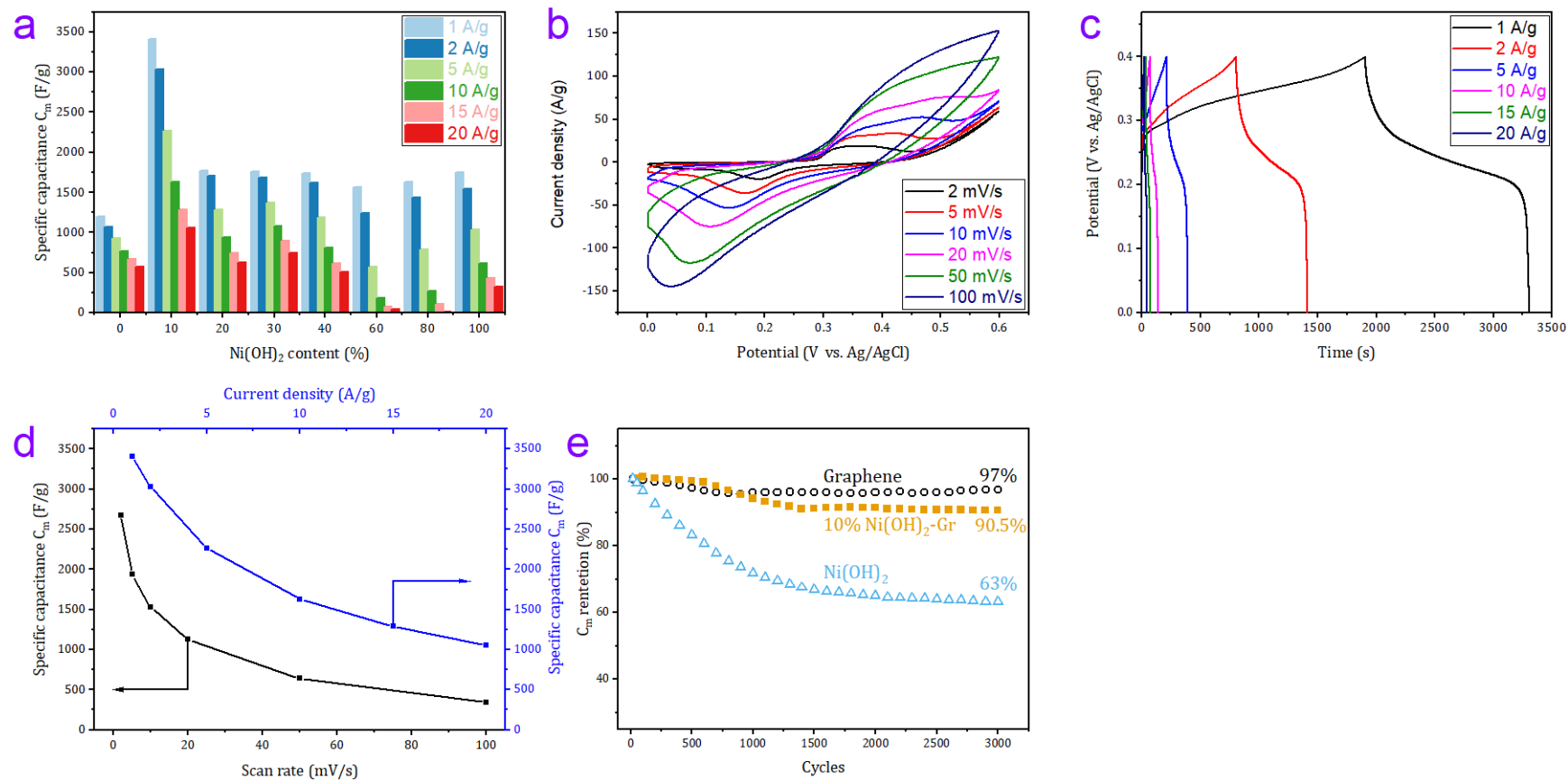


Figure 34 (a) comparison of specific capacitances of Ni(OH)₂-Gr hybrid electrodes with different Ni(OH)₂ content (0~100% by wt.) at various current densities of 1~20 A g⁻¹, (b) CV curves, (c) GCD curves, (d) the variation of specific capacitances of 10% Ni(OH)₂-Gr hybrid electrode as a function of scan rate and current density, and (e) cyclic stability of Gr, Ni(OH)₂, and the 10% Ni(OH)₂-Gr hybrid electrode at a scan rate of 100 mV s⁻¹.

Table 13 Specific capacitance of the Ni(OH)₂-Gr hybrid electrode obtained in this study, compared with some of the Ni(OH)₂ and carbon-based hybrid electrodes reported in previous literature.

<i>Material</i>	<i>Specific capacitance</i>	<i>Electrolyte</i>	<i>Retention</i>	<i>Ref.</i>
Ni(OH)₂-Gr	3408 F g ⁻¹ at 1 A g ⁻¹	2 M KOH	90.5% after 3000 cycles	This work
Ni(OH)₂/rGO	3328.7 F g ⁻¹ at 1.5 A g ⁻¹	1 M KOH	90.6% after 5000 cycles	[255]
rGO-Ni(OH)₂	1717 F g ⁻¹ at 0.5 A g ⁻¹	2 M KOH	89% after 1000 cycles	[256]
CNT@ Ni(OH)₂ core-shell	1136 F g ⁻¹ at 2 A g ⁻¹	1 M KOH	92% after 1000 cycles	[241]
Ni(OH)₂/G/NF	2161 F g ⁻¹ at 3 A g ⁻¹	1 M KOH	51% after 500 cycles	[257]
rGO/Ni(OH)₂	2134 F g ⁻¹ at 2 mV s ⁻¹	6 M KOH	81% after 2000 cycles	[248]
Ni(OH)₂-3D graphene	1450 F g ⁻¹ at 5 A g ⁻¹	6 M KOH	78% after 1000 cycles	[258]
Ni(OH)₂/graphene	1503 F g ⁻¹ at 2 mV s ⁻¹	6 M KOH	96.5% after 6000 cycles	[259]

6.3.2 Negative electrode material

Graphene is a promising electrode material for energy storage and conversion applications due to its large surface area, good stability, and excellent electrical conductivity[253]. Graphene can be prepared by the chemical reduction of graphene oxide (GO). GO was synthesized from raw graphite using Hummers' method[260]. Then, reduced graphene oxide (rGO) was produced by reducing the oxygen and carbonyl groups by hydrazine hydrate. The presence of the residual oxygen groups on the graphene sheets enhances the wettability of the electrodes, and also prevents aggregation of the graphene sheets. Furthermore, the residual oxygen groups on the graphene sheets present additional pseudocapacitance[261].

The XRD patterns of graphite, GO, and rGO are shown in Figure 35 (a). The diffraction peak at 26.4° corresponding to the graphite (002) plane no longer appears in GO. The peak corresponding to GO appears at 10.76° with an interlayer distance of 8.22 \AA . An increase in the interlayer distance is evidence of the formation of highly oxidized GO. After the reduction of GO, the XRD pattern of rGO clearly shows two diffraction peaks at 23.5° and 43° , related to the (002) and (100) planes of carbon, respectively. This confirms that the oxygen-containing functional groups vanished during the reduction by sodium borohydride and hydrazine hydrate. In Figure 35 (b), the Raman spectrum of rGO shows two main peaks, the D band (disordered carbon) at 1350 cm^{-1} and the G band (E_{2g} symmetry of sp^2 carbon) at 1589 cm^{-1} . The ratio between the intensities of the D and G bands (I_D/I_G) for GO was 0.96. However, the I_D/I_G ratio in the case of rGO was 1.11, indicating that GO was reduced to rGO with more structural defects.

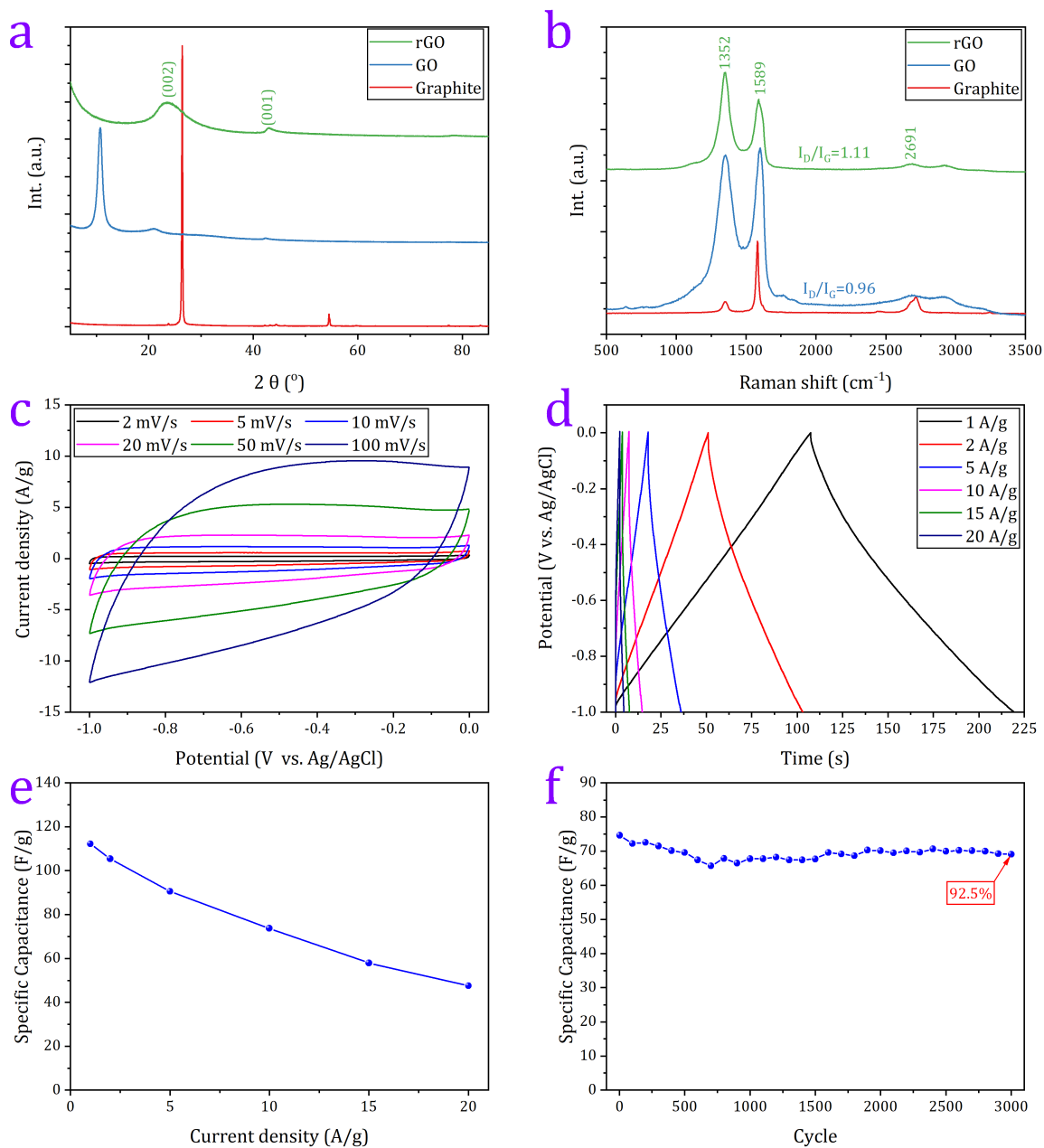


Figure 35 (a) XRD spectra, (b) Raman spectra of graphite, GO, and rGO, (c) CV curves at different scan rates, (d) GCD curves at different current densities, (e) specific capacitance versus current density, and (f) cycling stability for 3000 cycles at a current density of 10 A g^{-1} for the rGO electrode.

The electrochemical performance of rGO was tested by CV and GCD in 2 M KOH aqueous solution over the potential range of -1 V to 0 V. Figure 35 (c) displays the CV curves of rGO at different scan rates from 2 mV s^{-1} to

100 mV s⁻¹. The semi-rectangular shape suggested an excellent EDLC performance. The CV curves preserved the same shape with changing the scan rate, demonstrating outstanding cyclic stability. Figure 35 (d) shows the GCD curves of rGO at different current densities from 1 A g⁻¹ to 20 A g⁻¹. The GCD curves showed symmetrical and linear charging and discharging profiles, indicating that the rGO electrode had good reversibility and fast response. The specific capacitance of the rGO electrode was calculated from the GCD curves at different current densities, as shown in Figure 35 (e). The calculated specific capacitance was approximately 110 F g⁻¹ at a current density of 1 A g⁻¹. The stability of the rGO electrode was determined by repeating GCD for 3000 cycles at a current density of 10 A g⁻¹. As shown in Figure 35 (f), the rGO electrode retained 92.5% of its initial specific capacitance after 3000 cycles and exhibited excellent cyclic stability.

6.3.3 Asymmetric supercapacitor

The ASC was assembled using 10% Ni(OH)₂-Gr hybrid (as the positive electrode), rGO (as the negative electrode), and 2 M KOH aqueous electrolyte, as illustrated in Figure 36 (a). For ASC, it is known that the charge balance between the positive and negative electrodes should be satisfied by the relation $q_+ = q_-$. The charge stored by each electrode (q) can be determined by the specific capacitance (C), the potential window (ΔV), and the loading mass of the electrode (m). In order to obtain $q_+ = q_-$, the mass balance will follow the following expression:

$$\frac{m_+}{m_-} = \frac{C_- \times \Delta V_-}{C_+ \times \Delta V_+} \dots\dots\dots 6.4$$

Herein, the optimum mass ratio between the 10% Ni(OH)₂-Gr hybrid and rGO electrodes was predicted to be 1:10.

Figure 36 (b) illustrates the CV curves of the Ni(OH)₂-Gr//rGO ASC at different scan rates in the potential window from 0 V to 1.6 V. The broad redox peaks in the CV curves suggest that the pseudocapacitive behavior of the Ni(OH)₂-Gr//rGO ASC arises from the 10% Ni(OH)₂-Gr hybrid electrode. Figure 36 (c) shows the GCD curves at various current densities ranging from 2 mA cm⁻² to 20 mA cm⁻². A small IR drop is observed in the discharge curves, indicating the small equivalent series resistance of the ASC. From the discharge curves, the specific capacitance values of the Ni(OH)₂-Gr//rGO ASC are estimated based on the loading mass of the active materials on the two electrodes. The specific capacitance reaches a maximum of 180 F g⁻¹ at 1 mA cm⁻² in the 1.6 V potential window, as shown in Figure 36 (d). The energy and power density of the ASC is the most important parameter for evaluating its performance. Figure 36 (e) represents the Ragone plot of the energy density and power density. The energy density of the Ni(OH)₂-Gr//rGO ASC achieves 64 W h kg⁻¹ at a power density of 411 W kg⁻¹ and holds 20 W h kg⁻¹ at a high-power density of 8230 W kg⁻¹. The results show outstanding performance compared with literature results of CNT@Ni(OH)₂//3DGN (44 W h kg⁻¹ at 800 W kg⁻¹)[241], β-Ni(OH)₂/NF//AC (36.2 W h kg⁻¹ at 100.6 W kg⁻¹)[262], Ni(OH)₂/NF//AC (35.7 W h kg⁻¹ at 490 W kg⁻¹)[263], Ni(OH)₂/CNT/NF//AC (50.6 W h kg⁻¹ at 96 W kg⁻¹)[264], Ni/Ni(OH)₂//AC (23 W h kg⁻¹ at 4598 W kg⁻¹)[228], and α-Ni(OH)₂/NF//AC (74.94 W h kg⁻¹ at 197.4 W kg⁻¹)[265].

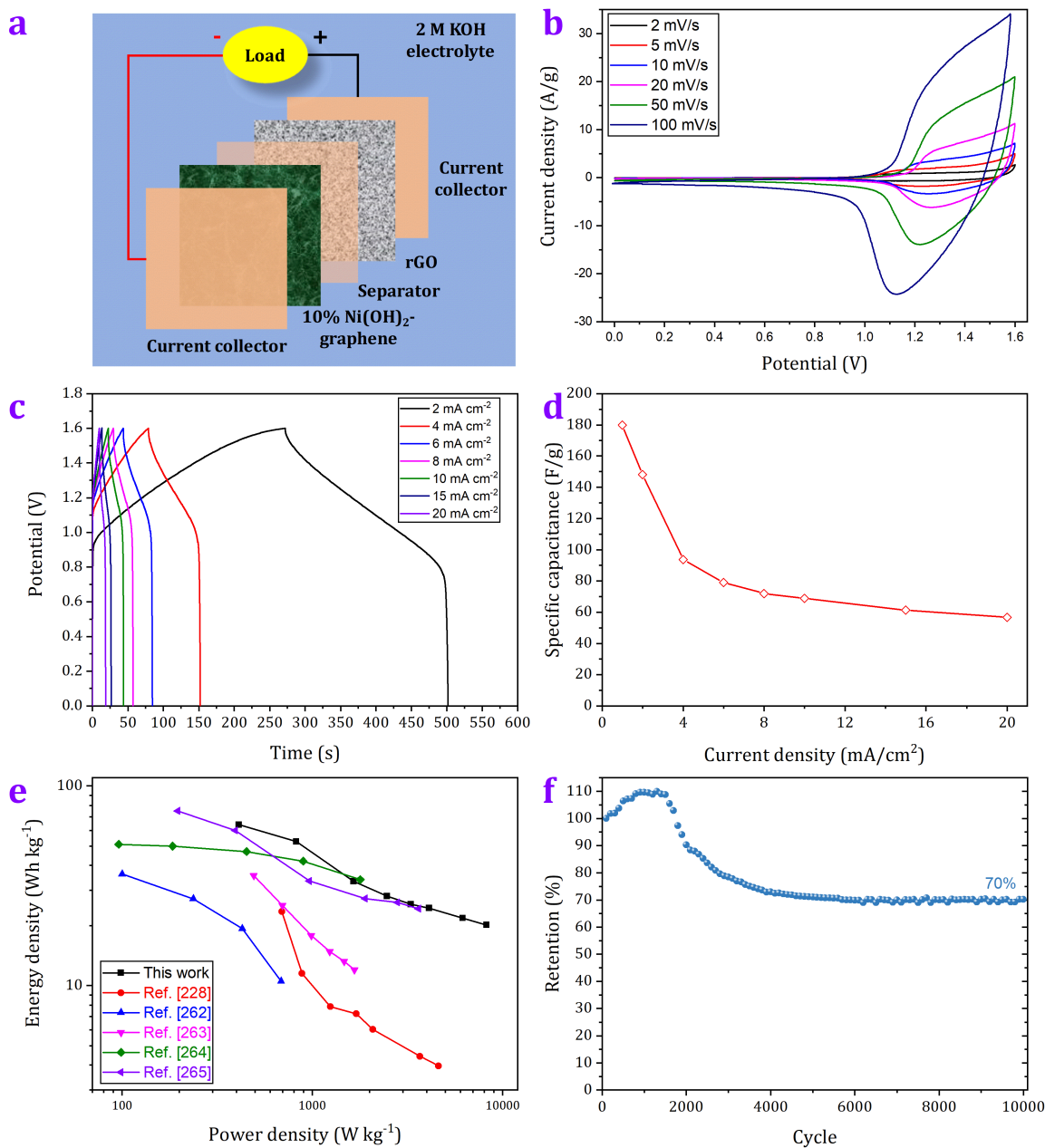


Figure 36 (a) Schematic diagram of the Ni(OH)₂-Gr//rGO ASC, (b) CV curves of the Ni(OH)₂-Gr//rGO ASC at various scan rates, (c) GCD curves of the Ni(OH)₂-Gr//rGO ASC at various current densities, (d) specific capacitance of the Ni(OH)₂-Gr//rGO ASC at different current densities, (e) Ragone plot of the Ni(OH)₂-Gr//rGO ASC, and (f) cyclic stability of the Ni(OH)₂-Gr//rGO ASC at 6 mA cm⁻² current density.

The cyclic stability of Ni(OH)₂-Gr//rGO ASC was investigated by repeating charge-discharge cycles at a current density of 6 mA cm⁻². As shown in Figure 36

(f), the Ni(OH)₂-Gr//rGO ASC exhibits a capacitance retention of 70% after 10,000 cycles, indicating acceptable cyclic stability that is superior to some pervious ASCs, such as β-Ni(OH)₂/NF//AC (92% retention after 1000 cycles)[262], Ni(OH)₂/CNT/NF//AC (83% retention after 3000 cycles)[264], and Co₃O₄/CC//MnO₂/CC (83% retention after 5000 cycles)[266].

6.4 Summary

A Ni(OH)₂-Gr hybrid electrode was successfully deposited directly on nickel foam by the facile, one-step NPDS technique. The electrochemical performance of the 10% Ni(OH)₂-Gr hybrid electrode demonstrated a specific capacitance of 3400 F g⁻¹ at 1 A g⁻¹ in 2 M KOH. An asymmetric supercapacitor has been fabricated using 10% Ni(OH)₂-Gr as a positive electrode and rGO as a negative electrode. The fabricated Ni(OH)₂-Gr//rGO ASC exhibits many advantages, such as a high specific capacitance of 180 F g⁻¹ at 1 mA cm⁻², wide potential window of 1.6 V, superior energy density of 64 W h kg⁻¹, high power density of 8230 W kg⁻¹, and acceptable cyclic stability of 70% capacitance retention after 10,000 cycles. This indicates that Ni(OH)₂-Gr//rGO ASC may offer a great prospective for energy storage applications.

Chapter 7

Conclusion

7.1 Conclusion

This thesis has focused on the development of one-step, facile deposition technique of different electrode materials, namely few-layer graphene nano-flakes electrode, MoS₂-graphite hybrid electrode, Ni(OH)₂ electrode, and Ni(OH)₂-graphene hybrid electrode.

Improving the Electrochemical performance of each of these electrode materials, we have studied the effects of different key parameters, such as the deposition scan speed of the few-layer graphene nano-flakes electrode, the concentration of the electrolyte used few-layer graphene nano-flakes symmetric device, the amount of MoS₂ used in hybrid MoS₂-graphite electrode, the effect of deposition parameters on Ni(OH)₂ electrode, and the effect of the amount of Ni(OH)₂ used in hybrid Ni(OH)₂-graphene electrode on their performance as electrodes and the overall electrochemical performance of devices. The electrochemical performances are compared in Table 14 and the key findings in each chapter are summarized below:

- (1) Few-layer graphene nano-flakes have been deposited by the NPDS on a stainless-steel substrate. The deposition was carried out with different scan speeds of deposition. The deposition with slow scan speed results in graphene/graphite structure. By increasing the scan speed of the deposition, the micro-sized graphite powder was totally transformed to few-layered graphene nano-flakes. The obtained few-layer graphene nano-flakes showed high areal capacitance in symmetric two electrode configuration. The areal capacitance of the symmetric few-layer graphene nano-flakes supercapacitor could be improved by increasing the concentration of the acidic ions in the gel electrolyte.
- (2) The MoS₂-graphite hybrid electrode was prepared firstly by the ball milling by mixing the raw MoS₂ and graphite powders with different MoS₂

contents. Then the NPDS was used to deposit MoS₂-graphite hybrids on stainless-steel substrate. The electrochemical performance of symmetrical supercapacitors fabricated from MoS₂-graphite hybrid showed better performance at 15% of the MoS₂-graphite composition ratio. Moreover, the cyclic stability of the supercapacitor is measured by repeating charging-discharging for 10,000 cycles.

- (3) Nano-structured Ni(OH)₂ was successfully prepared by the deposition of micro-sized Ni(OH)₂ powder on nickel sheet and nickel foam using the NPDS. The deposition of the Ni(OH)₂ powder on nickel sheets was carried out with various stand-off-distances (SoDs) and carrier gas pressures. The crystallite size of the nano-structured Ni(OH)₂ depends on the SoD and the carrier gas pressure. The electrochemical performance of Ni(OH)₂ deposited on nickel sheets showed that the deposition with 5 mm SoD and 0.3 MPa carrier gas pressure is the optimum deposition condition for the nano-structured Ni(OH)₂ thin film as an electrode material. The nano-structured Ni(OH)₂ thin film deposited with 5 mm SoD and 0.3 MPa carrier gas pressure on nickel foam demonstrates a specific capacitance of 2377 F g⁻¹ at 2 mV s⁻¹ scan rate and 2092 F g⁻¹ at 1 A g⁻¹ current density and excellent cyclic stability for 3000 cycles with 83% capacitance retention.
- (4) Nickel hydroxide-graphene (Ni(OH)₂-Gr) hybrid electrode was prepared by one-step, binder-free NPDS deposition technique from a micro-sized hydroxide graphite powders mixture with Ni(OH)₂ weight ratios. The electrochemical performance of the 10% Ni(OH)₂-Gr hybrid electrode in a 3-electrode cell demonstrates a specific capacitance of 3400 F g⁻¹ at 1 A g⁻¹. Asymmetric supercapacitors (ASCs) was fabricated from Ni(OH)₂-Gr hybrid as a positive electrode and reduced graphene oxide (rGO) as a negative electrode. The Ni(OH)₂-Gr//rGO ASC displays a specific capacitance of 180 F g⁻¹ at 1 mA cm⁻² in a high potential window from 0 V to 1.6 V. The Ni(OH)₂-Gr//rGO ASC has an energy density of 64 W h kg⁻¹

¹ at a power density of 411 W kg⁻¹, and still 20 W h kg⁻¹ at a high power density of 8230 W kg⁻¹.

Table 14 Summary of the electrochemical performance of the studied 3-electrode configuration and the fabricated symmetric and asymmetric hybrid supercapacitors.

Material	3-electrode		2-electrode					
	Capacitance	Stability	Anode Materials	Capacitance	Stability	Potential window	Max. Energy Density	Max. Power Density
few-layer graphene nano-flakes	-	-	Symmetric	1.67 mF cm ⁻² @ 2 mV s ⁻¹	93% after 5000 cycles	1 V	-	-
MoS ₂ -graphite	-	-	Symmetric	5.1 mF cm ⁻² @ 2 mV s ⁻¹	81% after 10,000 cycles	1 V	-	-
Ni(OH) ₂	2092 F g ⁻¹ @ 1 A g ⁻¹	83% after 3000 cycles	-	-	-	-	-	-
Ni(OH) ₂ -graphene	3400 F g ⁻¹ @ 1 A g ⁻¹	90.5% after 3000 cycles	rGO	180 F g ⁻¹ @ 1 mA cm ⁻²	70% after 10,000 cycles	1.6 V	64 Wh kg ⁻¹	8.23 kW kg ⁻¹

7.2 Recommendations

Supercapacitors represent one of the key elements in energy storage systems having the potential to complement or even replace batteries in a variety of applications. The supercapacitor market is driven by their unique electrochemical characteristics such as high-power density, extremely short charging time, and excellent low-temperature performance. Given the rapid improvements of this technology, asymmetric supercapacitors are expected to play a key role in the energy-storage industry. The future of asymmetric supercapacitors looks promising with opportunities in transportation, power tools, and consumer electronics. Research in this area can be expected to flourish with the goal of increasing energy density without compromising the high-power density of supercapacitors. The combination of different Faradaic active and capacitive materials should be a viable approach, but a deeper understanding of the synergistic interactions is still required to ensure optimized capacitive performance.

Searching for new materials is essential to develop advanced asymmetric supercapacitors with enhanced electrochemical performance. In the past few years new 2D materials such as MXenes, metal nitrides, metal organic frameworks (MOFs), covalent organic framework (COFs), black phosphorus, and transition-metal dichalcogenides have been examined for their potential for high energy density systems. The use of these redox-active electrodes coupled with controllable pore structures offers a great opportunity to create optimized asymmetric supercapacitors. In addition, the selection of positive and negative electrode materials should be optimized to extend the operating voltage of the final device.

Finally, further study of the exact energy storage mechanisms for new composite materials is needed including computational studies on the effect of pore size on the double layer capacitance. Detailed computational modeling

tools at the molecular level need to be used to obtain better understanding of the charging-discharging mechanisms, self-discharging and capacitance development.

References

- [1] G. Wang, L. Zhang, J. Zhang, A review of electrode materials for electrochemical supercapacitors, *Chem Soc Rev*, 41 (2012) 797-828.
- [2] M. Armand, J.M. Tarascon, Building better batteries, *Nature*, 451 (2008) 652-657.
- [3] H. Wu, G. Yu, L. Pan, N. Liu, M.T. McDowell, Z. Bao, Y. Cui, Stable Li-ion battery anodes by in-situ polymerization of conducting hydrogel to conformally coat silicon nanoparticles, *Nat Commun*, 4 (2013) 1943.
- [4] C.M. Park, J.H. Kim, H. Kim, H.J. Sohn, Li-alloy based anode materials for Li secondary batteries, *Chem Soc Rev*, 39 (2010) 3115-3141.
- [5] J.R. Miller, P. Simon, Materials science. Electrochemical capacitors for energy management, *Science*, 321 (2008) 651-652.
- [6] P. Simon, Y. Gogotsi, Materials for electrochemical capacitors, *Nat Mater*, 7 (2008) 845-854.
- [7] A. Burke, Ultracapacitors: why, how, and where is the technology, *Journal of Power Sources*, 91 (2000) 37-50.
- [8] R. Kotz, M. Carlen, Principles and applications of electrochemical capacitors, *Electrochimica Acta*, 45 (2000) 2483-2498.
- [9] W. Henson, Optimal battery/ultracapacitor storage combination, *Journal of Power Sources*, 179 (2008) 417-423.
- [10] P. Bubna, S.G. Advani, A.K. Prasad, Integration of batteries with ultracapacitors for a fuel cell hybrid transit bus, *Journal of Power Sources*, 199 (2012) 360-366.

- [11] L.L. Zhang, X.S. Zhao, Carbon-based materials as supercapacitor electrodes, *Chem Soc Rev*, 38 (2009) 2520-2531.
- [12] H. Helmholtz, Studien über electriche Grenzschichten, *Annalen der Physik und Chemie*, 243 (1879) 337-382.
- [13] M. Gouy, Sur la constitution de la charge électrique à la surface d'un électrolyte, *J. Phys. Theor. Appl.*, 9 (1910) 457-468.
- [14] D.L. Chapman, LI. A contribution to the theory of electrocapillarity, *The London, Edinburgh, and Dublin Philosophical Magazine and Journal of Science*, 25 (2010) 475-481.
- [15] O. Stern, ZUR THEORIE DER ELEKTROLYTISCHEN DOPPELSCHICHT, *Zeitschrift für Elektrochemie und angewandte physikalische Chemie*, 30 (1924) 508-516.
- [16] C. Liu, Z. Yu, D. Neff, A. Zhamu, B.Z. Jang, Graphene-based supercapacitor with an ultrahigh energy density, *Nano Lett*, 10 (2010) 4863-4868.
- [17] B.E. Conway, Transition from Supercapacitor to Battery Behavior in Electrochemical Energy-Storage, *Journal of the Electrochemical Society*, 138 (1991) 1539-1548.
- [18] B.E. Conway, V. Birss, J. Wojtowicz, The role and utilization of pseudocapacitance for energy storage by supercapacitors, *Journal of Power Sources*, 66 (1997) 1-14.
- [19] A. Burke, R&D considerations for the performance and application of electrochemical capacitors, *Electrochimica Acta*, 53 (2007) 1083-1091.
- [20] K. Naoi, P. Simon, *New Materials and New Configurations for Advanced Electrochemical Capacitors*, 2008.

- [21] E. Frackowiak, V. Khomenko, K. Jurewicz, K. Lota, F. Beguin, Supercapacitors based on conducting polymers/nanotubes composites, *Journal of Power Sources*, 153 (2006) 413-418.
- [22] K. Jurewicz, S. Delpeux, V. Bertagna, F. Beguin, E. Frackowiak, Supercapacitors from nanotubes/polypyrrole composites, *Chemical Physics Letters*, 347 (2001) 36-40.
- [23] C. Arbizzani, M. Mastragostino, F. Soavi, New trends in electrochemical supercapacitors, *Journal of Power Sources*, 100 (2001) 164-170.
- [24] A. Laforgue, P. Simon, J.F. Fauvarque, M. Mastragostino, F. Soavi, J.F. Sarrau, P. Lailier, M. Conte, E. Rossi, S. Saguatti, Activated carbon/conducting polymer hybrid supercapacitors, *Journal of the Electrochemical Society*, 150 (2003) A645-A651.
- [25] M. Mastragostino, C. Arbizzani, F. Soavi, Conducting polymers as electrode materials in supercapacitors, *Solid State Ionics*, 148 (2002) 493-498.
- [26] H. Li, L. Cheng, Y. Xia, A Hybrid Electrochemical Supercapacitor Based on a 5 V Li-Ion Battery Cathode and Active Carbon, *Electrochemical and Solid-State Letters*, 8 (2005) A433-A436.
- [27] X. Wang, J.P. Zheng, The optimal energy density of electrochemical capacitors using two different electrodes, *Journal of the Electrochemical Society*, 151 (2004) A1683-A1689.
- [28] A. Du Pasquier, I. Plitz, S. Menocal, G. Amatucci, A comparative study of Li-ion battery, supercapacitor and nonaqueous asymmetric hybrid devices for automotive applications, *Journal of Power Sources*, 115 (2003) 171-178.

- [29] W.G. Pell, B.E. Conway, Peculiarities and requirements of asymmetric capacitor devices based on combination of capacitor and battery-type electrodes, *Journal of Power Sources*, 136 (2004) 334-345.
- [30] G.G. Amatucci, F. Badway, A. Du Pasquier, T. Zheng, An asymmetric hybrid nonaqueous energy storage cell, *Journal of the Electrochemical Society*, 148 (2001) A930-A939.
- [31] W.T. Gu, G. Yushin, Review of nanostructured carbon materials for electrochemical capacitor applications: advantages and limitations of activated carbon, carbide-derived carbon, zeolite-templated carbon, carbon aerogels, carbon nanotubes, onion-like carbon, and graphene, *Wiley Interdisciplinary Reviews-Energy and Environment*, 3 (2014) 424-473.
- [32] D.Y. Qu, H. Shi, Studies of activated carbons used in double-layer capacitors, *Journal of Power Sources*, 74 (1998) 99-107.
- [33] J. Gamby, P.L. Taberna, P. Simon, J.F. Fauvarque, M. Chesneau, Studies and characterisations of various activated carbons used for carbon/carbon supercapacitors, *Journal of Power Sources*, 101 (2001) 109-116.
- [34] H. Shi, Activated carbons and double layer capacitance, *Electrochimica Acta*, 41 (1996) 1633-1639.
- [35] Y.M. Cai, Z.Y. Qin, L. Chen, Effect of electrolytes on electrochemical properties of graphene sheet covered with polypyrrole thin layer, *Progress in Natural Science-Materials International*, 21 (2011) 460-466.
- [36] Q. Cheng, J. Tang, J. Ma, H. Zhang, N. Shinya, L.C. Qin, Graphene and carbon nanotube composite electrodes for supercapacitors with ultra-high energy density, *Phys Chem Chem Phys*, 13 (2011) 17615-17624.

- [37] E. Frackowiak, F. Beguin, Carbon Materials for the Electrochemical Storage of Energy in Capacitors, 2001.
- [38] E. Frackowiak, K. Metenier, V. Bertagna, F. Beguin, Supercapacitor electrodes from multiwalled carbon nanotubes, Applied Physics Letters, 77 (2000) 2421-2423.
- [39] C.M. Niu, E.K. Sichel, R. Hoch, D. Moy, H. Tennent, High power electrochemical capacitors based on carbon nanotube electrodes, Applied Physics Letters, 70 (1997) 1480-1482.
- [40] K.H. An, W.S. Kim, Y.S. Park, Y.C. Choi, S.M. Lee, D.C. Chung, D.J. Bae, S.C. Lim, Y.H. Lee, Supercapacitors Using Single-Walled Carbon Nanotube Electrodes, Advanced Materials, 13 (2001) 497-500.
- [41] K.H. An, W.S. Kim, Y.S. Park, J.M. Moon, D.J. Bae, S.C. Lim, Y.S. Lee, Y.H. Lee, Electrochemical properties of high-power supercapacitors using single-walled carbon nanotube electrodes, Advanced Functional Materials, 11 (2001) 387-392.
- [42] A.K. Geim, K.S. Novoselov, The rise of graphene, Nat Mater, 6 (2007) 183-191.
- [43] A.K. Geim, Graphene: status and prospects, Science, 324 (2009) 1530-1534.
- [44] K.S. Novoselov, A.K. Geim, S.V. Morozov, D. Jiang, M.I. Katsnelson, I.V. Grigorieva, S.V. Dubonos, A.A. Firsov, Two-dimensional gas of massless Dirac fermions in graphene, Nature, 438 (2005) 197-200.
- [45] A. Peigney, C. Laurent, E. Flahaut, R.R. Bacsa, A. Rousset, Specific surface area of carbon nanotubes and bundles of carbon nanotubes, Carbon, 39 (2001) 507-514.

- [46] K.S. Novoselov, A.K. Geim, S.V. Morozov, D. Jiang, Y. Zhang, S.V. Dubonos, I.V. Grigorieva, A.A. Firsov, Electric field effect in atomically thin carbon films, *Science*, 306 (2004) 666-669.
- [47] K.S. Kim, Y. Zhao, H. Jang, S.Y. Lee, J.M. Kim, K.S. Kim, J.H. Ahn, P. Kim, J.Y. Choi, B.H. Hong, Large-scale pattern growth of graphene films for stretchable transparent electrodes, *Nature*, 457 (2009) 706-710.
- [48] K.H. Yu, W. Zhao, X. Wu, J.N. Zhuang, X.H. Hu, Q.B. Zhang, J. Sun, T. Xu, Y. Chai, F. Ding, L.T. Sun, In situ atomic-scale observation of monolayer graphene growth from SiC, *Nano Research*, 11 (2018) 2809-2820.
- [49] D.V. Kosynkin, A.L. Higginbotham, A. Sinitskii, J.R. Lomeda, A. Dimiev, B.K. Price, J.M. Tour, Longitudinal unzipping of carbon nanotubes to form graphene nanoribbons, *Nature*, 458 (2009) 872-876.
- [50] M.D. Stoller, S. Park, Y. Zhu, J. An, R.S. Ruoff, Graphene-based ultracapacitors, *Nano Lett*, 8 (2008) 3498-3502.
- [51] C.D. Lokhande, D.P. Dubal, O.S. Joo, Metal oxide thin film based supercapacitors, *Current Applied Physics*, 11 (2011) 255-270.
- [52] W. Wang, S. Guo, I. Lee, K. Ahmed, J. Zhong, Z. Favors, F. Zaera, M. Ozkan, C.S. Ozkan, Hydrous ruthenium oxide nanoparticles anchored to graphene and carbon nanotube hybrid foam for supercapacitors, *Sci Rep*, 4 (2014) 4452.
- [53] D.Y. Qu, Studies of the activated carbons used in double-layer supercapacitors, *Journal of Power Sources*, 109 (2002) 403-411.
- [54] J.R. Lomeda, C.D. Doyle, D.V. Kosynkin, W.F. Hwang, J.M. Tour, Diazonium functionalization of surfactant-wrapped chemically converted graphene sheets, *J Am Chem Soc*, 130 (2008) 16201-16206.

- [55] S. Stankovich, D.A. Dikin, G.H. Dommett, K.M. Kohlhaas, E.J. Zimney, E.A. Stach, R.D. Piner, S.T. Nguyen, R.S. Ruoff, Graphene-based composite materials, *Nature*, 442 (2006) 282-286.
- [56] B.E. Conway, *Electrochemical Supercapacitors: Scientific Fundamentals and Technological Applications*, Springer US2013.
- [57] Y. Chen, X.O. Zhang, D.C. Zhang, P. Yu, Y.W. Ma, High performance supercapacitors based on reduced graphene oxide in aqueous and ionic liquid electrolytes, *Carbon*, 49 (2011) 573-580.
- [58] A. Balducci, R. Dugas, P.L. Taberna, P. Simon, D. Plee, M. Mastragostino, S. Passerini, High temperature carbon-carbon supercapacitor using ionic liquid as electrolyte, *Journal of Power Sources*, 165 (2007) 922-927.
- [59] H. Xia, M.O. Lai, L. Lu, Nanostructured Manganese Oxide Thin Films as Electrode Material for Supercapacitors, *Jom*, 63 (2011) 54-59.
- [60] W. Lee, R.S. Mane, V.V. Todkar, S. Lee, O. Egorova, W.S. Chae, S.H. Han, Implication of liquid-phase deposited amorphous RuO₂ electrode for electrochemical supercapacitor, *Electrochemical and Solid State Letters*, 10 (2007) A225-A227.
- [61] X.H. Zou, S. Zhang, M.H. Shi, J.L. Kong, Remarkably enhanced capacitance of ordered polyaniline nanowires tailored by stepwise electrochemical deposition, *Journal of Solid State Electrochemistry*, 11 (2007) 317-322.
- [62] B. Moore, E. Asadi, G. Lewis, *Deposition Methods for Microstructured and Nanostructured Coatings on Metallic Bone Implants: A Review*, *Advances in Materials Science and Engineering*, 2017 (2017) 9.

- [63] H. Khallaf, G.Y. Chai, O. Lupan, H. Heinrich, S. Park, A. Schulte, L. Chow, Investigation of chemical bath deposition of ZnO thin films using six different complexing agents, *Journal of Physics D-Applied Physics*, 42 (2009) 135304.
- [64] P.R. Deshmukh, N. Pusawale, V.S. Jamadade, U.M. Patil, C.D. Lokhande, Microwave assisted chemical bath deposited polyaniline films for supercapacitor application, *Journal of Alloys and Compounds*, 509 (2011) 5064-5069.
- [65] K.M. McPeak, M.A. Becker, N.G. Britton, H. Majidi, B.A. Bunker, J.B. Baxter, In Situ X-ray Absorption Near-Edge Structure Spectroscopy of ZnO Nanowire Growth During Chemical Bath Deposition, *Chemistry of Materials*, 22 (2010) 6162-6170.
- [66] P.K. Nair, V.M. Garcia, O. Gomez-Daza, M.T.S. Nair, High thin-film yield achieved at small substrate separation in chemical bath deposition of semiconductor thin films, *Semiconductor Science and Technology*, 16 (2001) 855-863.
- [67] A. Leela Mohana Reddy, F. Estaline Amitha, I. Jafri, S. Ramaprabhu, Asymmetric Flexible Supercapacitor Stack, *Nanoscale Research Letters*, 3 (2008) 145-151.
- [68] X. Cao, Y. Shi, W. Shi, G. Lu, X. Huang, Q. Yan, Q. Zhang, H. Zhang, Preparation of novel 3D graphene networks for supercapacitor applications, *Small*, 7 (2011) 3163-3168.
- [69] D. Hulicova-Jurcakova, X. Li, Z.H. Zhu, R. de Marco, G.Q. Lu, Graphitic Carbon Nanofibers Synthesized by the Chemical Vapor Deposition (CVD) Method and Their Electrochemical Performances in Supercapacitors, *Energy & Fuels*, 22 (2008) 4139-4145.
- [70] D. W. Johnson Jr, *Sol-Gel Processing of Ceramics and Glass*, 1985.

- [71] M. Gaudon, C. Laberty-Robert, F. Ansart, P. Stevens, Thick YSZ films prepared via a modified sol-gel route: Thickness control (8–80 μ m), *Journal of the European Ceramic Society*, 26 (2006) 3153-3160.
- [72] P. Lenormand, M. Rieu, P. Cienfuegos, A. Julbe, S. Castillo, F. Ansart, "Potentialities of the sol-gel route to develop cathode and electrolyte thick layers. Application to SOFC systems surface and coatings technology", 2008.
- [73] N.X.P. Vo, S.P. Yoon, S.W. Nam, J.H. Han, T.H. Lim, S.A. Hong, Fabrication of an Anode-Supported Sofc with a Sol-Gel Coating Method for a Mixed-Gas Fuel Cell, *Key Engineering Materials*, 277-279 (2005) 455-461.
- [74] C. Moreno-Castilla, F.J. Maldonado-Hodar, Carbon aerogels for catalysis applications: An overview, *Carbon*, 43 (2005) 455-465.
- [75] C. Lin, J.A. Ritter, B.N. Popov, Development of carbon-metal oxide supercapacitors from sol-gel derived carbon-ruthenium xerogels, *Journal of the Electrochemical Society*, 146 (1999) 3155-3160.
- [76] N.L. Wu, Nanocrystalline oxide supercapacitors, *Materials Chemistry and Physics*, 75 (2002) 6-11.
- [77] J.R. Zhang, D.C. Jiang, B. Chen, J.J. Zhu, L.P. Jiang, H.Q. Fang, Preparation and electrochemistry of hydrous ruthenium oxide/active carbon electrode materials for supercapacitor, *Journal of the Electrochemical Society*, 148 (2001) A1362-A1367.
- [78] R.N. Reddy, R.G. Reddy, Synthesis and electrochemical characterization of amorphous MnO₂ electrochemical capacitor electrode material, *Journal of Power Sources*, 132 (2004) 315-320.

- [79] D.M. Chun, M.H. Kim, J.C. Lee, S.H. Ahn, TiO₂ coating on metal and polymer substrates by nano-particle deposition system (NPDS), *Cirp Annals-Manufacturing Technology*, 57 (2008) 551-554.
- [80] D.-M. Chun, M.-H. Kim, J.-C. Lee, S.-H. Ahn, A Nano-particle Deposition System for Ceramic and Metal Coating at Room Temperature and Low Vacuum Conditions TT, *International Journal of Precision Engineering and Manufacturing*, 9 (2008) 51-53.
- [81] D.M. Chun, J.O. Choi, C.S. Lee, I. Kanno, H. Kotera, S.H. Ahn, Nano-particle deposition system (NPDS): Low energy solvent-free dry spray process for direct patterning of metals and ceramics at room temperature, *International Journal of Precision Engineering and Manufacturing*, 13 (2012) 1107-1112.
- [82] M.S. Kim, D.M. Chun, J.O. Choi, J.C. Lee, K.S. Kim, Y.H. Kim, C.S. Lee, S.H. Ahn, Room Temperature Deposition of TiO₂ Using Nano Particle Deposition System (NPDS): Application to Dye-Sensitized Solar Cell (DSSC), *International Journal of Precision Engineering and Manufacturing*, 12 (2011) 749-752.
- [83] S.I. Park, S. Kim, J.O. Choi, J.H. Song, M. Taya, S.H. Ahn, Low-cost fabrication of WO₃ films using a room temperature and low-vacuum air-spray based deposition system for inorganic electrochromic device applications, *Thin Solid Films*, 589 (2015) 412-418.
- [84] K. Jung, W. Song, D.M. Chun, J.C. Yeo, M.S. Kim, S.H. Ahn, C.S. Lee, Coating of Ni powders through micronozzle in a nano particle deposition system, *Metals and Materials International*, 16 (2010) 465-467.

- [85] 천두만, Development of nano particle deposition system(NPDS) for room temperature deposition of metals and ceramics and its applications, 서울대학교 대학원, pp. xii, 133 leaves.
- [86] S.H. Ahn, D.M. Chun, C.S. Kim, Nanoscale hybrid manufacturing process by nano particle deposition system (NPDS) and focused ion beam (FIB), *Cirp Annals-Manufacturing Technology*, 60 (2011) 583-586.
- [87] S.H. Ahn, J.O. Choi, C.S. Kim, G.Y. Lee, H.T. Lee, K. Cho, D.M. Chun, C.S. Lee, Laser-assisted nano particle deposition system and its application for dye sensitized solar cell fabrication, *Cirp Annals-Manufacturing Technology*, 61 (2012) 575-578.
- [88] D.M. Chun, M.S. Kim, J.C. Yeo, M.H. Kim, C.S. Lee, S.H. Ahn, Nano/micro particle beam for ceramic deposition and mechanical etching, *Physica Scripta*, T139 (2010) 014047.
- [89] D.-M. Chun, J.-O. Choi, C.S. Lee, S.-H. Ahn, Effect of stand-off distance for cold gas spraying of fine ceramic particles ($<5\mu\text{m}$) under low vacuum and room temperature using nano-particle deposition system (NPDS), *Surface and Coatings Technology*, 206 (2012) 2125-2132.
- [90] H. Kim, S. Yang, S.H. Ahn, C.S. Lee, Effect of particle size on various substrates for deposition of NiO film via nanoparticle deposition system, *Thin Solid Films*, 600 (2016) 109-118.
- [91] M.N.E.A.A. Nasim, D.-M. Chun, Substrate-dependent deposition behavior of graphite particles dry-sprayed at room temperature using a nano-particle deposition system, *Surface and Coatings Technology*, 309 (2017) 172-178.

- [92] M.N.E.A.A. Nasim, D.-M. Chun, Formation of few-layer graphene flake structures from graphite particles during thin film coating using dry spray deposition method, *Thin Solid Films*, 622 (2017) 34-40.
- [93] F.C. Adams, X-Ray Absorption and Diffraction—Overview, in: P. Worsfold, C. Poole, A. Townshend, M. Miró (Eds.) Reference Module in Chemistry, Molecular Sciences and Chemical Engineering, Academic Press, Oxford, 2017, pp. 391-403.
- [94] C. Liu, F. Li, L.P. Ma, H.M. Cheng, Advanced materials for energy storage, *Adv Mater*, 22 (2010) E28-62.
- [95] M. Kaempgen, C.K. Chan, J. Ma, Y. Cui, G. Gruner, Printable thin film supercapacitors using single-walled carbon nanotubes, *Nano Lett*, 9 (2009) 1872-1876.
- [96] I. Shakir, High Energy Density based Flexible Electrochemical Supercapacitors from Layer-by-Layer Assembled Multiwall Carbon Nanotubes and Graphene, *Electrochimica Acta*, 129 (2014) 396-400.
- [97] M.F. El-Kady, V. Strong, S. Dubin, R.B. Kaner, Laser scribing of high-performance and flexible graphene-based electrochemical capacitors, *Science*, 335 (2012) 1326-1330.
- [98] A.M. Abdelkader, N. Karim, C. Valles, S. Afroj, K.S. Novoselov, S.G. Yeates, Ultraflexible and robust graphene supercapacitors printed on textiles for wearable electronics applications, *2d Materials*, 4 (2017) 35016-35016.
- [99] A.M. Abdelkader, D.J. Fray, Controlled electrochemical doping of graphene-based 3D nanoarchitecture electrodes for supercapacitors and capacitive deionisation, *Nanoscale*, 9 (2017) 14548-14557.

- [100] Q. Wu, Y. Xu, Z. Yao, A. Liu, G. Shi, Supercapacitors based on flexible graphene/polyaniline nanofiber composite films, *ACS Nano*, 4 (2010) 1963-1970.
- [101] Y. Zhu, S. Murali, M. D Stoller, K. Ganesh, W. Cai, P. J Ferreira, A. Pirkle, R. Wallace, K. A Cychosz, M. Thommes, D. Su, E. Stach, R. Ruoff, Carbon-Based Supercapacitors Produced by Activation of Graphene, 2011.
- [102] J. Wei, Z. Zang, Y. Zhang, M. Wang, J. Du, X. Tang, Enhanced performance of light-controlled conductive switching in hybrid cuprous oxide/reduced graphene oxide ($\text{Cu}_2\text{O}/\text{rGO}$) nanocomposites, *Opt Lett*, 42 (2017) 911-914.
- [103] H.J. Huang, J. Zhang, L. Jiang, Z.G. Zang, Preparation of cubic Cu_2O nanoparticles wrapped by reduced graphene oxide for the efficient removal of rhodamine B, *Journal of Alloys and Compounds*, 718 (2017) 112-115.
- [104] Z.G. Zang, X.F. Zeng, M. Wang, W. Hu, C.R. Liu, X.S. Tang, Tunable photoluminescence of water-soluble AgInZnS -graphene oxide (GO) nanocomposites and their application in-vivo bioimaging, *Sensors and Actuators B-Chemical*, 252 (2017) 1179-1186.
- [105] D.A. Dikin, S. Stankovich, E.J. Zimney, R.D. Piner, G.H. Dommett, G. Evmenenko, S.T. Nguyen, R.S. Ruoff, Preparation and characterization of graphene oxide paper, *Nature*, 448 (2007) 457-460.
- [106] M. Segal, Selling graphene by the ton, *Nat Nanotechnol*, 4 (2009) 612-614.
- [107] Z.S. Wu, D.W. Wang, W. Ren, J. Zhao, G. Zhou, F. Li, H.M. Cheng, Anchoring Hydrous RuO_2 on Graphene Sheets for High-Performance Electrochemical Capacitors, *Advanced Functional Materials*, 20 (2010) 3595-3602.

- [108] V. Singh, D. Joung, L. Zhai, S. Das, S.I. Khondaker, S. Seal, Graphene based materials: Past, present and future, *Progress in Materials Science*, 56 (2011) 1178-1271.
- [109] S. Park, R.S. Ruoff, Chemical methods for the production of graphenes, *Nat Nanotechnol*, 4 (2009) 217-224.
- [110] A. Ambrosi, M. Pumera, Electrochemically Exfoliated Graphene and Graphene Oxide for Energy Storage and Electrochemistry Applications, *Chemistry*, 22 (2016) 153-159.
- [111] C.H. Chen, S.W. Yang, M.C. Chuang, W.Y. Woon, C.Y. Su, Towards the continuous production of high crystallinity graphene via electrochemical exfoliation with molecular in situ encapsulation, *Nanoscale*, 7 (2015) 15362-15373.
- [112] A.M. Abdelkader, A.J. Cooper, R.A. Dryfe, I.A. Kinloch, How to get between the sheets: a review of recent works on the electrochemical exfoliation of graphene materials from bulk graphite, *Nanoscale*, 7 (2015) 6944-6956.
- [113] B.D. Ossoinon, D. Belanger, Functionalization of graphene sheets by the diazonium chemistry during electrochemical exfoliation of graphite, *Carbon*, 111 (2017) 83-93.
- [114] S. Yang, S. Bruller, Z.S. Wu, Z. Liu, K. Parvez, R. Dong, F. Richard, P. Samori, X. Feng, K. Mullen, Organic Radical-Assisted Electrochemical Exfoliation for the Scalable Production of High-Quality Graphene, *J Am Chem Soc*, 137 (2015) 13927-13932.
- [115] Y. Hernandez, V. Nicolosi, M. Lotya, F.M. Blighe, Z. Sun, S. De, I.T. McGovern, B. Holland, M. Byrne, Y.K. Gun'Ko, J.J. Boland, P. Niraj, G. Duesberg, S. Krishnamurthy, R. Goodhue, J. Hutchison, V. Scardaci, A.C.

Ferrari, J.N. Coleman, High-yield production of graphene by liquid-phase exfoliation of graphite, *Nat Nanotechnol*, 3 (2008) 563-568.

[116] N. Behabtu, J.R. Lomeda, M.J. Green, A.L. Higginbotham, A. Sinitskii, D.V. Kosynkin, D. Tsentelovich, A.N. Parra-Vasquez, J. Schmidt, E. Kesselman, Y. Cohen, Y. Talmon, J.M. Tour, M. Pasquali, Spontaneous high-concentration dispersions and liquid crystals of graphene, *Nat Nanotechnol*, 5 (2010) 406-411.

[117] Y.Q. Sun, Q.O. Wu, G.Q. Shi, Graphene based new energy materials, *Energy & Environmental Science*, 4 (2011) 1113-1132.

[118] A.C. Ferrari, F. Bonaccorso, V. Fal'ko, K.S. Novoselov, S. Roche, P. Boggild, S. Borini, F.H. Koppens, V. Palermo, N. Pugno, J.A. Garrido, R. Sordan, A. Bianco, L. Ballerini, M. Prato, E. Lidorikis, J. Kivioja, C. Marinelli, T. Ryhanen, A. Morpurgo, J.N. Coleman, V. Nicolosi, L. Colombo, A. Fert, M. Garcia-Hernandez, A. Bachtold, G.F. Schneider, F. Guinea, C. Dekker, M. Barbone, Z. Sun, C. Galiotis, A.N. Grigorenko, G. Konstantatos, A. Kis, M. Katsnelson, L. Vandersypen, A. Loiseau, V. Morandi, D. Neumaier, E. Treossi, V. Pellegrini, M. Polini, A. Tredicucci, G.M. Williams, B.H. Hong, J.H. Ahn, J.M. Kim, H. Zirath, B.J. van Wees, H. van der Zant, L. Occhipinti, A. Di Matteo, I.A. Kinloch, T. Seyller, E. Quesnel, X. Feng, K. Teo, N. Rupesinghe, P. Hakonen, S.R. Neil, Q. Tannock, T. Lofwander, J. Kinaret, Science and technology roadmap for graphene, related two-dimensional crystals, and hybrid systems, *Nanoscale*, 7 (2015) 4598-4810.

[119] A. Reina, X. Jia, J. Ho, D. Nezich, H. Son, V. Bulovic, M.S. Dresselhaus, J. Kong, Large area, few-layer graphene films on arbitrary substrates by chemical vapor deposition, *Nano Lett*, 9 (2009) 30-35.

[120] S. Bae, H. Kim, Y. Lee, X. Xu, J.S. Park, Y. Zheng, J. Balakrishnan, T. Lei, H.R. Kim, Y.I. Song, Y.J. Kim, K.S. Kim, B. Ozyilmaz, J.H. Ahn, B.H. Hong, S.

Iijima, Roll-to-roll production of 30-inch graphene films for transparent electrodes, *Nat Nanotechnol*, 5 (2010) 574-578.

[121] W. Cai, A.L. Moore, Y. Zhu, X. Li, S. Chen, L. Shi, R.S. Ruoff, Thermal transport in suspended and supported monolayer graphene grown by chemical vapor deposition, *Nano Lett*, 10 (2010) 1645-1651.

[122] W.W. Cai, R.D. Piner, Y.W. Zhu, X.S. Li, Z.B. Tan, H.C. Floresca, C.L. Yang, L. Lu, M.J. Kim, R.S. Ruoff, Synthesis of Isotopically-Labeled Graphite Films by Cold-Wall Chemical Vapor Deposition and Electronic Properties of Graphene Obtained from Such Films, *Nano Research*, 2 (2009) 851-856.

[123] B. Fallahazad, Y.F. Hao, K. Lee, S. Kim, R.S. Ruoff, E. Tutuc, Quantum Hall effect in Bernal stacked and twisted bilayer graphene grown on Cu by chemical vapor deposition, *Physical Review B*, 85 (2012) 201408.

[124] J.W. Suk, A. Kitt, C.W. Magnuson, Y. Hao, S. Ahmed, J. An, A.K. Swan, B.B. Goldberg, R.S. Ruoff, Transfer of CVD-grown monolayer graphene onto arbitrary substrates, *ACS Nano*, 5 (2011) 6916-6924.

[125] X. Li, C.W. Magnuson, A. Venugopal, R.M. Tromp, J.B. Hannon, E.M. Vogel, L. Colombo, R.S. Ruoff, Large-area graphene single crystals grown by low-pressure chemical vapor deposition of methane on copper, *J Am Chem Soc*, 133 (2011) 2816-2819.

[126] M.J. Allen, V.C. Tung, R.B. Kaner, Honeycomb carbon: a review of graphene, *Chem Rev*, 110 (2010) 132-145.

[127] K. Jung, W. Song, D.M. Chun, Y.H. Kim, J.C. Yeo, M.S. Kim, S.H. Ahn, C.S. Lee, Nickel Line Patterning Using Silicon Supersonic Micronozzle Integrated with a Nanoparticle Deposition System, *Japanese Journal of Applied Physics*, 49 (2010) 05EC09-05EC09.

- [128] D.M. Chun, S.H. Ahn, Deposition mechanism of dry sprayed ceramic particles at room temperature using a nano-particle deposition system, *Acta Materialia*, 59 (2011) 2693-2703.
- [129] Q. Chen, X.M. Li, X.B. Zang, Y.C. Cao, Y.J. He, P.X. Li, K.L. Wang, J.Q. Wei, D.H. Wu, H.W. Zhu, Effect of different gel electrolytes on graphene-based solid-state supercapacitors, *Rsc Advances*, 4 (2014) 36253-36256.
- [130] S.L. Shen, W. Xiaohong, X. Hexin, Caiwei, Micro supercapacitors based on a 3D structure with symmetric graphene or activated carbon electrodes, *Journal of Micromechanics and Microengineering*, 23 (2013) 114013-114013.
- [131] G.S. Kumar, U. Thupakula, P.K. Sarkar, S. Acharya, Easy extraction of water-soluble graphene quantum dots for light emitting diodes, *RSC Advances*, 5 (2015) 27711-27716.
- [132] A.W. Robertson, J.H. Warner, Atomic resolution imaging of graphene by transmission electron microscopy, *Nanoscale*, 5 (2013) 4079-4093.
- [133] F. Tuinstra, J.L. Koenig, Raman Spectrum of Graphite, *The Journal of Chemical Physics*, 53 (1970) 1126-1130.
- [134] A.C. Ferrari, Raman spectroscopy of graphene and graphite: Disorder, electron-phonon coupling, doping and nonadiabatic effects, *Solid State Communications*, 143 (2007) 47-57.
- [135] L.G. Cancado, M.A. Pimenta, B.R. Neves, G. Medeiros-Ribeiro, T. Enoki, Y. Kobayashi, K. Takai, K. Fukui, M.S. Dresselhaus, R. Saito, A. Jorio, Anisotropy of the Raman spectra of nanographite ribbons, *Phys Rev Lett*, 93 (2004) 047403.
- [136] R.J. Nemanich, S.A. Solin, First- and second-order Raman scattering from finite-size crystals of graphite, *Physical Review B*, 20 (1979) 392-401.

- [137] R.P. Vidano, D.B. Fischbach, L.J. Willis, T.M. Loehr, Observation of Raman band shifting with excitation wavelength for carbons and graphites, *Solid State Communications*, 39 (1981) 341-344.
- [138] I. Pocsik, M. Hundhausen, M. Koos, L. Ley, Origin of the D peak in the Raman spectrum of microcrystalline graphite, *Journal of Non-Crystalline Solids*, 227 (1998) 1083-1086.
- [139] J. Maultzsch, S. Reich, C. Thomsen, H. Requardt, P. Ordejon, Phonon dispersion in graphite, *Phys Rev Lett*, 92 (2004) 075501.
- [140] H. Wang, Y.F. Wang, X.W. Cao, M. Feng, G.X. Lan, Vibrational properties of graphene and graphene layers, *Journal of Raman Spectroscopy*, 40 (2009) 1791-1796.
- [141] M. Hiramatsu, K. Shiji, H. Amano, M. Hori, Fabrication of vertically aligned carbon nanowalls using capacitively coupled plasma-enhanced chemical vapor deposition assisted by hydrogen radical injection, *Applied Physics Letters*, 84 (2004) 4708-4710.
- [142] T. Mori, M. Hiramatsu, K. Yamakawa, K. Takeda, M. Hori, Fabrication of carbon nanowalls using electron beam excited plasma-enhanced chemical vapor deposition, *Diamond and Related Materials*, 17 (2008) 1513-1517.
- [143] Z.H. Ni, Y.Y. Wang, T. Yu, Z.X. Shen, Raman Spectroscopy and Imaging of Graphene, *Nano Research*, 1 (2008) 273-291.
- [144] M.-X. Wang, Q. Liu, H.-F. Sun, E. Stach, H. Zhang, L. Stanciu, J. Xie, Preparation of high-surface-area carbon nanoparticle/graphene composites, 2012.
- [145] J. Liu, M. Notarianni, G. Will, V.T. Tiong, H. Wang, N. Motta, Electrochemically exfoliated graphene for electrode films: effect of graphene

flake thickness on the sheet resistance and capacitive properties, *Langmuir*, 29 (2013) 13307-13314.

[146] B. Galindo, S.G. Alcolea, J. Gómez, A. Navas, A.O. Murguialday, M.P. Fernandez, R.C. Puelles, Effect of the number of layers of graphene on the electrical properties of TPU polymers, *IOP Conference Series: Materials Science and Engineering*, 64 (2014) 012008.

[147] J.P. Zheng, T.R. Jow, The Effect of Salt Concentration in Electrolytes on the Maximum Energy Storage for Double Layer Capacitors, *Journal of The Electrochemical Society*, 144 (1997) 2417-2420.

[148] V. Srinivasan, J.W. Weidner, Studies on the capacitance of nickel oxide films: Effect of heating temperature and electrolyte concentration, *Journal of the Electrochemical Society*, 147 (2000) 880-885.

[149] K. Torchała, K. Kierzek, J. Machnikowski, Capacitance behavior of KOH activated mesocarbon microbeads in different aqueous electrolytes, *Electrochimica Acta*, 86 (2012) 260-267.

[150] X. Yu, H.J. Kim, J.Y. Hong, Y.M. Jung, K.D. Kwon, J. Kong, H.S. Park, Elucidating surface redox charge storage of phosphorus-incorporated graphenes with hierarchical architectures, *Nano Energy*, 15 (2015) 576-586.

[151] Y. Wen, B. Wang, C. Huang, L. Wang, D. Hulicova-Jurcakova, Synthesis of phosphorus-doped graphene and its wide potential window in aqueous supercapacitors, *Chemistry*, 21 (2015) 80-85.

[152] V. Thirumal, A. Pandurangan, R. Jayavel, K.S. Venkatesh, N.S. Palani, R. Ragavan, R. Ilangovan, Single pot electrochemical synthesis of functionalized and phosphorus doped graphene nanosheets for supercapacitor applications, *Journal of Materials Science-Materials in Electronics*, 26 (2015) 6319-6328.

- [153] H. Pan, C.K. Poh, Y.P. Feng, J.Y. Lin, Supercapacitor electrodes from tubes-in-tube carbon nanostructures, *Chemistry of Materials*, 19 (2007) 6120-6125.
- [154] B.Q. Xie, Y. Chen, M.Y. Yu, S.S. Zhang, L.H. Lu, Z. Shu, Y. Zhang, Phosphoric acid-assisted synthesis of layered MoS₂/graphene hybrids with electrolyte-dependent supercapacitive behaviors, *Rsc Advances*, 6 (2016) 89397-89406.
- [155] X. Li, T. Zhao, Q. Chen, P. Li, K. Wang, M. Zhong, J. Wei, D. Wu, B. Wei, H. Zhu, Flexible all solid-state supercapacitors based on chemical vapor deposition derived graphene fibers, *Phys Chem Chem Phys*, 15 (2013) 17752-17757.
- [156] J.J. Yoo, K. Balakrishnan, J. Huang, V. Meunier, B.G. Sumpter, A. Srivastava, M. Conway, A.L. Reddy, J. Yu, R. Vajtai, P.M. Ajayan, Ultrathin planar graphene supercapacitors, *Nano Lett*, 11 (2011) 1423-1427.
- [157] K. Sheng, Y. Sun, C. Li, W. Yuan, G. Shi, Ultrahigh-rate supercapacitors based on electrochemically reduced graphene oxide for ac line-filtering, *Sci Rep*, 2 (2012) 247.
- [158] J.R. Miller, R.A. Outlaw, B.C. Holloway, Graphene double-layer capacitor with ac line-filtering performance, *Science*, 329 (2010) 1637-1639.
- [159] J. Lin, C. Zhang, Z. Yan, Y. Zhu, Z. Peng, R.H. Hauge, D. Natelson, J.M. Tour, 3-Dimensional graphene carbon nanotube carpet-based microsupercapacitors with high electrochemical performance, *Nano Lett*, 13 (2013) 72-78.

- [160] Z.S. Wu, Z. Liu, K. Parvez, X. Feng, K. Mullen, Ultrathin Printable Graphene Supercapacitors with AC Line-Filtering Performance, *Adv Mater*, 27 (2015) 3669-3675.
- [161] A.S.A. Khair, A.K. Arof, Conductivity studies of starch-based polymer electrolytes, *Ionics*, 16 (2010) 123-129.
- [162] F. Beguin, V. Presser, A. Balducci, E. Frackowiak, Carbons and electrolytes for advanced supercapacitors, *Adv Mater*, 26 (2014) 2219-2251, 2283.
- [163] Y.R. Liang, F.X. Liang, H. Zhong, Z.H. Li, R.W. Fu, D.C. Wu, An advanced carbonaceous porous network for high-performance organic electrolyte supercapacitors, *Journal of Materials Chemistry A*, 1 (2013) 7000-7005.
- [164] M. Inagaki, H. Konno, O. Tanaike, Carbon materials for electrochemical capacitors, *Journal of Power Sources*, 195 (2010) 7880-7903.
- [165] Z.H. Li, D.C. Wu, X. Huang, J.H. Ma, H. Liu, Y.R. Liang, R.W. Fu, K. Matyjaszewski, Fabrication of novel polymeric and carbonaceous nanoscale networks by the union of self-assembly and hypercrosslinking, *Energy & Environmental Science*, 7 (2014) 3006-3012.
- [166] K. Fic, M. Meller, E. Frackowiak, Strategies for enhancing the performance of carbon/carbon supercapacitors in aqueous electrolytes, *Electrochimica Acta*, 128 (2014) 210-217.
- [167] Y.F. Zhao, W. Wang, D.B. Xiong, G.J. Shao, W. Xia, S.X. Yu, F.M. Gao, Titanium carbide derived nanoporous carbon for supercapacitor applications, *International Journal of Hydrogen Energy*, 37 (2012) 19395-19400.
- [168] C.W. Liew, S. Ramesh, A.K. Arof, Good prospect of ionic liquid based-poly(vinyl alcohol) polymer electrolytes for supercapacitors with excellent

electrical, electrochemical and thermal properties, *International Journal of Hydrogen Energy*, 39 (2014) 2953-2963.

[169] C.W. Liew, S. Ramesh, A.K. Arof, Characterization of ionic liquid added poly(vinyl alcohol)-based proton conducting polymer electrolytes and electrochemical studies on the supercapacitors, *International Journal of Hydrogen Energy*, 40 (2015) 852-862.

[170] G.A. Snook, P. Kao, A.S. Best, Conducting-polymer-based supercapacitor devices and electrodes, *Journal of Power Sources*, 196 (2011) 1-12.

[171] H. Wang, H. Feng, J. Li, Graphene and graphene-like layered transition metal dichalcogenides in energy conversion and storage, *Small*, 10 (2014) 2165-2181.

[172] L.Q. Fan, G.J. Liu, J.H. Wu, L. Liu, J.M. Lin, Y.L. Wei, Asymmetric supercapacitor based on graphene oxide/polypyrrole composite and activated carbon electrodes, *Electrochimica Acta*, 137 (2014) 26-33.

[173] K.J. Huang, L. Wang, Y.J. Liu, Y.M. Liu, H.B. Wang, T. Gan, L.L. Wang, Layered MoS₂-graphene composites for supercapacitor applications with enhanced capacitive performance, *International Journal of Hydrogen Energy*, 38 (2013) 14027-14034.

[174] A.V. Powell, L. Kosidowski, A. McDowall, Inorganic-organic hybrids by exfoliation of MoS₂, *Journal of Materials Chemistry*, 11 (2001) 1086-1091.

[175] H.S. Matte, A. Gomathi, A.K. Manna, D.J. Late, R. Datta, S.K. Pati, C.N. Rao, MoS₂ and WS₂ analogues of graphene, *Angew Chem Int Ed Engl*, 49 (2010) 4059-4062.

- [176] J. Xiao, D.W. Choi, L. Cosimbescu, P. Koech, J. Liu, J.P. Lemmon, Exfoliated MoS₂ Nanocomposite as an Anode Material for Lithium Ion Batteries, *Chemistry of Materials*, 22 (2010) 4522-4524.
- [177] N. Zheng, X. Bu, P. Feng, Synthetic design of crystalline inorganic chalcogenides exhibiting fast-ion conductivity, *Nature*, 426 (2003) 428-432.
- [178] E.G. da Silveira Firmiano, A.C. Rabelo, C.J. Dalmaschio, A.N. Pinheiro, E.C. Pereira, W.H. Schreiner, E.R. Leite, Supercapacitor Electrodes Obtained by Directly Bonding 2D MoS₂ on Reduced Graphene Oxide, *Advanced Energy Materials*, 4 (2014) 1301380.
- [179] A. Ramadoss, T. Kim, G.S. Kim, S.J. Kim, Enhanced activity of a hydrothermally synthesized mesoporous MoS₂ nanostructure for high performance supercapacitor applications, *New Journal of Chemistry*, 38 (2014) 2379-2385.
- [180] B.L. Hu, X.Y. Qin, A.M. Asiri, K.A. Alamry, A.O. Al-Youbi, X.P. Sun, Synthesis of porous tubular C/MoS₂ nanocomposites and their application as a novel electrode material for supercapacitors with excellent cycling stability, *Electrochimica Acta*, 100 (2013) 24-28.
- [181] K.J. Huang, L. Wang, J.Z. Zhang, L.L. Wang, Y.P. Mo, One-step preparation of layered molybdenum disulfide/multi-walled carbon nanotube composites for enhanced performance supercapacitor, *Energy*, 67 (2014) 234-240.
- [182] J. Wang, Z.C. Wu, K.H. Hu, X.Y. Chen, H.B. Yin, High conductivity graphene-like MoS₂/polyaniline nanocomposites and its application in supercapacitor, *Journal of Alloys and Compounds*, 619 (2015) 38-43.

- [183] W. Song, K. Jung, D.-M. Chun, S.-H. Ahn, C.S. Lee, DEPOSITION OF Al₂O₃ POWDERS USING NANO-PARTICLE DEPOSITION SYSTEM, *Surface Review and Letters*, 17 (2010) 189-193.
- [184] K.J. Lee, S. Woojin, C. Doo-Man, K. Yang-Hee, Y. Jun-Cheol, K. Min-Saeng, A. Sung-Hoon, S. Caroline, Nickel Line Patterning Using Silicon Supersonic Micronozzle Integrated with a Nanoparticle Deposition System, *Japanese Journal of Applied Physics*, 49 (2010) 05EC09-05EC09.
- [185] M.M.M. Mohammed, D.M. Chun, Electrochemical Performance of Few-Layer Graphene Nano-Flake Supercapacitors Prepared by the Vacuum Kinetic Spray Method, *Coatings*, 8 (2018) 302.
- [186] Y. Liu, Z.H. Dang, Y.Y. Wang, J. Huang, H. Li, Hydroxyapatite/graphene-nanosheet composite coatings deposited by vacuum cold spraying for biomedical applications: Inherited nanostructures and enhanced properties, *Carbon*, 67 (2014) 250-259.
- [187] Y. Liu, X.M. Xu, X.K. Suo, Y.F. Gong, H. Li, Suspension Flame Spray Construction of Polyimide-Copper Layers for Marine Antifouling Applications, *Journal of Thermal Spray Technology*, 27 (2018) 98-105.
- [188] V.H. Pham, K.H. Kim, D.W. Jung, K. Singh, E.S. Oh, J.S. Chung, Liquid phase co-exfoliated MoS₂-graphene composites as anode materials for lithium ion batteries, *Journal of Power Sources*, 244 (2013) 280-286.
- [189] M.A. Ibrahim, T.W. Lan, J.K. Huang, Y.Y. Chen, K.H. Wei, L.J. Li, C.W. Chu, High quantity and quality few-layers transition metal disulfide nanosheets from wet-milling exfoliation, *Rsc Advances*, 3 (2013) 13193-13202.

- [190] M. Hiramatsu, M. Hori, Fabrication of carbon nanowalls using novel plasma processing, *Japanese Journal of Applied Physics Part 1-Regular Papers Brief Communications & Review Papers*, 45 (2006) 5522-5527.
- [191] J. Zhu, H. Wang, J. Liu, L. Ouyang, M. Zhu, Exfoliation of MoS₂ and h-BN nanosheets by hydrolysis of LiBH₄, *Nanotechnology*, 28 (2017) 115604.
- [192] J.M. Soon, K.P. Loh, Electrochemical double-layer capacitance of MoS₂ nanowall films, *Electrochemical and Solid State Letters*, 10 (2007) A250-A254.
- [193] M. Acerce, D. Voiry, M. Chhowalla, Metallic 1T phase MoS₂ nanosheets as supercapacitor electrode materials.: EBSCOhost, *Nature Nanotechnology*, 10 (2015) 313-313.
- [194] H. Pan, C.K. Poh, Y.P. Feng, J. Lin, Supercapacitor Electrodes from Tubes-in-Tube Carbon Nanostructures, *Chemistry of Materials*, 19 (2007) 6120-6125.
- [195] B. Xie, Y. Chen, M. Yu, S. Zhang, L. Lu, Z. Shu, Y. Zhang, Phosphoric acid-assisted synthesis of layered MoS₂/graphene hybrids with electrolyte-dependent supercapacitive behaviors, *RSC Advances*, 6 (2016) 89397-89406.
- [196] M.A. Bissett, I.A. Kinloch, R.A. Dryfe, Characterization of MoS₂-Graphene Composites for High-Performance Coin Cell Supercapacitors, *ACS Appl Mater Interfaces*, 7 (2015) 17388-17398.
- [197] Y.X. Xiao, L. Huang, Q. Zhang, S.H. Xu, Q. Chen, W.Z. Shi, Gravure printing of hybrid MoS₂@S-rGO interdigitated electrodes for flexible microsupercapacitors, *Applied Physics Letters*, 107 (2015) 13906-13906.
- [198] C.C. Hu, K.H. Chang, M.C. Lin, Y.T. Wu, Design and tailoring of the nanotubular arrayed architecture of hydrous RuO₂ for next generation supercapacitors, *Nano Lett*, 6 (2006) 2690-2695.

- [199] H. Xia, Y.S. Meng, G.L. Yuan, C. Cui, L. Luc, A Symmetric RuO₂/RuO₂ Supercapacitor Operating at 1.6 V by Using a Neutral Aqueous Electrolyte, *Electrochemical and Solid State Letters*, 15 (2012) A60-A63.
- [200] N. Kang, T. Yu, G.H. Lim, T. Koh, B. Lim, Facile synthesis of carbon-supported, ultrasmall ruthenium oxide nanocrystals for supercapacitor electrode materials, *Chemical Physics Letters*, 592 (2014) 192-195.
- [201] K.W. Nam, K.B. Kim, Manganese oxide film electrodes prepared by electrostatic spray deposition for electrochemical capacitors, *Journal of the Electrochemical Society*, 153 (2006) A81-A88.
- [202] J. Yan, E. Khoo, A. Sumboja, P.S. Lee, Facile coating of manganese oxide on tin oxide nanowires with high-performance capacitive behavior, *ACS Nano*, 4 (2010) 4247-4255.
- [203] J. Ge, H.B. Yao, W. Hu, X.F. Yu, Y.X. Yan, L.B. Mao, H.H. Li, S.S. Li, S.H. Yu, Facile dip coating processed graphene/MnO₂ nanostructured sponges as high performance supercapacitor electrodes, *Nano Energy*, 2 (2013) 505-513.
- [204] S.K. Meher, P. Justin, G.R. Rao, Microwave-mediated synthesis for improved morphology and pseudocapacitance performance of nickel oxide, *ACS Appl Mater Interfaces*, 3 (2011) 2063-2073.
- [205] X.H. Xia, J.P. Tu, X.L. Wang, C.D. Gu, X.B. Zhao, Hierarchically porous NiO film grown by chemical bath deposition via a colloidal crystal template as an electrochemical pseudocapacitor material, *Journal of Materials Chemistry*, 21 (2011) 671-679.
- [206] C.Z. Yuan, L. Yang, L.R. Hou, J.Y. Li, Y.X. Sun, X.G. Zhang, L.F. Shen, X.J. Lu, S.L. Xiong, X.W. Lou, Flexible Hybrid Paper Made of Monolayer Co₃O₄ Microsphere Arrays on rGO/CNTs and Their Application in

Electrochemical Capacitors, *Advanced Functional Materials*, 22 (2012) 2560-2566.

[207] F. Zhang, C.Z. Yuan, X.J. Lu, L.J. Zhang, Q. Che, X.G. Zhang, Facile growth of mesoporous Co₃O₄ nanowire arrays on Ni foam for high performance electrochemical capacitors, *Journal of Power Sources*, 203 (2012) 250-256.

[208] B. Vidyadharan, R. Abd Aziz, I.I. Misnon, G.M.A. Kumar, J. Ismail, M.M. Yusoff, R. Jose, High energy and power density asymmetric supercapacitors using electrospun cobalt oxide nanowire anode, *Journal of Power Sources*, 270 (2014) 526-535.

[209] L.B. Kong, M. Liu, J.W. Lang, Y.C. Luo, L. Kang, Asymmetric Supercapacitor Based on Loose-Packed Cobalt Hydroxide Nanoflake Materials and Activated Carbon, *Journal of the Electrochemical Society*, 156 (2009) A1000-A1004.

[210] Z. Gao, W. Yang, Y. Yan, J. Wang, J. Ma, X. Zhang, B. Xing, L. Liu, Synthesis and Exfoliation of Layered α -Co(OH)₂ Nanosheets and Their Electrochemical Performance for Supercapacitors, *European Journal of Inorganic Chemistry*, 2013 (2013) 4832-4838.

[211] J. Tang, D. Liu, Y. Zheng, X. Li, X. Wang, D. He, Effect of Zn-substitution on cycling performance of α -Co(OH)₂ nanosheet electrode for supercapacitors, *Journal of Materials Chemistry A*, 2 (2014) 2585-2591.

[212] G. Hu, C. Li, H. Gong, Capacitance decay of nanoporous nickel hydroxide, *Journal of Power Sources*, 195 (2010) 6977-6981.

[213] A.K. Mondal, D. Su, S. Chen, J. Zhang, A. Ung, G. Wang, Microwave-assisted synthesis of spherical β -Ni(OH)₂ superstructures for electrochemical

capacitors with excellent cycling stability, *Chemical Physics Letters*, 610-611 (2014) 115-120.

[214] W.P. Sun, X.H. Rui, M. Ulaganathan, S. Madhavi, Q.Y. Yan, Few-layered Ni(OH)₂ nanosheets for high-performance supercapacitors, *Journal of Power Sources*, 295 (2015) 323-328.

[215] U.M. Patil, K.V. Gurav, V.J. Fulari, C.D. Lokhande, O.S. Joo, Characterization of honeycomb-like “β-Ni(OH)₂” thin films synthesized by chemical bath deposition method and their supercapacitor application, *Journal of Power Sources*, 188 (2009) 338-342.

[216] M.S. Wu, K.C. Huang, Fabrication of nickel hydroxide electrodes with open-ended hexagonal nanotube arrays for high capacitance supercapacitors, *Chem Commun (Camb)*, 47 (2011) 12122-12124.

[217] M.M.M. Mohammed, D.-M. Chun, All-Solid-State Supercapacitor Based on MoS₂–Graphite Composite Prepared by the Vacuum Kinetic Spray Method, *Journal of Thermal Spray Technology*, 28 (2019) 963-973.

[218] M.C. Bernard, R. Cortes, M. Keddou, H. Takenouti, P. Bernard, S. Senyari, Structural defects and electrochemical reactivity of β-Ni(OH)₂, *Journal of Power Sources*, 63 (1996) 247-254.

[219] B.C. Cornilsen, P.J. Karjala, P.L. Loyselle, Structural models for nickel electrode active mass, *Journal of Power Sources*, 22 (1988) 351-357.

[220] A. Audemer, A. Delahaye, R. Farhi, N. Sac-Epée, J.M. Tarascon, Electrochemical and Raman Studies of Beta-Type Nickel Hydroxides Ni_{1-x}Co_x(OH)₂ Electrode Materials, *Journal of The Electrochemical Society*, 144 (1997) 2614-2620.

- [221] C. Murli, S.M. Sharma, S.K. Kulshreshtha, S.K. Sikka, High-pressure behavior of β -Ni (OH)₂—A Raman scattering study, *Physica B: Condensed Matter*, 307 (2001) 111-116.
- [222] J.L. Bantignies, S. Deabate, A. Righi, S. Rols, P. Hermet, J.L. Sauvajol, F. Henn, New Insight into the Vibrational Behavior of Nickel Hydroxide and Oxyhydroxide Using Inelastic Neutron Scattering, Far/Mid-Infrared and Raman Spectroscopies, *The Journal of Physical Chemistry C*, 112 (2008) 2193-2201.
- [223] L. Gourrier, S. Deabate, T. Michel, M. Paillet, P. Hermet, J.-L. Bantignies, F. Henn, Characterization of Unusually Large “Pseudo-Single Crystal” of β -Nickel Hydroxide, *The Journal of Physical Chemistry C*, 115 (2011) 15067-15074.
- [224] C. Marini, B. Joseph, S. Caramazza, F. Capitani, M. Bendele, I. Kantor, P. Lotti, O. Mathon, S. Pascarelli, P. Postorino, Local structure investigation of β -Ni(OH)₂ under pressure using combined Raman and Ni K-edge extended x-ray absorption fine structure studies, *High Pressure Research*, 37 (2017) 1-10.
- [225] A. Audemer, Electrochemical and Raman Studies of Beta-Type Nickel Hydroxides Ni_[sub 1-x]Co_[sub x](OH)_[sub 2] Electrode Materials, *Journal of The Electrochemical Society*, 144 (1997) 2614-2620.
- [226] R.T. Wang, J.W. Lang, Y.H. Liu, Z.Y. Lin, X.B. Yan, Ultra-small, size-controlled Ni(OH)₂ nanoparticles: elucidating the relationship between particle size and electrochemical performance for advanced energy storage devices, *Npg Asia Materials*, 7 (2015) e183-e183.
- [227] W. Li, S. Zhang, J. Chen, Synthesis, characterization, and electrochemical application of Ca(OH)₂-, Co(OH)₂-, and Y(OH)₃-Coated Ni(OH)₂ tubes, *J Phys Chem B*, 109 (2005) 14025-14032.

- [228] S.R. Ede, S. Anantharaj, K.T. Kumaran, S. Mishra, S. Kundu, One step synthesis of Ni/Ni(OH)₂ nano sheets (NSs) and their application in asymmetric supercapacitors, *Rsc Advances*, 7 (2017) 5898-5911.
- [229] A.M. Elshahawy, K.H. Ho, Y. Hu, Z. Fan, Y.W.B. Hsu, C. Guan, Q. Ke, J. Wang, Microwave – assisted hydrothermal synthesis of nanocrystal β -Ni(OH)₂ for supercapacitor applications, *CrystEngComm*, 18 (2016) 3256-3264.
- [230] N. Zhang, J.M. Ma, Q. Li, J. Li, D.H.L. Ng, Shape-controlled synthesis of MnCO₃ nanostructures and their applications in supercapacitors, *Rsc Advances*, 5 (2015) 81981-81985.
- [231] X.L. Guo, X.Y. Liu, X.D. Hao, S.J. Zhu, F. Dong, Z.Q. Wen, Y.X. Zhang, Nickel-Manganese Layered Double Hydroxide Nanosheets Supported on Nickel Foam for High-performance Supercapacitor Electrode Materials, *Electrochimica Acta*, 194 (2016) 179-186.
- [232] V. Lakshmi, R. Ranjusha, S. Vineeth, S.V. Nair, A. Balakrishnan, Supercapacitors based on microporous β -Ni(OH)₂ nanorods, *Colloids and Surfaces A: Physicochemical and Engineering Aspects*, 457 (2014) 462-468.
- [233] S. Xing, Q. Wang, Z. Ma, Y. Wu, Y. Gao, Synthesis of mesoporous α -Ni(OH)₂ for high-performance supercapacitors, *Materials Letters*, 78 (2012) 99-101.
- [234] X.H. Xiong, D. Ding, D.C. Chen, G. Waller, Y.F. Bu, Z.X. Wang, M.L. Liu, Three-dimensional ultrathin Ni(OH)₂ nanosheets grown on nickel foam for high-performance supercapacitors, *Nano Energy*, 11 (2015) 154-161.
- [235] R.H. Wang, A. Jayakumar, C.H. Xu, J.M. Lee, Ni(OH)₂ Nanoflowers/Graphene Hydrogels: A New Assembly for Supercapacitors, *Acs Sustainable Chemistry & Engineering*, 4 (2016) 3736-3742.

[236] N. Parveen, M.H. Cho, Self-Assembled 3D Flower-Like Nickel Hydroxide Nanostructures and Their Supercapacitor Applications, *Scientific Reports*, 6 (2016) 27318.

[237] B.R. Wiston, M. Ashok, Electrochemical performance of nickel hydroxide nanopetals for supercapacitor electrodes, *Materials Letters*, 235 (2019) 76-79.

[238] Y. Wang, B. Shang, F. Lin, Y. Chen, R. Ma, B. Peng, Z. Deng, Controllable synthesis of hierarchical nickel hydroxide nanotubes for high performance supercapacitors, *Chemical Communications*, 54 (2018) 559-562.

[239] H. Gao, F. Xiao, C.B. Ching, H. Duan, High-performance asymmetric supercapacitor based on graphene hydrogel and nanostructured MnO₂, *ACS Appl Mater Interfaces*, 4 (2012) 2801-2810.

[240] J. Yan, Z.J. Fan, W. Sun, G.Q. Ning, T. Wei, Q. Zhang, R.F. Zhang, L.J. Zhi, F. Wei, Advanced Asymmetric Supercapacitors Based on Ni(OH)₂/Graphene and Porous Graphene Electrodes with High Energy Density, *Advanced Functional Materials*, 22 (2012) 2632-2641.

[241] H. Yi, H.W. Wang, Y.T. Jing, T.Q. Peng, Y.R. Wang, J. Guo, Q.L. He, Z.H. Guo, X.F. Wang, Advanced asymmetric supercapacitors based on CNT@Ni(OH)₂ core-shell composites and 3D graphene networks, *Journal of Materials Chemistry A*, 3 (2015) 19545-19555.

[242] Q. Liao, S. Jin, C. Wang, Novel graphene-based composite as binder-free high-performance electrodes for energy storage systems, *Journal of Materiomics*, 2 (2016) 291-308.

[243] W. Song, K. Jung, D.M. Chun, S.H. Ahn, C.S. Lee, DEPOSITION OF Al₂O₃ POWDERS USING NANO-PARTICLE DEPOSITION SYSTEM, *Surface Review and Letters*, 17 (2010) 189-193.

- [244] M.M. Mohammed, D.-M. Chun, Electrochemical Performance of Few-Layer Graphene Nano-Flake Supercapacitors Prepared by the Vacuum Kinetic Spray Method, *Coatings*, 8 (2018).
- [245] S. Hossain, W.-S. Chu, C.S. Lee, S.-H. Ahn, D.-M. Chun, Photocatalytic performance of few-layer Graphene/WO₃ thin films prepared by a nano-particle deposition system, *Materials Chemistry and Physics*, 226 (2019) 141-150.
- [246] D. Choi, H. Kim, M. Lee, M. Son, S.-h. Ahn, C.S. Lee, Low-voltage modulated inorganic smart windows using solid polymer electrolyte, *Solar Energy Materials and Solar Cells*, 200 (2019) 109966.
- [247] D.C. Marcano, D.V. Kosynkin, J.M. Berlin, A. Sinitskii, Z. Sun, A. Slesarev, L.B. Alemany, W. Lu, J.M. Tour, Improved synthesis of graphene oxide, *ACS Nano*, 4 (2010) 4806-4814.
- [248] D.-L. Fang, Z.-D. Chen, X. Liu, Z.-F. Wu, C.-H. Zheng, Homogeneous growth of nano-sized β -Ni(OH)₂ on reduced graphene oxide for high-performance supercapacitors, *Electrochimica Acta*, 81 (2012) 321-329.
- [249] A. Lamberti, M. Destro, S. Bianco, M. Quaglio, A. Chiodoni, C.F. Pirri, C. Gerbaldi, Facile fabrication of cuprous oxide nanocomposite anode films for flexible Li-ion batteries via thermal oxidation, *Electrochimica Acta*, 86 (2012) 323-329.
- [250] M. Rajamathi, G. N. Subbanna, P. Vishnu Kamath, On the existence of a nickel hydroxide phase which is neither α nor β , *Journal of Materials Chemistry*, 7 (1997) 2293-2296.
- [251] C. Delmas, C. Tessier, Stacking faults in the structure of nickel hydroxide: a rationale of its high electrochemical activity, *Journal of Materials Chemistry*, 7 (1997) 1439-1443.

- [252] H. Jiang, T. Zhao, C. Li, J. Ma, Hierarchical self-assembly of ultrathin nickel hydroxide nanoflakes for high-performance supercapacitors, *Journal of Materials Chemistry*, 21 (2011) 3818-3823.
- [253] B. Xu, S. Yue, Z. Sui, X. Zhang, S. Hou, G. Cao, Y. Yang, What is the choice for supercapacitors: graphene or graphene oxide?, *Energy & Environmental Science*, 4 (2011) 2826-2830.
- [254] E. Frackowiak, Carbon materials for supercapacitor application, *Physical Chemistry Chemical Physics*, 9 (2007) 1774-1785.
- [255] S.D. Min, C.J. Zhao, Z.M. Zhang, G.R. Chen, X.Z. Qian, Z.P. Guo, Synthesis of Ni(OH)₂/RGO pseudocomposite on nickel foam for supercapacitors with superior performance, *Journal of Materials Chemistry A*, 3 (2015) 3641-3650.
- [256] Y. Liu, R. Wang, X. Yan, Synergistic Effect between Ultra-Small Nickel Hydroxide Nanoparticles and Reduced Graphene Oxide sheets for the Application in High-Performance Asymmetric Supercapacitor, *Sci Rep*, 5 (2015) 11095.
- [257] L.Q. Wang, X.C. Li, T.M. Guo, X.B. Yan, B.K. Tay, Three-dimensional Ni(OH)₂ nanoflakes/graphene/nickel foam electrode with high rate capability for supercapacitor applications, *International Journal of Hydrogen Energy*, 39 (2014) 7876-7884.
- [258] C. Jiang, B. Zhao, J. Cheng, J. Li, H. Zhang, Z. Tang, J. Yang, Hydrothermal synthesis of Ni(OH)₂ nanoflakes on 3D graphene foam for high-performance supercapacitors, *Electrochimica Acta*, 173 (2015) 399-407.
- [259] Z. Wu, X.-L. Huang, Z.-L. Wang, J.-J. Xu, H.-G. Wang, X.-B. Zhang, Electrostatic Induced Stretch Growth of Homogeneous β -Ni(OH)₂ on Graphene

with Enhanced High-Rate Cycling for Supercapacitors, *Scientific Reports*, 4 (2014) 3669.

[260] W.S. Hummers, R.E. Offeman, Preparation of Graphitic Oxide, *Journal of the American Chemical Society*, 80 (1958) 1339-1339.

[261] B. Rajagopalan, J.S. Chung, Reduced chemically modified graphene oxide for supercapacitor electrode, *Nanoscale Research Letters*, 9 (2014) 535.

[262] J. Huang, P. Xu, D. Cao, X. Zhou, S. Yang, Y. Li, G. Wang, Asymmetric supercapacitors based on β -Ni(OH)₂ nanosheets and activated carbon with high energy density, *Journal of Power Sources*, 246 (2014) 371-376.

[263] H.B. Li, M.H. Yu, F.X. Wang, P. Liu, Y. Liang, J. Xiao, C.X. Wang, Y.X. Tong, G.W. Yang, Amorphous nickel hydroxide nanospheres with ultrahigh capacitance and energy density as electrochemical pseudocapacitor materials, *Nature Communications*, 4 (2013) 1894.

[264] Z. Tang, C.-h. Tang, H. Gong, A High Energy Density Asymmetric Supercapacitor from Nano-architected Ni(OH)₂/Carbon Nanotube Electrodes, *Advanced Functional Materials*, 22 (2012) 1272-1278.

[265] S. Zhou, S. Cui, W. Wei, W. Chen, L. Mi, Development of high-utilization honeycomb-like α -Ni(OH)₂ for asymmetric supercapacitors with excellent capacitance, *RSC Advances*, 8 (2018) 37129-37135.

[266] N. Yu, K. Guo, W. Zhang, X. Wang, M.-Q. Zhu, Flexible high-energy asymmetric supercapacitors based on MnO@C composite nanosheet electrodes, *Journal of Materials Chemistry A*, 5 (2017) 804-813.

Appendices

Appendix A: Credits & Copyright Permissions

Notes on Copyright Licenses for Reproduction of Text and Figures in this Thesis

Chapter 1:

For reproducing those figures that have appeared in the following publication with credit to other sources, permission has also been sought from the respective sources.

Chapter 3:

The text excerpts and the figures presented in Chapter Three are reproduced with permission from the following article.

Mohaned Mohammed Mahmoud Mohammed and Doo-Man Chun, “*Electrochemical Performance of Few-Layer Graphene Nano-Flake Supercapacitors Prepared by the Vacuum Kinetic Spray Method*”, *Coatings* 2018, 8 (9), 302. (Open access).

Chapter 4:

The text excerpts and the figures presented in Chapter 4 are reproduced with permission from the following article.

Mohaned Mohammed Mahmoud Mohammed and Doo-Man Chun, “*All-Solid-State Supercapacitor Based on MoS₂–Graphite Composite Prepared by the Vacuum Kinetic Spray Method*”, *Journal of Thermal Spray Technology*, 2019, 28 (5), 963–973. Copyright © 2019, ASM International.

Chapter 5:

The text excerpts and the figures presented in Chapter 5 are reproduced with permission from the following article.

Mohaned Mohammed Mahmoud Mohammed and Doo-Man Chun, “*Deposition of Ni(OH)₂ on nickel substrate using vacuum kinetic spray and its application to high-performance supercapacitor*”, *Journal of Materials Science: Materials in Electronics*, 2019, 30 (18), 17481–17490. Copyright © 2019, Springer Science Business Media, LLC, part of Springer Nature.

List of Publications

- [1] Mohaned Mohammed Mahmoud Mohammed and Doo-Man Chun*, “Electrochemical Performance of Few-Layer Graphene Nano-Flake Supercapacitors Prepared by the Vacuum Kinetic Spray Method”, *Coatings*, **2018**, 8 (9), 302.
- [2] Mohaned Mohammed Mahmoud Mohammed and Doo-Man Chun*, “All-Solid-State Supercapacitor Based on MoS₂–Graphite Composite Prepared by the Vacuum Kinetic Spray Method”, *Journal of Thermal Spray Technology*, **2019**, 28 (5), 963–973.
- [3] Mohaned Mohammed Mahmoud Mohammed and Doo-Man Chun*, “Deposition of Ni(OH)₂ on nickel substrate using vacuum kinetic spray and its application to high-performance supercapacitor”, *Journal of Materials Science: Materials in Electronics*, **2019**, 30 (18), 17481–17490.
- [4] Mohaned M. M. Mohammed, A. G. Abd-Elrahim, and Doo-Man Chun* “One-step deposition of a Ni(OH)₂-graphene hybrid prepared by vacuum kinetic spray for high energy density hybrid supercapacitor”. *[submitted]*
- [5] A. G. Abd-Elrahim, Mohaned M. M. Mohammed, and Doo-Man Chun* “Composition dependent electrocatalytic activity of Ni(OH)₂-graphene hybrid catalyst deposited by one-step vacuum kinetic spray technique”. *[submitted]*